Molecular-Level Modeling of Thermal Transport Mechanisms within Carbon Nanotube/Graphene-based Nanostructure-enhanced Phase Change Materials

by

Hasan Babaei

A dissertation submitted to the Graduate Faculty of
Auburn University
in partial fulfillment of the
requirements for the Degree of
Doctor of Philosophy

Auburn, Alabama
August 2, 2014

Keywords: Nanostructure-enhanced Phase Change Materials, Nanofluid, Carbon Nanotube, Graphene, Thermal Transport, Molecular Dynamics Simulation, Thermal Conductance

Approved by

Jay M. Khodadadi, Chair, Alumni Professor, Mechanical Engineering Department
Pawel Keblinski, Co-chair, Professor of Materials Science and Engineering, Rensselaer Polytechnic Institute
W. Robert Ashurst, Associate Professor, Chemical Engineering Department
Rik Blumenthal, Associate Professor, Chemistry and Biochemistry Department

Abstract

The mechanisms of nanoscale thermal transport within nanoparticle suspensions (nanofluids) and nanostructure-enhanced phase change materials (NePCM) are investigated using molecular dynamics (MD) simulations.

To begin, the terms included in the heat current expression utilized in the Green-Kubo-based equilibrium MD (EMD) simulations are examined by performing simulations on different multi-component systems including model nanofluid and gas, liquid and solid mixtures. The results are compared against those obtained with the application of the heat source and sink and determination of the thermal conductivity using non-equilibrium molecular dynamics (NEMD) and the Fourier's Law. The results indicate that the proper definition of the heat current in the equilibrium simulations leads to the consistency between the results obtained using the EMD and NEMD simulations. The validated EMD method is utilized to study the role of the Brownian motion-induced micro-convection in the thermal conductivity of well-dispersed nanofluids. An illustrative decomposition of the thermal conductivity into appropriate components shows that while the individual terms in the heat current autocorrelation function associated with the diffusion of nanoparticles achieve significant values, these terms essentially cancel each other if the correctly-defined average enthalpy expressions are subtracted. Otherwise, erroneous thermal conductivity enhancements will be predicted that are attributed to the Brownian motion-induced micro-convection. Consequently, micro-convection does not contribute noticeably to the thermal

conductivity and the predicted thermal conductivity enhancements are consistent with the effective medium theory.

Then, the experimentally-observed improving effect of high aspect-ratio carbon-based nano-fillers, e.g. carbon nanotubes (CNT) and graphene sheets, on heat transfer within paraffin-based phase change materials is investigated. Firstly, the thermal conductivity of liquid and solid n-octadecane (as n-paraffin) is determined by using the direct method-based NEMD simulations. Different calculated thermo-physical properties of liquid/solid n-octadecane show good consistency between the numerical results and experimental data. It is observed that through solidification, nano-crystalline domains form in n-octadecane and in agreement with experimental data the value of the thermal conductivity increases. The calculations for a perfect crystal structure of n-octadecane molecules show that the thermal conductivity along the molecular axis is four times higher than the value for the solid case, showing a strong relation between the ordering of paraffin's molecules and its thermal conductivity. Introducing CNT and graphene sheets in paraffin promotes aligning of paraffin's molecules in the direction parallel to the CNT axis and graphene surface, respectively and consequently lead to considerable enhancements in its thermal conductivity along those directions. Then, descriptive set of simulations are designed to study the overall thermal conductivity enhancement for the solid/liquid mixtures and also determine the contribution of the proposed mechanism in such enhancement. The results exhibit improvements in the thermal conductivity well beyond the predictions of the effective medium theory and indicate the dominant role of the filler-induced alignment mechanism.

The investigation on the interfacial thermal conductance, which is a key element in heat transfer through multi-component systems, between graphene sheets and paraffin also shed light

on the nanoscale thermal transport within such mixtures/composites. The results from the direct method-based NEMD calculations reveal two main statements: (i) for solid phase paraffin the interfacial thermal conductance is higher than the corresponding liquid phase paraffin, more likely due to the more effective filler-induced ordering of paraffin molecules, and (ii) the graphene sheets containing a few number of layers exhibit higher values of the interfacial thermal conductance with respect to the thicker graphene sheets.

Acknowledgments

I would like to thank my wife for her unconditional and consistent support and encouragement and my family, particularly my parents, for their support, patience and advice during all steps of my life.

I am grateful for support and advice from Dr. Jay M. Khodadadi during the whole period of my PhD. He was always advising me on the right track to achieve my academic goals. He was also consistently providing me with different academic opportunities to accumulate helpful experience for my future career. I also thank him for teaching of three well-designed graduate-level fluid mechanics courses.

I am also grateful for advice from Dr. Pawel Keblinski. I have had wonderful time during my PhD studies discussing exciting novel scientific and technical problems with him and getting very helpful feedback along with my consistent learning process.

I would like to thank Dr. Rik Blumenthal for teaching me a great deal and close work on inter/intra-molecular forces and molecular electronic structure during a 1-year coursework at the Department of Chemistry at Auburn University. He kindly defined a project on force field parameterization by using *ab initio* quantum mechanical calculations and scheduled weekly meetings to discuss issues that arose along the way. I had very helpful and exciting discussions during those meetings. I would also like to thank Dr. Jianjun Dong for teaching me statistical mechanics and “theories and simulations of thermal conductivity” and defining a relevant project during my 1-year coursework at the Department of Physics at Auburn University. I would also like to thank Dr. W. Robert Ashurst for his great course on transport phenomena and his comments during the initial stages of the project.

Permission to reuse copyrighted materials in compilation of this dissertation granted by The American Institute of Physics (AIP) and Elsevier is acknowledged. These materials include:

1. Babaei, H., Keblinski, P., Khodadadi, J. M., 2013, “Improvement in thermal conductivity of paraffin by adding high aspect-ratio carbon-based nano-fillers,” *Physics Letters A*, **377**, pp. 1358–1361. (in chapter 4)
2. Babaei, H., Keblinski, P., Khodadadi, J. M., 2013, “A proof for insignificant effect of Brownian motion-induced micro-convection on thermal conductivity of nanofluids by utilizing molecular dynamics simulations,” *Journal of Applied Physics*, **113**, 084302. (in chapter 3)
3. Khodadadi, J. M., Fan, L., Babaei, H., 2013, “Thermal conductivity enhancement of nanostructure-based colloidal suspensions utilized as phase change materials for thermal energy storage: a review, *Renewable & Sustainable Energy Reviews*, **24**, pp. 418-444.
4. Babaei, H., Keblinski, P., Khodadadi, J. M., 2013, “Thermal conductivity enhancement of paraffins by increasing the alignment of molecules through adding CNT/graphene,” *International Journal of Heat and Mass Transfer*, **58**(1-2), pp. 209-216. (in chapter 4)
5. Babaei, H., Keblinski, P., Khodadadi, J. M., 2012, “Equilibrium molecular dynamics determination of thermal conductivity for multi-component systems,” *Journal of Applied Physics*, **112**, 054310. (in chapter 2)

6. Babaei, H., Keblinski, P., Khodadadi, J. M., 2013, “Molecular dynamics study of the interfacial thermal conductance at the graphene/paraffin interface in solid and liquid phases, In ASME 2013 Heat Transfer Summer Conference collocated with the ASME 2013 7th International Conference on Energy Sustainability and the ASME 2013 11th International Conference on Fuel Cell Science, Engineering and Technology, pp. V004T14A018-V004T14A018. American Society of Mechanical Engineers, 2013. (in chapter 5)

This dissertation is based upon work supported by the US Department of Energy under Award Number DE-SC0002470 (http://www.eng.auburn.edu/nepcm). This report was prepared as an account of work sponsored by an agency of the United States Government. Neither the United States Government nor any agency thereof, nor any of their employees, makes any warranty, express or implied, or assumes any legal liability or responsibility for the accuracy, completeness, or usefulness of any information, apparatus, product, or process disclosed, or represents that its use would not infringe privately owned rights. References herein to any specific commercial product, process, or service by trade name, trademark, manufacturer, or otherwise does not necessarily constitute or imply its endorsement, recommendation, or favoring by the United States Government or any agency thereof. The views and opinions of authors expressed herein do not necessarily state or reflect those of the United States Government or any agency thereof.

I also acknowledge financial support provided by the Alabama EPSCoR Program under the Graduate Research Scholars Program (Rounds 6, 7 and 8).

I am also grateful to the Samuel Ginn College of Engineering and the Department of Mechanical Engineering at Auburn University for providing support for my Dean’s Fellowship (Fall 2009-Fall 2012).

I also acknowledge the Alabama Supercomputer Center (www.asc.edu) for providing computational facilities for performing simulations.

Table of Contents

List of Tables

List of Figures

List of Symbols

Nomenclature

a_1; a_2; a_3	ellipsoid’s dimensions, Å
a_k	Kapitza length, Å
a	range-limiting term in the Tersoff potential
A	cross-sectional area, Å^2
A	parameter in the Tersoff potential, eV
b	bond length, Å
b	range-limiting term in the Tersoff potential
B	constant in the Tersoff potential, eV
c	constant in the Tersoff potential (chapter 2)
$\mathrm{c_p}$	heat capacity per particle
C	constant
C	convective term (chapters 2 and 3)
d	constant in the Tersoff potential (chapter 2); particle diameter, Å (chapter 3); layer thickness, nm (chapter 4)
D	self-diffusion coefficient, m^2/s
E	internal energy, kcal/mol
f_{ij}^A	attractive term in the Tersoff potential, eV
f_{ij}^R	repulsive term in the Tersoff potential, eV

$\mathbf{f}$	force acting on the particles, kcal/mol Å
$\mathbf{F}_{ij}$	force acting on particle *i* due to particle *j*, kcal/mol Å
g	parameter in the Tersoff potential
G	interfacial thermal conductance, MW/m^2 K
h	constant in the Tersoff potential
h_α	partial enthalpy for species α, kcal/mol
H	enthalpy term in heat current, W/m^2
H	Hamiltonian (chapter 2)
$\mathbf{J}$	heat current, W/m^2
k	thermal conductivity, W/m K
k_B	Boltzmann constant, kcal/mol K
k_{ii}^c	*i*-th element of the equivalent thermal conductivity tensor, W/m K
K	kinetic energy, kcal/mol
K_r	bond stretching force coefficient, K/ Å^2
K_θ	bond bending force coefficient, K/rad^2
l	particle mean free path, Å
L_{ii}	geometrical factor associated with direction *i*
L	length of simulation cell, Å
m	mass of particles, grams/mol
n	particle number density, mol^{-1}
n	constant in the Tersoff potential
N	number of particles
p	aspect-ratio

$\mathbf{p}$	momentum of particles, (grams/mol)(Å/fs)
P	pressure, atm
q	heat flux, W/m^2
Q	mass conjugate for variable s in NVT and NPT MD simulations, (kcal/mol)(fs)^2
Q	heat, kcal/mol
r	radius, Å
$\mathbf{r}$	position vector of particles, Å
R	interfacial thermal resistance, m^2 K/MW
R	cut-off distance in the Tersoff potential, Å
R_i	distance between layer i and CNT axis, nm
s	alignment parameter
s	variable for NVT and NPT MD simulations
S	cut-off distance in the Tersoff potential, Å
t	time, ns or ps
T	temperature, K
U	potential energy, kcal/mol
U_0; U_1; U_2; U_3	parameters in torsional potential, K
$\mathbf{v}$	velocity of particles, Å/fs
V	virial term, W/m^2 (chapters 2 and 3); volume of simulation box, Å^3; variable for NPT MD simulations, Å^3
W	mass conjugate for variable V in NPT MD simulations, (kcal/mol)(fs)^2 Å$^{-2/3}$
x; y; z	Cartesian coordinates

Abbreviations

AMM	acoustic mismatch model
BTE	Boltzmann transport equation
CNF	carbon nanofiber
CNT	carbon nanotube
COMPASS	condensed-phase optimized molecular potentials for atomistic simulation studies
DMM	diffuse mismatch model
EAM	embedded atom method
EMD	equilibrium molecular dynamics
FCC	face-centered cubic
FENE	finite extensible nonlinear elastic
GNP	graphene nanoplatelet
HCACF	heat current auto-correlation function
HFACF	heat flux auto-correlation function
H-S	Hashin and Shtrikman
LAMMPS	large-scale atomic/molecular massively parallel simulator
LJ	Lennard-Jones
MD	molecular dynamics
MWCNT	multi-walled carbon nanotube
NePCM	nanostructure-enhanced phase change materials
NEMD	non-equilibrium molecular dynamics
NERD	Nath, Escobedo and de Pablo-revised
NPT	constant number of particles, pressure and temperature
NVE	constant number of particles, volume and energy

NVT	constant number of particles, volume and temperature
OPLS	optimized potentials for liquid simulations
PCM	phase change materials
SKS	Smith, Karaborni and Siepmann
SWCNT	single-walled carbon nanotube
TEM	transmission electron microscopy
TraPPE	Transferable potentials for phase equilibria

Greek Symbols

α	geometrical parameter in the Nan’s model
β	constant in the Tersoff potential
β_{ii}	parameters in the Nan’s model
Δt	time step, fs
ΔT	temperature difference, ^{o}C
ε	Lennard-Jones parameter, energy scale, kcal/mol
ϕ	volume fraction
λ_1	constant in the Tersoff potential, Å^{-1}
λ_2	constant in the Tersoff potential, Å^{-1}
γ	geometrical parameter in the Nan’s model
θ	bond angle, chapter 2
θ	angle between the end-to-end vector a molecule and an axis, chapter 4
σ	Lennard-Jones parameter, length scale, Å
ψ	dihedral angle
ζ	parameter in the Tersoff potential

Subscripts

eff	effective
eq	equilibrium
ex	external
i	particle i
i	x, y or z
j	particle j
k	particle k
k	Kapitza, chapter 3
l	liquid
m	matrix
n	nth step
p	particle
r	bond length
s	solid
s	parameter s in NVT or NVT MD simulations, chapter 2
V	parameter V in NVT or NVT MD simulations
x; y; z	Cartesian coordinates
∞	infinity
α	species α
θ	bond angle

Superscripts

A	attractive
C	cut-off

R	repulsive

Chapter 1 Introduction

In this chapter, the background and motivation of the research is explained in the first section, followed by an outline of the objectives and the structure of the dissertation in the second section.

1.1 Background and motivation

In recent decades, availability of energy and its stable supply at a steady price has become one of the most important issues in developed and developing countries. These matters, in turn, are linked to regional and global economic growth through affecting residential, commercial and industrial energy consumptions. Instabilities associated with supply of the fossil fuels compounded with the environmental concerns in terms of release of pollutants, etc., have necessitated greater focus on utilizing other sources of energy, e.g., solar, wind, or wave energy. Upon maturity and cost-effectiveness, these renewable sources of energy will prove reliable and sustainable ways of providing energy. The need for making the conversion of these renewable sources of energy more efficient has attracted the attention of a great number of investigators. Due to the unreliable supply of the renewable sources of energy, storing of energy is the most critical obstacle that can hamper utilization of renewable sources of energy. Among all types of energy, thermal energy is considered to be the lowest grade and is generally associated with “waste heat”. Despite the low quality of the thermal energy, rejected thermal energy and waste heat are widely encountered in transportation, industrial processes, household energy portfolios, etc.

One of the convenient ways to store thermal energy is through using Phase Change Materials (PCM). PCM offer their sizeable latent heat for storing thermal energy at a constant temperature. However, a drawback of such materials is their relatively low thermal conductivity, which strongly suppresses the energy charge/discharge rates. Introduction of highly-conductive materials, e.g., metal fins or graphite fibers, into the PCM in order to enhance the thermal conductivity has long been studied (Fan and Khodadadi, 2011). The resulting mixtures/composites have higher apparent thermal conductivity than the original PCM. A far more challenging option is to suspend highly-conductive particles into PCM, which leads to "free-form" mixtures/composites. During the last decade, utilization of ultrafine nanoparticles in liquids (referred to as nanofluids) as promoters of thermal conductivity has been the topic of interest for many researchers worldwide. However, the idea was highly-debated in relation to the initial promise of introducing very high enhancement (order of magnitude increase) in the thermal conductivity. It was initially suggested by some researchers that for well-dispersed nanofluids, the Brownian motion-induced micro-convection has led to the experimentally-observed enhancements of thermal conductivity. On the other side of the debate, some researchers explained that the claimed micro-convection does not lead to any enhancement and the observed enhancements are due to the aggregation of nanoparticles. The statement by this group of researchers was that for well-dispersed nanofluids, the increase in thermal conductivity follows the model of Maxwell (1881) with no extraordinary enhancements.

In 2007, the idea of utilizing nanoparticles to improve the thermal conductivity of PCM was proposed by Khodadadi and Hosseinizadeh (2007). Recently researchers have widely investigated the influence of different nanoparticles on thermal conductivity of different PCM. Very recently, it has been observed that nano-size high aspect-ratio carbon-based fillers, e.g. carbon nanotubes (CNT), graphene and graphite nano-platelets, introduce even greater improvements in thermal conductivity of paraffin as a common PCM (Yu et al., 2013 and Shi et al., 2013).

The above discussion on the effect of nano-fillers on thermal transport in fluids/PCM directed us to a conclusion that an in-depth investigation on the nanoscale mechanisms involved in thermal transport within such suspensions/composites is required. This research project is devoted to a non-continuum-based investigation of the effects of adding nanofillers to fluids/PCM and the resulting heat transport within the nanoparticle suspensions/composites. The novel type of PCM which is enhanced by nanoparticles is referred to as nanostructure-enhanced PCM (NePCM).

Continuum-level modeling of transport phenomena in materials requires transport properties of bulk materials such as the diffusion coefficient, viscosity, thermal conductivity and electrical conductivity for mass, momentum, heat and charge transfer problems, respectively. The required transport relations corresponding to mass, momentum, heat and charge transfer are the Fick's, Newton's, Fourier's and Ohm's Laws, respectively. The transport properties of materials are basically related to the fundamental transport carriers including atoms, electrons, phonons and photons. In macro-scale problems, these transport properties are used to study the transport phenomena without the need to directly study the fundamental carriers. In contrast, for the multicomponent materials composed of sub-micron-scale-structured components and also the sub-micron-scale materials, those bulk-transport-properties-based sets of equations are not capable of fully explaining the undergoing transport phenomena. This is because the boundary, size and interfacial effects play significant roles in essentially changing the mechanisms of transport. In order to gain further insight into the transport phenomena within such materials at the sub-micron-scale, the corresponding fundamental transport carriers are needed to be directly and fully studied. The nature of transport within the NePCM studied in this dissertation is mostly associated with the atoms and molecules and in some ideal cases of solids it also contains phonons.

Limitations of the continuum modeling in handling the particle-particle and particle-media interactions in a NePCM calls for adoption of more sophisticated non-continuum simulation methods. The Molecular Dynamics (MD) method is an excellent candidate for handling the length and time scales that are expected in this problem. MD method is capable of monitoring the dynamics of atoms and molecules which are the fundamental thermal transport carriers within NePCM. The method is a potentially powerful predictive tool to quantify the underlying physics of heat transfer mechanisms in nanoparticle suspensions/composites.

1.2 Objectives and structure of the dissertation

The objectives of this dissertation are:

- Investigating the mechanisms of heat transfer in spherical nanoparticles suspensions. This study will attempt to answer the question in relation to the effectiveness of the spherical nanoparticles in improving the thermal conductivity of the base fluid.
- Investigating the thermal conductivity improvement and nanoscale thermal transport mechanisms in liquid/solid mixtures of PCM and high aspect-ratio carbon-based nano-fillers. In this regard, special attention is given to the thermal transport in paraffin as PCM and its molecular ordering-thermal conductivity relationship. The effect of introducing those high aspect-ratio carbon-based nano-fillers on the ordering of paraffin’s molecules will be studied and the corresponding increase in the thermal conductivity will be assessed.

This thesis is organized as follows:

In chapter 2, the utilized methodologies are explained. Molecular dynamics (MD) simulation is first described. Then, the main two MD-based methods (Green-Kubo and direct methods) for evaluating the thermal conductivity are explained. With regard to the Green-Kubo method, wide-ranging simulations on different multicomponent systems are performed to validate the terms involved in the heat flux expression.

Chapter 3 is devoted to the discussion on the thermal conductivity of spherical nanoparticle suspensions. The debated effect of the Brownian motion-induced micro-convection on the thermal conductivity of nanofluids is discussed by decomposing the terms involved in the Green-Kubo-based calculations of the thermal conductivity. In order to judge the potential anomalous improvement, the calculated values of the thermal conductivity for well-dispersed nanofluids are compared with the predictions of the Maxwell's model.

Chapter 4 contains the study of the effects of adding carbon-based high aspect-ratio nano-fillers (CNT and graphene) on the thermal conductivity of paraffin. In this chapter, the relation between ordering of paraffin molecules on its thermal conductivity is studied. Moreover, the induced ordering of paraffin's molecules by introducing those nano-fillers and the resulting high enhancements are evaluated. Finally, a discussion will be given on the dominant mechanism in thermal conductivity improvement.

In chapter 5, results of investigation of the interfacial thermal conductance between graphene sheets and paraffin are reported. In this regard, the effect of the paraffin phase and the thickness of graphene on the interfacial thermal conductance are studied.

It should be mentioned that the literature reviews corresponding to the topic of each chapter will be presented at the beginning of the corresponding chapter.

Finally, conclusions of the dissertation along with future research directions are presented in chapter 6.

Chapter 2 Methodology

In this chapter, the methodology that is used in the dissertation is explained. The chapter has two main sections. In the first section, the molecular dynamics (MD) simulation technique is explained. In the second section, the methods for the prediction of the thermal conductivity are discussed. A detailed discussion of the terms involved in the microscopic heat flux used in the Green-Kubo-based equilibrium method is also presented and validated for different cases against the Fourier Law-based non-equilibrium method.

2.1 Molecular Dynamics Simulation

Molecular dynamics simulation is a highly-appreciated method which can be utilized for studying the nanoscale phenomena. In an MD simulation, the motion of atoms/molecules contained in a system is determined by solving the governing Newton's second law for an ensemble of the atoms/molecules. The functions that relate the interacting forces between the atoms/molecules to their locations are called the force fields and extracted by parameterizing functions with particular forms through fitting to the results of quantum mechanical *ab initio* calculations for subatomic particles and comparing the MD-predicted macroscale properties such as density of materials with corresponding experimental data. In these potential functions, atoms/molecules interact with each other as spherical balls. These could be in the form of pairwise, three-body and many-body interactions. For example, a pairwise interaction potential consists of repulsion and attraction parts and has an equilibrium distance between the balls. The force acting on the particles has the following relation with the potential energy

$$\mathbf{f} = -\nabla U \tag{2.1}$$

where **f** is the force and *U* is the potential energy. Knowing the initial velocity and position and the force acting on a particle, one can use the second law of Newton to predict its trajectory. The equation of motion for particle *i* reads

$$m_i \frac{d^2\mathbf{r}_i}{dt^2} = \mathbf{f}_i \tag{2.2}$$

where m_i and $\mathbf{r}_i$ are the mass and position vector of particle *i*, respectively. In an MD simulation, these equations are integrated in time for all particles and the time evolution of their positions and momentums are determined. Different algorithms have been proposed for time integration of the equations of motion. Here, the Verlet algorithm, one of the widely-used ones, and its derivation is explained in detail. The Taylor series expansion of the position of particle *i* at the *n+1*th step around the *n*th step is

$$\begin{aligned} \mathbf{r}_{i,n+1} &= \mathbf{r}_{i,n} + \left.\frac{d\mathbf{r}_i}{dt}\right|_n \Delta t + \frac{1}{2}\left.\frac{d^2\mathbf{r}_{i,n}}{dt^2}\right|_n \Delta t^2 + \frac{1}{6}\left.\frac{d^3\mathbf{r}_i}{dt^3}\right|_n \Delta t^3 + O(\Delta t^4) \\ &= \mathbf{r}_{i,n} + \mathbf{v}_{i,n}\Delta t + \frac{1}{2}\frac{\mathbf{f}_{i,n}}{m_i}\Delta t^2 + \frac{1}{6}\left.\frac{d^3\mathbf{r}_i}{dt^3}\right|_n \Delta t^3 + O(\Delta t^4) \end{aligned} \tag{2.3}$$

where $\mathbf{v}_{i,n}$ and $\mathbf{f}_{i,n}$ are the velocity and the force for particle *i* at step *n*, respectively. The quantity Δt is the time step, whereas $O(\Delta t^4)$ stands for terms of order 4 or higher in Δt

Similarly, the equation for the position at the *(n-1)*th step is

$$\mathbf{r}_{i,n-1} = \mathbf{r}_{i,n} - \mathbf{v}_{i,n}\Delta t + \frac{1}{2}\frac{\mathbf{f}_{i,n}}{m_i}\Delta t^2 - \frac{1}{6}\left.\frac{d^3\mathbf{r}_i}{dt^3}\right|_n \Delta t^3 + O(\Delta t^4) \tag{2.4}$$

Summing equations (2.3) and (2.4), one obtains

$$\mathbf{r}_{i,n+1} \approx 2\mathbf{r}_{i,n} - \mathbf{r}_{i,n-1} + \frac{\mathbf{f}_{i,n}}{m_i}\Delta t^2 \tag{2.5}$$

Equation (2.5) is used to estimate the new position of particle *i* based on the force of the particle obtained at the previous time step and the positions at the two last time steps. This equation does not depend on the velocity. The velocity is obtained for the new step as given in the following equation derived by subtracting equation (2.4) from relation (2.3),

$$\mathbf{v}_{i,n} = \frac{\mathbf{r}_{i,n+1} - \mathbf{r}_{i,n-1}}{2\Delta t} \tag{2.6}$$

The algorithm works by starting from the initial positions and velocities of particles. The initial velocities for particles are calculated based on a desired initial temperature and a random number seed determining the velocity distribution among particles. The velocity distribution should be such that the average kinetic energy of the particles in a classical view and in accordance with the equipartition theorem will be associated with the defined temperature. Throughout this project, the Packmol (Martinez et al., 2009) and XenoView (Shenogin and Ozisik, 2007) software packages have been utilized to create the initial positions of the atoms. The positions of the particles are updated by moving them from the initial positions considering the initial velocities. Then, by using equations (2.5) and (2.6), the positions and velocities are updated for next time steps. The time step is usually of the order of 1 fs and depends on the atomic vibrations in the system which itself depends on the strength of the interacting forces and masses of particles. All simulations were performed with the large-scale atomic/molecular massively parallel simulator (LAMMPS) molecular dynamics package (Plimpton, 1995).

Based on the objectives of a molecular modeling problem, different boundary conditions can be applied on the sides of the simulation box. The widely-adopted one is the periodic boundary condition which is commonly utilized to characterize the bulk properties of materials. Through adopting this boundary condition, the particles receive forces coming from particles included in a similar box located on the side where the periodic condition should be applied. A schematic diagram representing the utilization of periodic boundary condition is shown in Figure 2.1.

The explained MD method, in view of statistical physics, corresponds to the microcanonical (NVE, i.e. constant number of particles, volume and energy) ensemble because throughout MD simulations, the volume and the number of particles in the simulation cell do not vary and the energy of system is conserved by the Newton’s equation of motion. However, experimental measurements are often conducted within constant temperature and/or constant pressure conditions. The widely-adopted experimental approach of studying materials at constant temperature and pressure conditions calls for adaptation of a MD method capable of providing such conditions. In this regard, the MD simulation should provide a phase space which corresponds to the canonical (NVT) or isothermal-isobaric (NPT) statistical ensembles. The attempts of physicists have led to different methods, namely, stochastic methods, constraint methods and extended system methods (Allen and Tildesley, 1987). In stochastic methods (Anderson, 1980), the system interacts with a heat bath in the following way. The momentum of a particle which is randomly chosen is revalued based on the Maxwell-Boltzmann velocity distribution at a given temperature (kinetic energy). These stochastic collisions with the bath take place at time intervals which are assigned via the Poisson distribution around a specified mean value. By using this approach, if an infrequent collision interval is chosen, the temperature of the whole system converges gradually to the desired temperature without showing deviation from the inherent dynamical fluctuations of the system. In the constraint method, the momentums of all particles are rescaled to the values associated with the desired temperature. In an extended system method, which is used in this project, extra degrees of freedom are added to the Hamiltonian (and consequently to the equations of motion) of the system (Nose, 1984). These extra variables represent the reservoirs used for controlling the temperature and/or pressure of the system. The variables added for controlling the temperature and the pressure of the system are *s* and

V, where *V* is the volume of the system. The Hamiltonian, *H*, of the system is now defined as follows

$$H = \sum_i \mathbf{p}_i^2 / 2m_i V^{2/3} s^2 + \Phi(V^{1/3}\mathbf{r}) + p_s^2 / 2Q + gkT \ln s + p_V^2 / 2W + P_{ex} V \tag{2.7}$$

The first two terms on the right hand side of Eq. (2.7) are the kinetic and potential energy of the system of particles, respectively. The variable $\mathbf{p}_i$ is the scaled version of the momentum of particle *i* and **r** is the phase space for the position vectors of all particles on which the potential energy depends. The scale factors are defined based on variables *s* (dimensionless) and *V* (with dimension (length)^3). The last four terms in Eq. (2.7) originate from the additional variables and have the role of converting the micro-canonical ensemble into canonical or isothermal-isobaric ensembles. Variables p_s and p_V are the momentum conjugates for *s* and *V*, respectively. Parameters *Q* and *W* behave as masses for variables *s* and *V* with dimensions of (energy)×(time)^2 and (energy)×(time)^2×(length)$^{-2/3}$ and control the fluctuations of temperature and pressure, respectively. In other words, $p_{s=}$ *Qds/dt* and $p_{V=}$ *WdV/dt*. Quantity *g* is the number of degrees of freedom for particles inside the simulation cell, and P_{ex} is the desired external pressure on the simulation cell.

Based on the Hamiltonian defined in Eq. (2.7), the equations of motion are the following relations

$$\frac{d\mathbf{r}_i}{dt} = \frac{\partial H}{\partial \mathbf{p}_i} = \mathbf{p}_i / m_i V^{2/3} s^2 , \tag{2.8}$$

$$\frac{ds}{dt} = \frac{\partial H}{\partial p_s} = p_s / Q , \tag{2.9}$$

$$\frac{dV}{dt} = \frac{\partial H}{\partial p_V} = p_V / W , \tag{2.10}$$

$$\frac{d\mathbf{p}_i}{dt} = -\frac{\partial H}{\partial \mathbf{r}_i} = -\frac{\partial \Phi}{\partial \mathbf{r}_i} , \tag{2.11}$$

$$\frac{dp_s}{dt} = -\frac{\partial H}{\partial s} = \frac{\sum_i \mathbf{p}_i^2 / 2m_i V^{2/3} s^2 - gkT}{s} , \tag{2.12}$$

$$\frac{dp_V}{dt} = -\frac{\partial H}{\partial V} = \frac{\sum_i (\mathbf{p}_i^2 / 2m_i V^{2/3} s^2 - \frac{\partial \Phi}{\partial \mathbf{r}_i} \mathbf{r}_i)}{3V} - P_{ex} . \tag{2.13}$$

Solving this set of equations instead of the Newton's equations of motion, which conserve the energy and volume of the system and corresponds to an NVE ensemble, was proven (Nose, 1984) to provide an NPT ensemble.

2.1.1 Force fields utilized in this study

As explained earlier in this section, a force field is a necessary element in all MD simulations. In this subsection, the force fields that have been used in the MD simulations are explained. Since different materials are included in the MD simulations throughout this dissertation, force field for each material is given in a respective subsection.

2.1.1.1 Force fields for n-alkanes molecules

Various all-atom or united atom force fields exist for n-alkanes. OPLS (Optimized Potentials for Liquid Simulations (Jorgensen et al., 1984)), TraPPE (Transferable potentials for phase equilibria (Martin and Siepmann, 1998)), SKS (Smith, Karaborni and Siepmann, 1995) and NERD (Nath, Escobedo and de Pablo-revised (Nath et al., 1998)) have been examined to decide for the most appropriate existing force field to describe the thermal properties of n-alkanes. These force fields include similar functions for describing pairwise interaction, bond stretching, angle bending and dihedral torsion of such molecules. For the MD simulations of cases containing methane, the OPLS united-atom force field was used. In this force field, the CH_4 molecules are considered as pseudo-atoms among which the Lennard-Jones (LJ) potential acts. The LJ potential among particles *i* and *j* has the following form

$$U_{ij} = 4\varepsilon\left[\left(\frac{\sigma}{r_{ij}}\right)^{12} - \left(\frac{\sigma}{r_{ij}}\right)^{6}\right] \tag{2.14}$$

where ε and σ are the depth of the potential well and the finite distance at which the inter-particle potential is zero, respectively. Variable r_{ij} is the distance between particles *i* and *j*. For methane, σ and ε are 3.73 Å and 0.294 kcal/mol, respectively.

For n-octadecane molecules, the four force fields mentioned above were checked by obtaining the respective thermal conductivity values. It was found that the NERD potential is capable of describing the thermal transport properties of n-octadecane in addition to other thermo-physical properties well. It was also found that the shortcomings of other force fields originate from the fact that in those force fields rigid bonds are considered between atoms. The existence of rigid bonds rules out the significant contribution of bonds in heat transfer. It was observed that using those force fields reduces the thermal conductivity of n-octadecane to one tenth of the experimental value. Using the NERD potential, the calculated thermal conductivity values were in good agreement with the experimental values (this will be explained in detail in chapter 4).

The bond stretching part of the NERD potential reads as the following equation

$$U(r)/k_B = \frac{K_r}{2}(r - b_{eq})^2 \tag{2.15}$$

where K_r is 96,500 K/Å^2 and the equilibrium bond length, b_{eq}, is 1.54 Å.

The bond bending potential reads as

$$U(\theta)/k_B = \frac{K_\theta}{2}(\theta - \theta_{eq})^2 \tag{2.16}$$

where θ is the bond angle, K_θ is 62,500 K/rad^2 and the equilibrium bond angle, θ_{eq}, is 114.0°.

The torsional potential has the following form

$$U(\psi)/k_B = U_0 + U_1(1 + \cos\psi) + U_2(1 - \cos 2\psi) + U_3(1 + \cos 3\psi) \tag{2.17}$$

where U_0, U_1, U_2 and U_3 are 0, 355.04 K, -68.19 K and 701.32 K, respectively.

For pseudo-atoms that belong to different molecules or belong to the same molecules but at least four bonds away, the LJ potential describes the interacting forces. The ε and σ for CH_3 are 3.91 Å and 0.2059 kcal/mol, respectively, while for CH_2 those values are 3.93 Å and 0.0907 kcal/mol, respectively. The Lorentz-Berthelot mixing rule (Allen and Tildesley, 1987) is used for obtaining the LJ parameters among the CH_3 and CH_2 sites,

$$\sigma_{CH_2-CH_3} = \frac{\sigma_{CH_2} + \sigma_{CH_3}}{2}, \tag{2.18}$$

and

$$\varepsilon_{CH2-CH_3} = \left(\varepsilon_{CH_2}\varepsilon_{CH_3}\right)^{1/2}. \tag{2.19}$$

2.1.1.2 Force field for CNT/Graphene

For interpreting the interatomic potential among carbon atoms in CNT and graphene, a modified version of the Tersoff potential (Tersoff, 1988, 1989 and 1990) by Lindsay and Broido (2010) has been utilized. The Tersoff potential is a short-range empirical interaction potential which has been extensively used for different properties of single-walled CNTs (SWCNTs) and single-sheet graphenes. The form of this potential is convenient because it does not require defining bonds, angles and dihedrals. The Tersoff interaction potential for particles *i* and *j*, with the distance r_{ij} between the particles, reads as follows

$$U_{ij} = f_{ij}^{C}\left(a_{ij} f_{ij}^{R} - b_{ij} f_{ij}^{A}\right) \tag{2.20}$$

where

$$f_{ij}^{R} = Ae^{-\lambda_1 r_{ij}} \tag{2.21}$$

and

$$f_{ij}^{A} = Be^{-\lambda_2 r_{ij}} \tag{2.22}$$

where *A*, *B*, λ_1 and λ_2 are equal to 1893.6 eV, 346.74 eV, 3.4879 Å^{-1} and 2.2119 Å^{-1}, respectively. Quantities f_{ij}^{R} and f_{ij}^{A} account for repulsive and attractive forces, respectively, whereas f_{ij}^{C} is a cut-off term defined as follows

$$f_{ij}^{C} = \begin{cases} 1, & r_{ij} < R \\ \frac{1}{2}\left(1+\cos[\pi(r_{ij}-R)/(S-R)]\right), & \mathrm{R} < r_{ij} < S \\ 0, & r_{ij} > S \end{cases} \tag{2.23}$$

in which *R* and *S* are distances equal to 1.8 and 2.1 Å, respectively.

Functions a_{ij} and b_{ij} include range-limiting terms (terms that limit the range of interaction). The quantity a_{ij} is typically set to zero (Lindsay and Broido, 2010), whereas b_{ij} takes into account the bond angle for atoms around atom *i* and has the following form

$$b_{ij} = (1+\beta^{n}\zeta_{ij}^{n})^{-1/2n} \tag{2.24}$$

with

$$\zeta_{ij} = \sum_{k\neq i,j} f_{ij}^{C} g_{ijk} \exp(\lambda_3^3 (r_{ij}-r_{ik})^3) \tag{2.25}$$

and

$$g_{ijk} = 1+\frac{c^2}{d^2}-\frac{c^2}{d^2+(h-\cos(\theta_{ijk}))^2} \tag{2.26}$$

in which parameters β, *n*, *c*, *d*, *h* and λ_3 are equal to 1.5724×10^{-7}, 0.72751, 38049, 4.3484, -0.57058 and 0.0, respectively, and θ_{ijk} is the angle between bonds *ij* and *ik*.

The modification by Lindsay and Broido (2010) was made to the Tersoff potential, aiming to more accurately interpret the phonon dispersion of graphene and SWCNT, therefore, improving the MD or lattice dynamics simulations for thermal transport in such materials. Their parameterization lead to modifications in two parameters, *B* and *h*. Parameters *B* and *h* were optimized to be 430.0 eV and -0.930, respectively.

For the cross potential among the carbon atoms in CNT/graphene and interaction sites of n-octadecane, the Lorentz–Berthelot mixing rule was used for determining the LJ parameters among the n-octadecane sites and carbon atoms. The required LJ parameters for the carbon atoms in CNT and graphene for mixing calculations are extracted from the work of Walther et al. (2001).

In order to interpret the interactions among atoms in argon and copper, LJ potential was utilized. Parameters σ and ε for argon atoms are 3.405 $\dot{\text{A}}$ and $0.2381\,\text{kcal/mol}$, respectively (Verlet, 1967), while for copper atoms these are 2.34 $\dot{\text{A}}$ and $9.4512\,\text{kcal/mol}$, respectively (Halicioglu and Pound, 1975).

It should be noted that the cut-off radius utilized for the LJ interactions throughout this dissertation is taken to be equal to 2.5σ or 10 Å, depending on which one is bigger.

2.2 Methods for Determination of Thermal Conductivity

2.2.1 Equilibrium Molecular Dynamics Green-Kubo Method

Transport properties of materials can be determined by analysis of the fluctuating dynamical variables in equilibrium systems through utilizing the Green-Kubo relations (Kubo, 1957, and Vogelsang et al., 1987). This method has been widely utilized to predict the thermal conductivity of various systems using equilibrium molecular dynamics (EMD) simulations.

The Green-Kubo relation for thermal conductivity reads as

$$k_{ii} = \frac{V}{k_B T^2}\int_0^{\infty} < J_i(t) J_i(0) > dt, \quad i = x, y \text{ or } z. \tag{2.27}$$

The *i*-th diagonal component of the thermal conductivity matrix (k_{ii}) at temperature (*T*) is calculated by integrating over time the heat current autocorrelation function (HCACF) that is obtained from equilibrium molecular dynamics simulations. In Eq. (2.27), *V* is the volume of the simulation box that contains the system of particles, k_B is the Boltzmann's constant and ***J***(t) is the microscopic heat current.

2.2.2 Comment on the Heat Current in Multi-Component Systems

Considerable attempts have been made to study quantities included in both EMD Green-Kubo and non-equilibrium molecular dynamics (NEMD) methods, i.e. the heat current expression, to develop it for more complicated systems such as inhomogeneous (Todd et al., 1995) and multi-component systems (Bearman and Kirkwood, 1958, MacGowan and Evans, 1986, Vogelsang et al., 1987, Vogelsang and Hoheisel, 1987, Paolini and Ciccotti, 1987, Sindzingre et al., 1987, Li et al., 1998, and Pomeau, 1972). Among the terms included in the heat current expression for multi-component systems, the partial enthalpy term is sometimes neglected or not properly calculated, potentially leading to spurious results. Even when implemented correctly, the statistical errors can be significant (Sindzingre et al., 1987). First Pomeau (1972) (the term was referred to as “microscopic enthalpy”) and later Vogelsang et al. (1987) and Paolini and Ciccotti (1987) estimated the partial enthalpy to be the average of the kinetic energy, potential energy, and virial stress for each component, a method which has the advantage of being related to molecular expressions and leads to such terms during MD simulations. It should be noted that this definition of the partial enthalpy is still an estimation (Sindzingre et al., 1989) in the sense that it is an average quantity over all atoms for each species, which may not be identical for all atoms.

In particular, the EMD Green-Kubo method has been used (Keblinski et al., 2002, Eapen et al., 2007, Sarkar and Selvam, 2007, and Kang et al., 2011) for determining the thermal conductivity of nanofluids, which are highly inhomogeneous systems of solid nanoparticles suspended in liquids, and to elucidate the mechanism behind thermal conductance in such a system. Even though the “nanofluid” publications have typically reported significant thermal conductivity enhancements for well-dispersed nanofluids, they lack rigorous definition of the partial enthalpy terms in the heat current expression. Here, we try to demonstrate that the proper definition of partial enthalpy leads to the results obtained via the EMD Green-Kubo method that are consistent with the NEMD direct method (Schelling et al., 2002) results for various multi-component systems including a gas mixture, a liquid mixture, a solid alloy and a nanofluid. The origin of the possible spurious results when the incorrect partial enthalpies are used will be discussed. It will be also shown that for some multicomponent systems, such as solid alloys or liquid mixtures, even incorrect enthalpy definition has no or minor effects on the determination of the thermal conductivity.

The microscopic definition of the heat current is as follows

$$\mathbf{J}(t) = \overbrace{\frac{1}{V}\left[\sum_{j=1}^{N}\mathbf{v}_j E_j - \sum_{\alpha=1}^{2} h_\alpha \sum_{j=1}^{N_\alpha}\mathbf{v}_{\alpha j}\right]}^{Convective} + \overbrace{\frac{1}{V}\left[\frac{1}{2}\sum_{i=1}^{N}\sum_{j=1, j\neq i}^{N}\mathbf{r}_{ij}\left(\mathbf{v}_j . \mathbf{F}_{ij}\right)\right]}^{Virial}, \quad (2.28)$$

where $\mathbf{v}_j$ and E_j are the velocity and instantaneous energy of particle *j*, respectively. Quantities $\mathbf{r}_{ij}$ and $\mathbf{F}_{ij}$ are the displacement vector and interacting force between particles *i* and *j*, respectively. Parameter *N* is the total number of particles and N_α is the number of particles for species α (for simplicity, we assume only two species are present). Also, h_α denotes the average partial enthalpy of species α. Since the first term on the right hand side is the dominant term for gases in which the main thermal conductance mechanism is the convection of particles, and on the other hand, the second term is the dominant term for solids, the first term can be referred to as the “convective” term and the second term as the “virial” or “interaction” term.

For each species,

$$h_\alpha = \frac{\sum_{i=1}^{N_\alpha}\left[K_i + U_i + \frac{1}{3}\left(m_i v_i^2 + \frac{1}{2}\sum_{j=1}^{N}\mathbf{r}_{ij}.\mathbf{F}_{ij}\right)\right]}{N_\alpha} \quad (2.29)$$

where K_i and U_i are the time-averaged kinetic and potential energies of particles of species α, respectively. The first two terms constitute the internal energy (E_i) and the third term represents the *PV* term including the kinetic and interaction contributions. Such a definition is consistent with the thermodynamic definition of the enthalpy, $H = E + PV$. It should be noted that such a definition of the partial enthalpy is not an exact definition of the partial enthalpy as far as it has been calculated as an average quantity (Sindzingre et al., 1989). We also note that the calculated partial enthalpies by using Eq. (2.29) are the average over atoms in each species, and atoms in different regions of species may have slightly different values (e.g. the atoms located on the surface of nanopaticle and atoms at the center of nanoparticle). Subtracting the average enthalpies is necessary as such quantities represent energy that is not exchanged between the species, but is just silently carried around. In a single-component system, subtraction of the partial average enthalpy is inconsequential since the EMD simulation are performed subject to the condition of zero total momentum, which in a single-component system implies zero average velocity. In multi-component systems, the center of mass of species diffuses with respect to each other despite the zero total momentum.

2.2.3 NEMD direct method

In the direct method, a heat flux is imposed through the simulation box by adding heat to molecules inside a planar slab (heat source) in one region of the simulation box and extracting the same amount of heat from molecules inside another slab (heat sink) in a different region of the simulation box (Schelling et al., 2002). Figure 2.2 exhibits two possible configurations that can be used for establishing heat source/sink simulations for systems subjected to a periodic boundary condition. After reaching the steady-state condition in the studied system, based on the Fourier’s Law, the thermal conductivity of the material in the simulation box with the periodic boundary condition becomes $k = \dfrac{dQ/dt}{A(dT/dx_1 + dT/dx_2)}$, where dQ/dt is the time rate of heat addition or extraction from the heat source and heat sink, respectively. Quantity A is the cross-sectional area of the simulation box normal to the direction of imposed heat flux, whereas dT/dx_1 and dT/dx_2 are the temperature gradients of two sides of heat sink or heat source, respectively. It should be noted that for all cases studied in this dissertation, orthotropic thermal conductivity matrix is considered as it has been observed for similar materials investigated in detail by Rastgarkafshgarkolaei in his masters thesis (2014). It is also worth mentioning that in most of cases in this dissertation, we have homogeneity in the individual directions of simulation boxes which implies orthotropic properties.

A point should be noted in relation to the utilization of this method for crystalline or molecularly-ordered materials. As fully discussed by Schelling et al. (2002), in an NEMD direct method simulation of such structures, the size effect should be studied because of the phonon scattering at the regions in the vicinity of the source and sink. The thermal conductivities of systems with different sizes of the material should be obtained. Then, the inverse of the thermal conductivity vs. the inverse of the length of the simulation cell (*1/L*) should be plotted to extrapolate for *1/k* as $1/L \rightarrow 0$. In other words, for k as $L \rightarrow \infty$, a procedure extracted from the following expression for macroscopic thermal conductivity of crystals

$$\frac{1}{k}=\frac{1}{k_\infty}+\frac{C}{L} \tag{2.30}$$

is utilized where k_∞ is the macroscopic thermal conductivity and C is a constant related to the phonon group velocity and lattice spacing. Generally speaking, this relation originates from the fact that the inverse of the phonon average mean free path is a linear function of the inverse of the size of the system. For more details on derivation, the reader is referred to Schelling et al. (2002). The investigations by Sellan et al. (2010) hinted a limit on using the above-mentioned procedure for size effect study of the thermal conductivity. By using different methods including the EMD-based Green-Kubo method, the NEMD-based direct method and the Boltzmann transport equation (BTE)-based lattice dynamics method for evaluation of the thermal conductivity of different systems, they found that the systems with a minimum size equal to the largest mean free path of the effective phonon modes in thermal transport should be considered in the extrapolation procedure.

2.2.4 Comments on the Definition of Temperature in Classical MD

In classical MD, the temperature of a region in the simulation box at any time step is calculated based on the average kinetic energy of the particles contained in the region using the following equation

$$\frac{3}{2}k_BT = \frac{1}{N}\sum_{i=1}^{N}\frac{1}{2}m_iv_i^2 \tag{2.31}$$

in which $\frac{1}{2}m_iv_i^2$ is the kinetic energy of the atom with mass m_i and velocity v_i and *N* is the number of atoms in the region of interest.

In regard to this definition of temperature, two main issues arise especially for crystalline solids (Cahill et al., 2003). Firstly, this definition originates from the assumption of having all the vibrational modes equally excited. This is associated with the equipartition theorem in which the classical statistical mechanics relates the temperature of a system at thermal equilibrium to its kinetic energy. However, from the quantum mechanics treatment of phonons the excitations of different modes are not necessarily equal and for mode with frequency ω_i the excitation is $\frac{1}{\exp(\hbar\omega_i / k_BT) - 1}$. Then, it follows that when $\hbar\omega_i \le k_BT$ (usually $\hbar\omega_i < \frac{k_BT}{2}$ is used instead) mode ω_i is fully excited. It means that for any mode, there is a temperature above which the classical treatment or full excitation is correct. Commonly, a collective quantity which is called the Debye temperature is used for the classical treatment of all modes. For cases studied in this dissertation, the temperatures are high enough to consider the classical treatment of phonons.

The second issue arises when there is a temperature gradient or sharp change within the simulation box which is encountered in non-equilibrium calculations. The problem is associated with the fact that for defining temperature in any region, the atoms should be in local equilibrium. Since the particles get redistributed in distances corresponding to their mean free paths, in order to define a temperature within a region its length should be longer than the mean free path of particles. It should be noted that phonons with different frequencies and polarizations potentially possess different mean free paths. However, an effective mean free path can be considered for the modes having the higher contributions in thermal transport. In this dissertation, it is assumed that local equilibrium occurs for the regions where temperature is calculated.

2.2.5 Validation of the EMD Green-Kubo Method

In this section, four different model structures are considered to validate the results based on the EMD Green-Kubo method against those of the NEMD direct method. Specifically, (a) a methane-copper nanofluid at T=110 K including a copper nanoparticle occupying 0.35% of the system's volume, (b) a 50-50 "argon" gas mixture at T=1,000 K and P=175 atm, (c) a 50-50 liquid mixture at T=85 K and atmospheric pressure and (d) a 50-50 solid "argon" alloy at T=40 K and atmospheric pressure are studied. The argon interaction potentials are chosen for gas and liquid mixtures and the solid alloy. One of the species in all argon-based mixtures is regular argon, and the other species is the argon atom with a mass equal to ¼ of the mass of regular argon atoms. The Lennard-Jones (LJ) potential was chosen for intermolecular interactions among all pairs of particles. The LJ parameters, σ and ε, for argon atoms are 3.405 Å and $0.2381\,\text{kcal/mol}$, respectively (Verlet, 1967), whereas for copper atoms these quantities are 2.34 Å and $9.4512\,\text{kcal/mol}$, respectively (Halicioglu and Pound, 1975). For methane molecules, the Optimized Potentials for Liquid Simulations (OPLS) united-atom force field was used (Jorgensen et al., 1984). In this force field, CH_4 is taken as a single interaction site (united atom) for LJ interactions. The LJ parameters, σ and ε, for methane united atoms (i.e. without explicit hydrogen) are 3.73 Å and $0.294\,\text{kcal/mol}$, respectively. For the nanofluid case, the Lorentz-Berthelot mixing rule (Allen and Tildesley, 1987) was used for determining the LJ parameters between the methane and copper atoms. In the Green-Kubo-based calculations, the nanofluid system was made by carving a sphere of diameter 12.7 Å out of an FCC (face-centered cubic) copper crystal which leads to 87 copper atoms nanoparticle that was dissolved in 4,612 methane atoms. In the direct method-based calculations, the simulation box was doubled in all directions and included eight nanoparticles. Snapshots of the nanofluid system along with binary systems with different phases are shown in Figure 2.3.

The time step for all simulations was 1 fs. In the nanofluid case, the system was initially run for 200,000 time steps under the isothermal-isobaric (NPT) ensemble at atmospheric pressure and 110 K and then equilibrated under the NVE (constant volume and energy) ensemble for 200,000 time steps. The NVE simulations were continued for an additional 1,000,000 time steps over which the fluctuating heat current data were collected every 5 ps. For all binary mixture cases, the systems were thermalized under the NVT condition for 300,000 time steps and then equilibrated under the NVE condition for 300,000 time steps. The initial density of gas systems were taken about the density of an ideal gas at T=1,000 K and P=175 atm. Values of HCACFs were calculated for a time step of 5 fs. For the liquid, solid and nanofluid cases, the HCACF curves were obtained by averaging over 8 different simulations having different initial velocity distributions, whereas for the gas systems, the averaging process was done over 16 different simulations because the thermodynamic properties in gases exhibit greater fluctuations in MD simulations. The HCACF and thermal conductivity of pure methane and the Cu-methane nanofluid are shown in Figure 2.4. The HCACF and thermal conductivity of regular mass and mixture systems at different phases are shown in Figures 2.5-7. For all cases corresponding to the results presented in these figures, the initial value (at t=0) of the HCACF for two-component systems assume greater values when compared to the pure systems. However, this behavior does not necessarily lead to higher thermal conductivity values. The other important element which influences the value of the thermal conductivity is the time period over which the HCACF curves converge to zero. This convergence time period is related to the relaxation time for collisions of heat carrier particles (could be atoms or phonons). The HCACF curves corresponding to the liquids (both methane and argon) and nanofluid cases decay to zero faster than the ones for the solid and gas cases. This is consistent with the typical small relaxation time for atoms in liquid phase, where the correlation between the momentums of molecules last a short time (of the order of 1 ps). For the solid cases, the HCACF curve for the mixture case converges faster than the one for the pure case. This observation is in agreement with the phenomenon known as the phonon scattering in solids due to impurities. In a solid with a perfect arrangement of atoms (perfect crystal), vibrational waves (phonons) are the dominant heat carriers in the system. The relaxation time for phonons in a perfect crystal is relatively long, whereas for amorphous solids or crystals with impurities the phonon scattering decreases the relaxation time dramatically.

In the direct method-based simulations, all systems were thermalized and equilibrated in a similar way to the Green-Kubo cases and an appropriate heat flux was imposed on systems under the NVE conditions. Upon the application of a heat flux, the steady-state temperature profiles were attained after about 500,000 time steps and the temperature gradients were obtained by averaging the temperature profiles over 500,000 to 1,000,000 time steps. An example of the temperature profiles obtained in such a manner for the pure liquid and nanofluid are shown in Figure 2.8. The temperature profiles highly coincide with each other except for a minor difference close to the heat source regions. The temperature profiles do not exhibit distinct step changes for the nanofluid corresponding to the location of the nanoparticle.

2.2.6 Results and Discussion

In Table 2.1, the thermal conductivity values predicted by the Green-Kubo and direct methods for the pure liquid and the nanofluid are given. The thermal conductivity values obtained via both methods are in good agreement. The predicted thermal conductivity enhancement by the direct and Green-Kubo methods are very small to negligible. These results suggest that the enhancements of thermal conductivity of well-dispersed nanofluids reported in some EMD simulations are likely to be spurious rather than real.

The various components of the thermal conductivity originating from dividing the heat current term into the convective and virial components (Eq. (2.27)) are also provided in Table 2.1. For both cases of the pure fluid and the nanofluid, the virial term (*VV*) makes the dominant contribution to the thermal conductivity values. The convective term (*CC*) for the nanofluid case has a bigger value than the convective term of the pure liquid, but its magnitude is quite small comparing to the *VV* term and therefore does not lead to an anomalous thermal conductivity enhancement. The cross terms (*CV* and *VC*) are both small comparing to the virial terms.

The origin of the convective term is in the diffusion of the center of mass of each species. The components of the convective term originate from the autocorrelation function of the kinetic contribution $(\sum_{j=1}^{N} K_j \mathbf{v}_j)$, potential contribution $(\sum_{j=1}^{N} U_j \mathbf{v}_j)$ and partial enthalpies contribution ($\sum_{\alpha=1}^{2} h_{\alpha} \sum_{j=1}^{N_{\alpha}} \mathbf{v}_{\alpha j}$) terms in the heat current expression (Eq. (2.27)). It is observed that the time integral of the autocorrelation function of the kinetic term (*KK*) is very small comparing to the high values of the time integral of the autocorrelation function of the potential and partial enthalpy terms (*UU* and *HH*, respectively). The observed high values of the *UU* and *HH* terms (to be discussed in chapter 3) suggest that the manner in which the partial enthalpies are defined is very important in the prediction of overall thermal conductivity enhancement. The proper definition of the partial enthalpies (Eq. (2.29)) that leads to the time integral of the autocorrelation function for the *U-H* term (here called *U'U'*) does not result in a high value of the convective term and consequently high thermal conductivity enhancement. In other words, the potential term (in Eq. (2.28)) is mostly canceled out by the partial enthalpy terms.

To further validate our methodology, we present thermal conductivity results for atomic mixtures for gas, liquid and solid phases in Table 2.2. For the pure solid cases, the size effect was studied and the macroscopic thermal conductivity value was obtained by following the procedure explained in section 2.2.3. As an example, for the regular-mass argon solid, the plot of *1/k* vs. *1/L* is shown in Figure 2.9. In this plot, a straight line has been fitted to the data. Then, the value of the thermal conductivity is calculated by taking the inverse of the extrapolated value at *1/L*=0 and converting it to the desired units.

According to the data presented in Table 2.2, the predicted values of the thermal conductivity obtained via the direct and Green-Kubo methods are generally in good agreement. However, the results for pure gas and particularly gas mixture cases show noticeable discrepancy. It should be mentioned that the thermal conductivity predictions for the pure cases with the ¼ reduced mass (not given here) are two times greater than for pure cases with regular mass atoms, which is in agreement with time scaling argument.

The values of thermal conductivity of both gas and liquid mixtures fall between the two thermal conductivity values of pure cases with regular and reduced masses, while for the solid case, the value of the thermal conductivity of the mixture falls below the thermal conductivity of pure case with the regular mass. This distinct behavior of the solid system can be attributed to mass disorder scattering of phonons responsible for the high value of the thermal conductivity of crystalline solids. In gas systems, convection is the dominant mechanism of heat conduction as shown in Table 2.2, whereas in liquid and solid systems, the atomic interaction-related *VV* terms make the major contribution to the thermal conductivity values.

To provide further insight into the role of the partial enthalpy and the convective terms associated with diffusion of the centers of mass of species, the integrals of the center of mass velocity autocorrelation functions for each species is presented in Figure 2.10. Such autocorrelation functions yield the corresponding diffusion constants. The diffusivities of the gas system have the highest values, which is consistent with the large mean path of atoms between collisions. By contrast, the solid diffusivity is zero since atoms of solids only vibrate and do not diffuse. Interestingly, the diffusivity of the nanoparticle in the nanofluid case is roughly 50 times the diffusivity of the center of mass of species in the liquid mixture case. This is likely associated with the fact that the atoms aggregated into a sphere (i.e. a well-dispersed nanofluid) experience much lower friction (drag) force from the fluid compared to the case of the individual atoms dispersed in the fluid (case of a liquid mixture).

2.3 Summary and Conclusions

In summary, we performed EMD Green-Kubo calculations to predict the values of thermal conductivity of different multi-component systems including a nanofluid, gas and liquid mixtures and a solid alloy. The EMD-based predicted values of the thermal conductivity were in good agreement with the NEMD-based calculated thermal conductivities for each system. Our investigations indicate that the thermal conductivity values determined via the EMD simulations in the cases of well-dispersed nanofluids and gas mixtures are very sensitive to the correct definition of the average partial enthalpy terms used in the heat current formula. This is associated with the relatively high value of the center of mass diffusion coefficient for the species involved. In case of the liquid mixtures, value of diffusion is much lower and determination of the thermal conductivity, even with the incorrect average enthalpy definition does not lead to significant errors. In the case of the solid mixtures, the enthalpy definition is inconsequential as there is no diffusion.

Table 2.1 Predicted values of the thermal conductivity (W/m K) for the pure liquid and nanofluid based on the Green-Kubo and Direct methods.

	Direct method	*Green-Kubo method*				
	k_{total}	k_{total}	k_{CC}	k_{CV}	k_{VC}	k_{VV}
Pure liquid	0.153±0.001	0.154±0.003	0.0067	0.0147	0.0117	0.121
Nanofluid	0.150±0.003	0.159±0.002	0.0161	0.0108	0.0110	0.1225

Table 2.2 Predicted values of the thermal conductivity (W/m K) for the pure and 50-50 gas, liquid and solid mixtures based on the Green-Kubo and Direct methods.

	Direct method	*Green-Kubo method*				
	k_{total}	k_{total}	k_{CC}	k_{CV}	k_{VC}	k_{VV}
Gas, pure	0.045±0.004	0.040±0.004	0.037	0.001	0.002	0.0001
Gas, mixture	0.055±0.009	0.071±0.002	0.066	0.002	0.002	0.0002
Liquid, pure	0.132±0.002	0.138±0.004	0.004	0.011	0.011	0.1120
Liquid, mixture	0.139±0.004	0.146±0.003	0.005	0.011	0.011	0.1213
Solid, pure	0.345±0.004	0.316±0.003	0.001	0.015	0.013	0.2854
Solid, mixture	0.132±0.001	0.149±0.001	0.001	0.005	0.007	0.1338

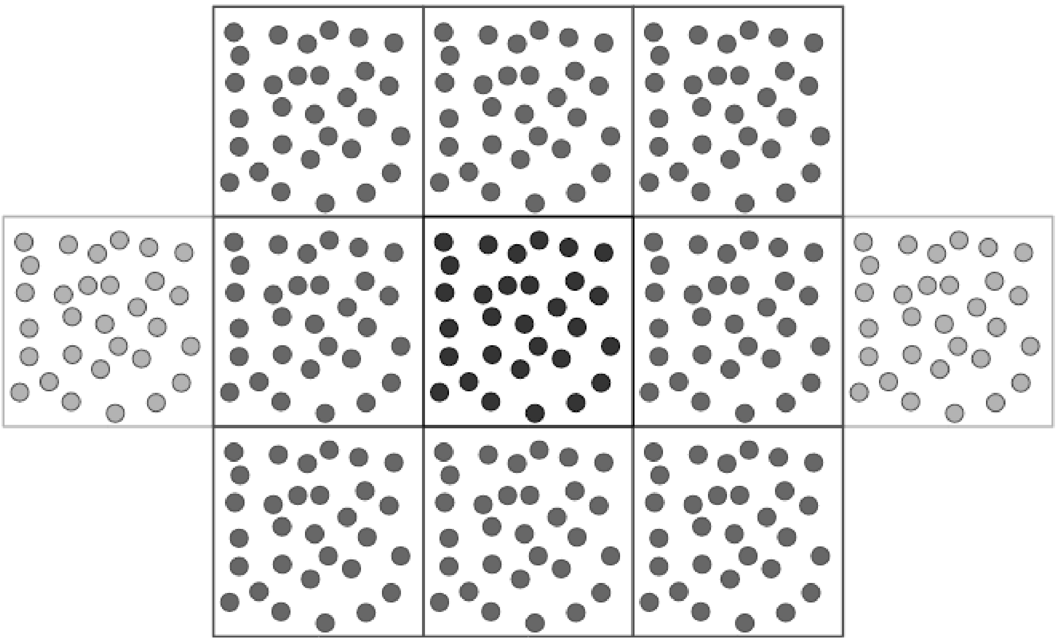

Figure 2.1 Schematic representation of the periodic boundary condition for a 2-dimensional case applied on all sides (Rapaport, 2004).

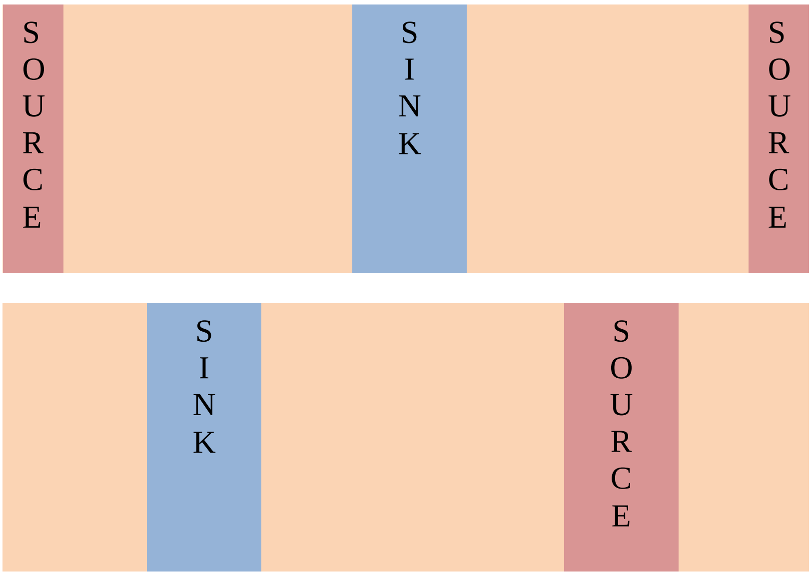

Figure 2.2 Possible configurations for a direct method heat source/sink simulation of a system subjected to a periodic boundary condition.

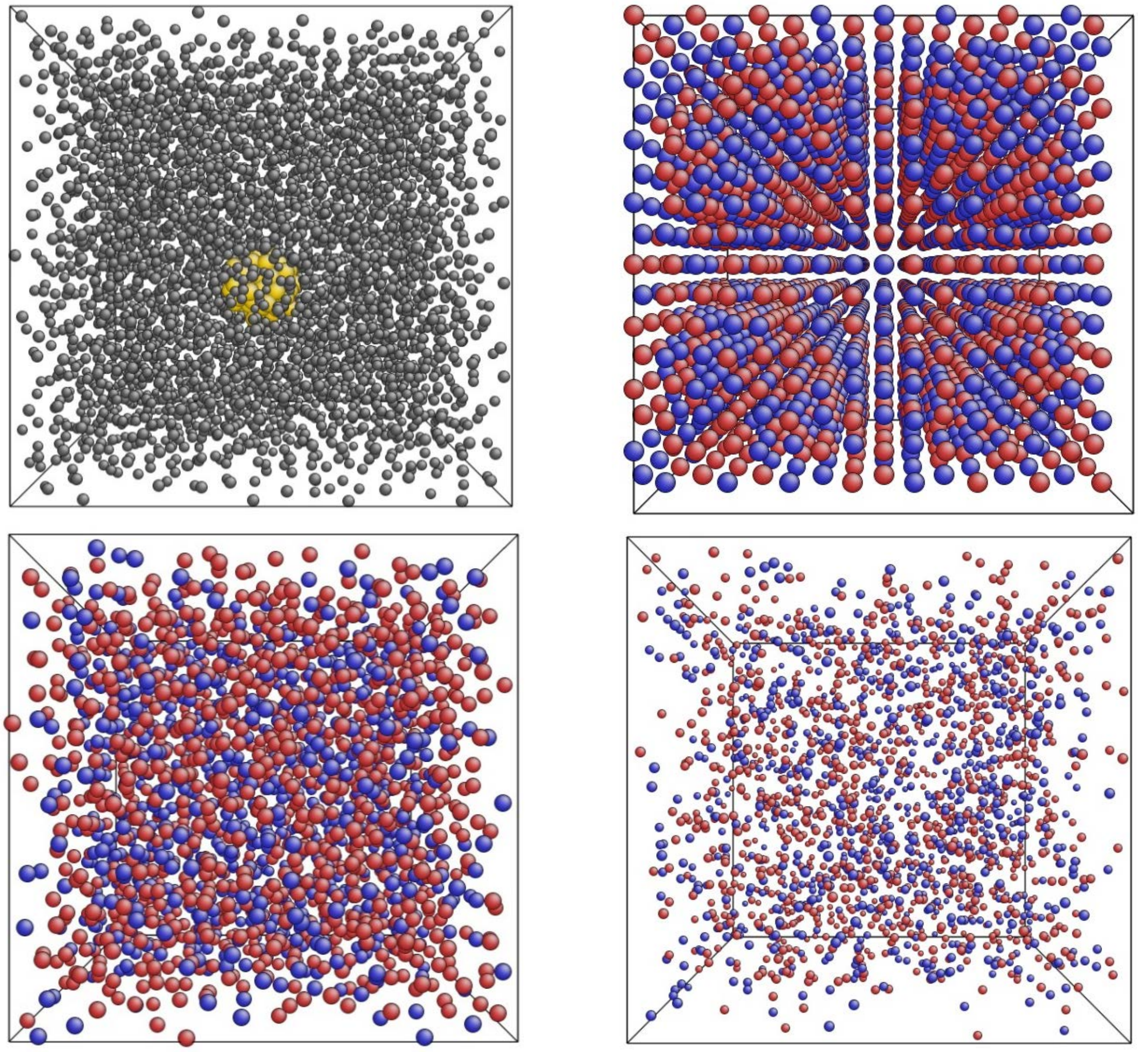

Figure 2.3 Snapshots of the nanofluid (top left), the solid mixture (top right), the liquid mixture (bottom left) and the gas mixture (bottom right) systems.

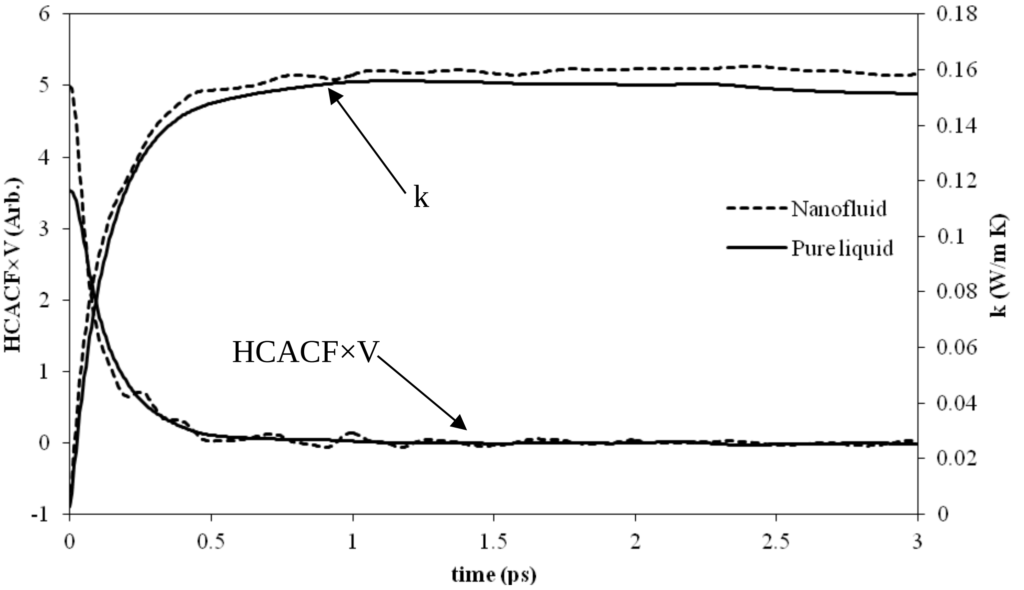

Figure 2.4 Values of the volume-normalized HCACF and thermal conductivity of pure liquid and nanofluid as functions of the time step.

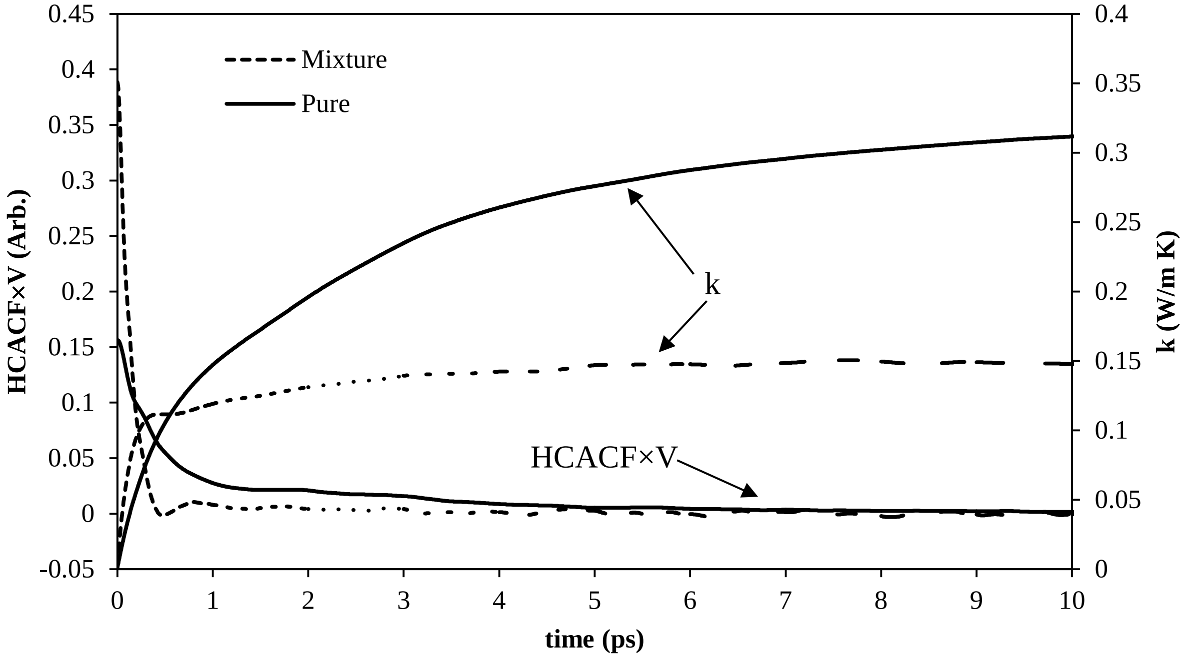

Figure 2.5 Values of the volume-normalized HCACF and thermal conductivity of pure solid and mixture systems as functions of time.

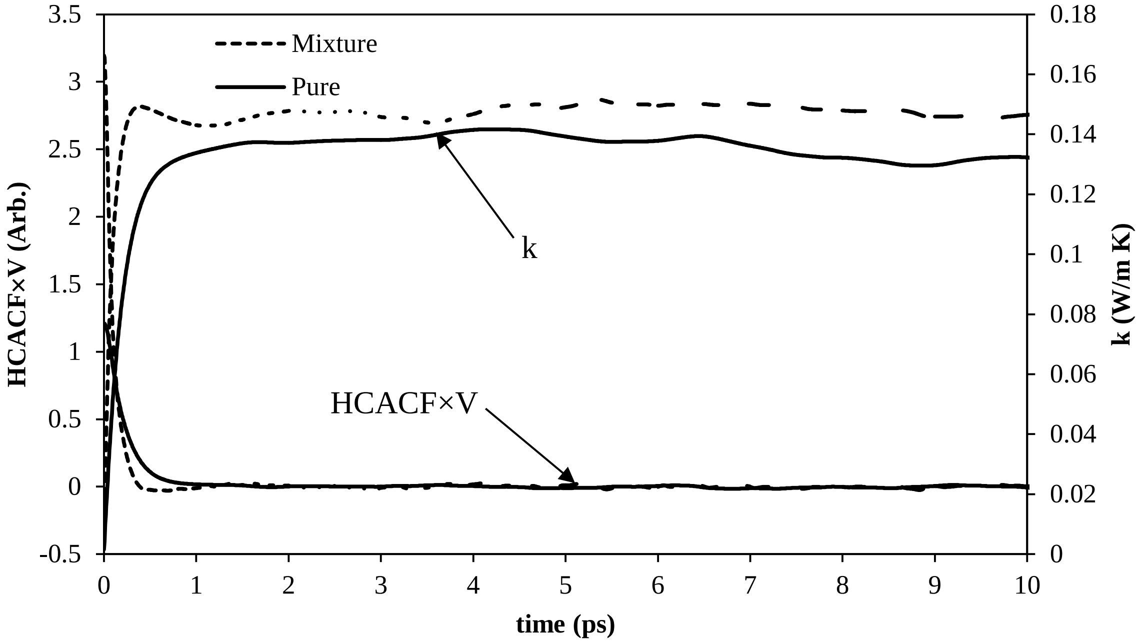

Figure 2.6 Values of the volume-normalized HCACF and thermal conductivity of pure liquid and mixture systems as functions of time.

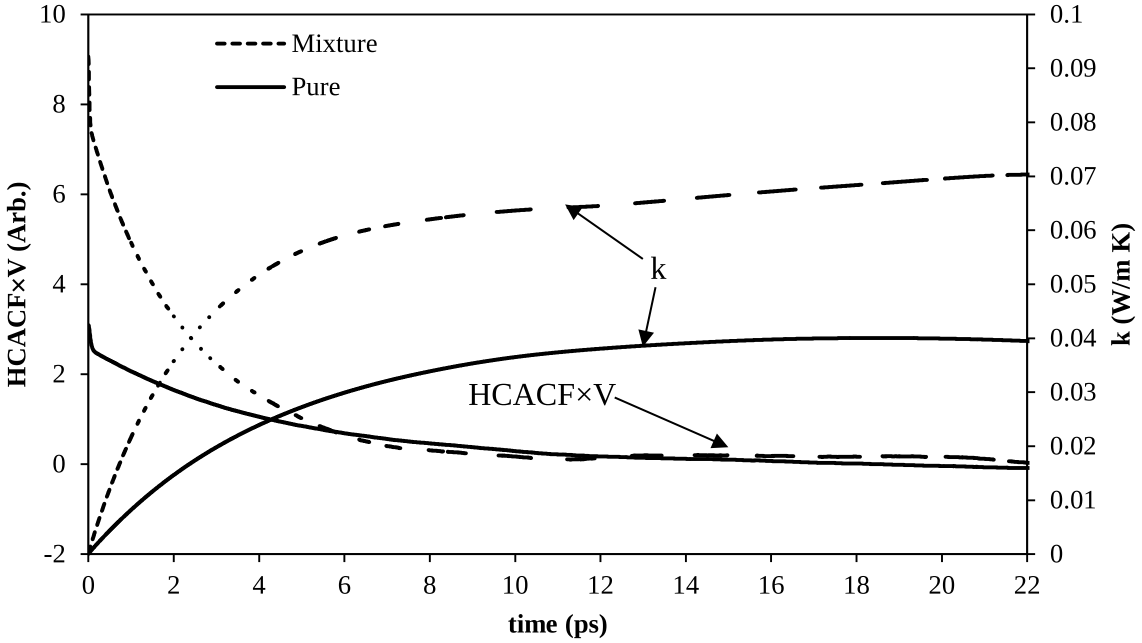

Figure 2.7 Values of the volume-normalized HCACF and thermal conductivity of pure gas and mixture systems as functions of time.

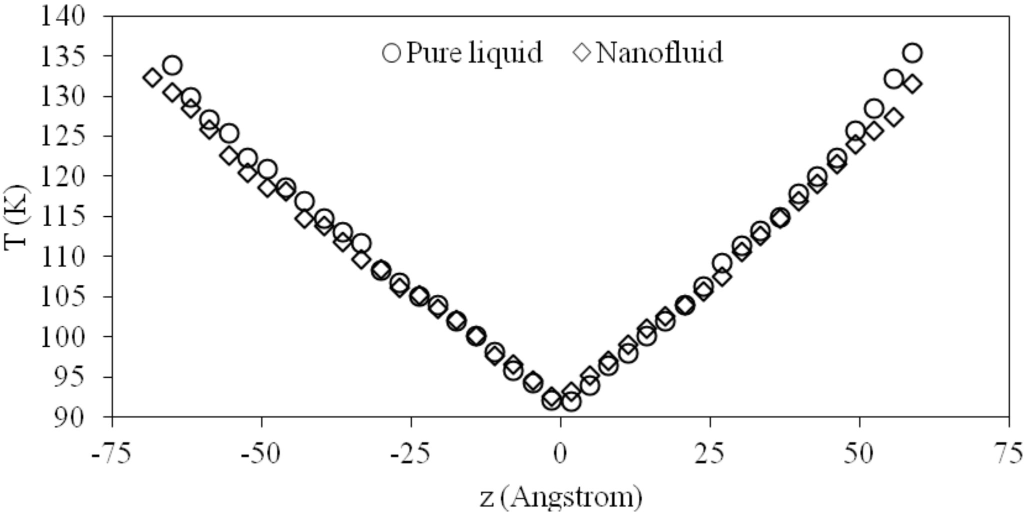

Figure 2.8 Steady-state temperature profiles for pure liquid and the nanofluid extracted from application of the direct method.

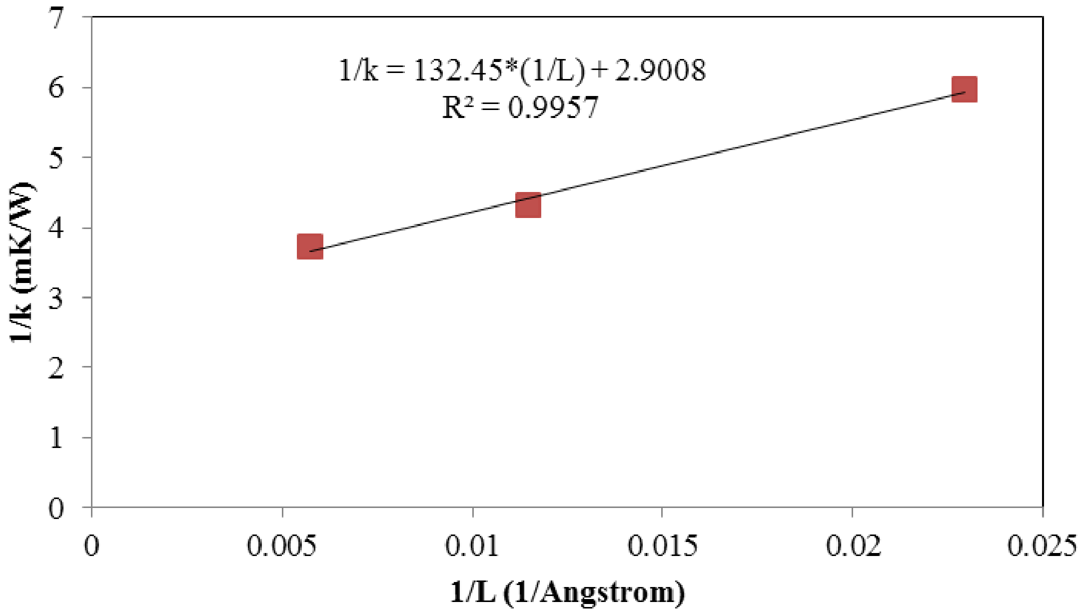

Figure 2.9 Inverse of the MD-derived thermal conductivity values against inverse of length of the side of the simulation box for solid argon.

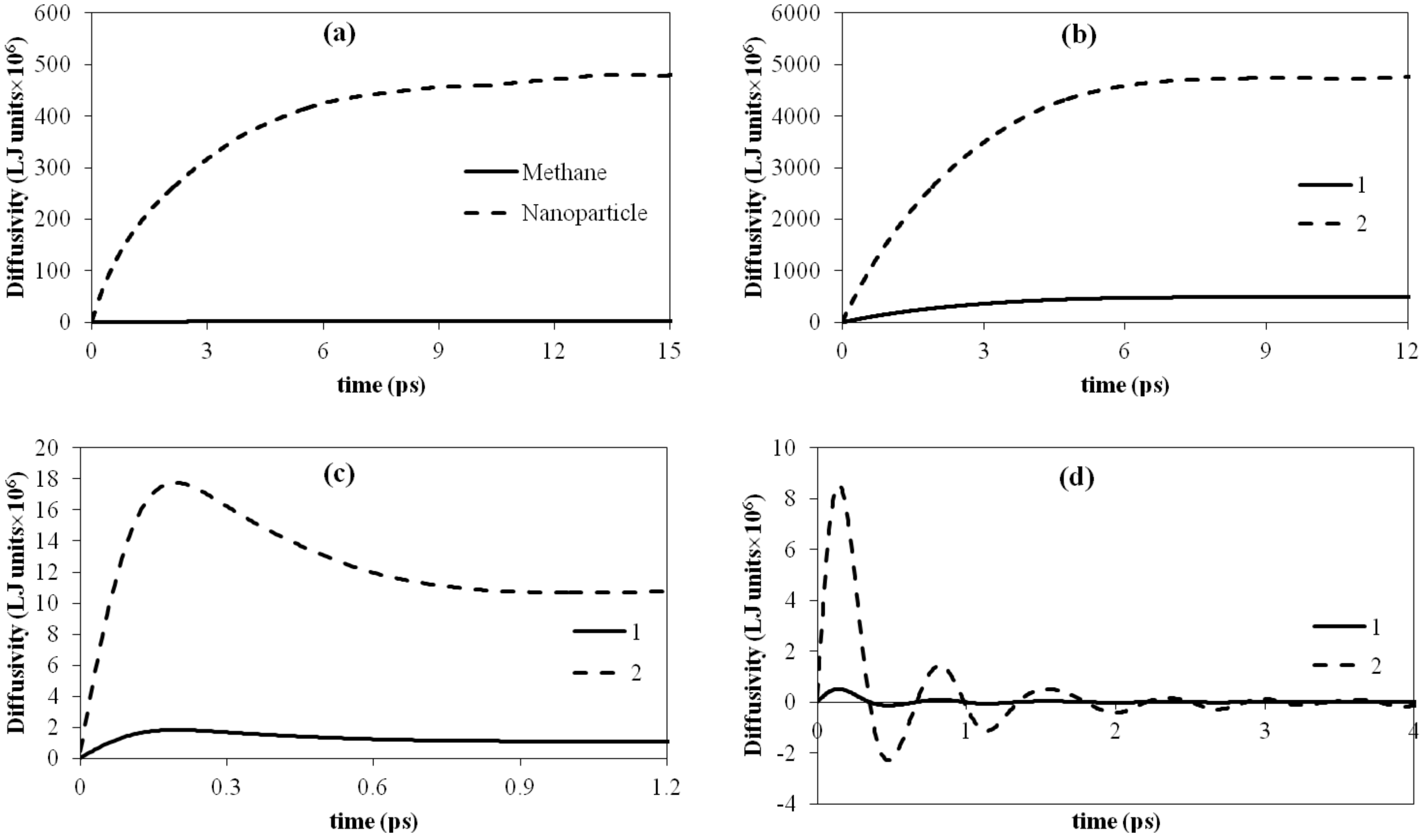

Figure 2.10 Diffusion coefficients of the centers of mass of different components in (a) nanofluid, (b) argon gas mixture, (c) argon liquid mixture and (d) argon solid mixture. Species 1 and 2 refer to the argon atoms with regular and ¼-reduced masses, respectively.

Chapter 3 Thermal Conductivity of Nanofluids

In this chapter, equilibrium molecular dynamics simulations are utilized to investigate the role of micro-convection on the thermal conductivity of well-dispersed nanofluids. It will be demonstrated that while the individual terms in the heat current autocorrelation function associated with the diffusion of nanoparticles achieve significant values, these terms essentially cancel each other if correctly-defined average enthalpy expressions are subtracted. Otherwise, erroneous thermal conductivity enhancements will be predicted that are widely attributed to the Brownian motion-induced micro-convection. Consequently, micro-convection does not contribute noticeably to the thermal conductivity and the predicted thermal conductivity enhancements are consistent with the effective medium theory.

3.1 Introduction

The thermal conductivity enhancement brought about by suspending nanoparticles in a fluid has been a highly-debated topic for more than a decade. Two main mechanisms of thermal conductivity enhancement have been reported, i.e. aggregation of nanoparticles into clusters and the Brownian motion-induced micro-convection. The argument by the first group of researchers (Keblinski et al., 2002, Buongiorno et al., 2009, Prasher et al., 2006, Prasher et al., 2006, Eapen et al., 2007, Keblinski et al., 2008, Gharagozloo et al., 2008 and 2010, and Gao et al., 2009), who reason that clustering is the mechanism explaining the high thermal conductivity enhancement of nanofluids, is that in well-dispersed nanofluids, the thermal conductivity enhancement just follows the effective medium theories for well-dispersed mixtures of spherical nanoparticles. Greater thermal conductivity enhancements are then explained by the aggregation/agglomeration of nanoparticles creating high aspect-ratio particles and/or networks of conductive particles. In both cases, the effective medium theory based simply on conduction explains the observed behavior (Eapen et al., 2007). The other group of researchers has identified the Brownian motion of nanoparticles as the origin of the observed anomalous thermal conductivity enhancement. Early studies, such as those by Kumar et al. (2004) and Bhattacharya et al. (2004), pointed to the direct influence of the Brownian motion on the thermal conductivity. Later on, convection introduced by the Brownian motion of either a single nanoparticle or multiple nanoparticles were identified as the major mechanism of thermal conductivity enhancement in nanofluids (Jang and Choi, 2004, Chon et al., 2005, Prasher et al., 2005, Prasher et al., 2006 and Sarkar and Selvam, 2007). Due to the temperature and particle size dependence of the Brownian motion, many researchers have studied the variation of thermal conductivity with the particle size and temperature (Kumar et al., 2004, Jang and Choi, 2004 and Chon et al., 2005).

In particular relevance to this investigation, some researchers performed equilibrium molecular dynamics (EMD) simulations and reported significant contributions of “micro-convection” to thermal transport (Sarkar and Selvam, 2007), or claimed that “convection” of the interfacial (particle-fluid) interaction energy contributes significantly to thermal conductivity (Eapen et al., 2007). On the other hand, results of studies that utilized direct method simulations, whereby a heat source and sink are introduced to create a heat flux and the associated temperature gradient (Evans et al., 2003), demonstrated thermal conductivity enhancements perfectly consistent with the effective medium theory predictions indicating that micro-convection plays no role. In this chapter, the above-discussed discrepancy is addressed in great detail, emphasizing issues that arise when EMD simulation is used for determining the thermal conductivity of nanofluid multi-component systems. Different contributing components to the thermal conductivity obtained via EMD simulations are evaluated and the terms that can lead to erroneous high thermal conductivities are identified. Furthermore, it is proven that for well-dispersed nanofluid systems, these high-value micro-convection-induced components of the thermal conductivity cancel each other. In effect, the shortcoming of a number of previous EMD simulations that report anomalous high values of thermal conductivity is highlighted.

This chapter starts with a literature review. Then, the effective medium theory-based models for predicting the thermal conductivity of nanofluids are reviewed. In the next sections, the MD calculations for determining the effect of nanoparticles on the thermal conductivity of fluids are presented. These sections contain discussions of the pertinent methodology, models and the results of MD simulations.

3.2 Literature Review

Over the last two decades, realizing and explaining the observed thermal conductivity enhancement through suspending nanometer-size particles in fluids has been a struggling topic in academia and has attracted attention of many researchers and scientists. The first paper that noted the enhancement of thermal conductivity of nanofluids was the one by Masuda *et al.* (1993). Two years later, Choi (1995) who was the first to name the suspension of nanoparticles as *nanofluid*, also reported thermal conductivity enhancement in nanofluids. Wang *et al.* (1999) investigated the thermal conductivity enhancement of suspensions of Al_2O_3 and CuO nanoparticles in four different base fluids including water, pump fluid, engine oil, and ethylene glycol. They also observed the higher thermal conductivity of nanofluids with respect to the base fluids. They compared their experimental results with the theoretical models and upon observing the deficiencies of those models, they were the first researchers to investigate the underlying heat transfer mechanisms in nanofluids. Lee et al. (1999) showed that the model of Hamilton and Crosser (1962) can predict the experimentally-observed thermal conductivity enhancement of Al_2O_3 nanofluid but cannot predict the thermal conductivity enhancement observed in a CuO-based nanofluid. They reported a thermal conductivity enhancement of about 20% for a 4% volume fraction of 35 nm in diameter CuO nanoparticles dispersed in ethylene glycol.

Anomalous thermal conductivity enhancement of copper nanoparticles suspended in ethylene glycol was reported by Eastman et al. (2001), which is the first nanofluid containing metal nanoparticles, thus opening a new chapter in nanofluid investigations and promoted further attempts to reveal the dominant mechanisms and underlying physics of heat transfer in nanofluids. They reported a thermal conductivity enhancement of up to 40% in nanofluids with nanoparticle volume fractions less than 0.5% which is far beyond the predictions based on the Maxwell's model (see Figure 3.1).

Keblinski et al. (2002) suggested four possible major mechanisms for the observed anomalous enhancement of thermal conductivity, i.e. the Brownian motion of the particles, ordered layering of liquid molecules at the liquid/nanoparticle interface, heat transport within the nanoparticles, and the clustering (agglomeration) of nanoparticles. Through a time-scale study of both heat transfer in the liquid and the Brownian motion of particles, they showed that the effect of the Brownian motion does not adequately explain the observed enhancement. To verify this, molecular dynamics (MD) simulations were also utilized. Nearly-identical heat current autocorrelation functions extracted from the MD simulations for two cases with and without constrained center of mass verified the previous finding that the Brownian motion has a minor influence on thermal conductivity enhancement. Soon thereafter, the effect of the Brownian motion on heat transport of nanofluids became one of the highly-debated topics in thermal physics. This paper also encouraged researchers to further pursue experimental and numerical investigations of each of these mechanisms, modify the mechanisms, or add other possible mechanisms. They also ruled out the effect of the liquid layering at the interface by arguing that the required thickness of the liquid layer with the similar crystalline structure to the solid particles to meet the enhancement from theoretical models is around 2.5 nm, while the existing experiments and simulations had shown that the thickness of the layer is only 1 nm. As for the effect of the nature of thermal transport in nanoparticles, phonon diffusion was shown insufficient to explain the enhancement because the phonon mean free path is greater than the size of nanoparticles which results in the lack of phonon modes that can highly contribute to thermal transport. However, the ballistic phonon effect remained a viable contributor to the increase in thermal conductivity, especially when the ballistic phonons can reach nearby particles through the short-phonon-mean free path-liquid medium. The fourth mechanism was identified as the local clustering (agglomeration) of nanoparticles. Upon clustering, more effective heat conductive paths are formed in the nanofluid, which is suggested as a reason for the thermal conductivity enhancement in nanofluids. Research papers following Keblinski et al. (2002) placed more attention into investigating and evaluating the significance of each mechanism or bringing new mechanisms into focus.

Xuan et al. (2003) assigned the main role to the Brownian motion and an inverse decreasing role to the aggregation of nanoparticles. They modified an existing stationary theoretical model by introducing the effect of the Brownian motion. The observed decreasing role of aggregation was also indirectly proved by the Brownian motion. They simply explained it by the following statement: *Having smaller particles leads to higher speed of nanoparticles and therefore higher thermal conductivity values due to more effective interactions among nanoparticles* (taken from Xuan et al., 2003). They validated their proposed model by comparison to experimental data for the thermal conductivity of a Cu-water nanofluid. They pointed out that the degree of enhancement increases by raising the temperature of the sample, which was another evidence for them to prove the effect of the Brownian motion. Das et al. (2003) investigated the effect of temperature on the thermal conductivity enhancement of nanofluids with water as the base fluid and Al_2O_3 and CuO as the nanoparticles. It was shown that the thermal conductivity enhancement was realized by increasing the temperature. The temperature effect was more noticeable for the smaller size of the CuO nanoparticles. Kumar et al. (2004) claimed a comprehensive model which included the observed dependencies of enhancement on the volume fraction of nanoparticles, temperature of nanofluid and size of particles. They based their model on two aspects: first, the thermal conductivity of a mixture of stationary particles in the base fluid, and second the thermal conductivity due to the random motion of nanoparticles. They explained the observed dependencies on the temperature of nanofluid and the size of nanoparticles in the thermal conductivity enhancement to be due to the Brownian motion. By using the kinetic theory expression for the thermal conductivity, i.e. $k_p = \frac{1}{3} n l v c_p$ (where n is the particle number density, l is the particle mean free path, v is the average velocity of particles and c_p is the heat capacity per particle) for the Brownian motion of nanoparticles, and substituting the mean velocity of nanoparticles into the equation, they proposed that the thermal conductivity enhancement is proportional to the temperature of nanofluid and inversely proportional to the radius of nanoparticles. Later, Keblinski and Cahill (2005) wrote a one-page comment on the paper of Kumar et al. (2004) and showed that the expression of mean velocity of nanoparticles (gold nanoparticles was used in Kumar et al., 2004) that they had utilized is not correct and the Brownian motion contribution based on the correct velocity is orders of magnitude smaller than the thermal conductivity of a common base fluid (water was the base fluid in Kumar et al., 2004). Jang and Choi (2004) introduced a new model which accounts for a new mechanism. The new mechanism was the convection due to the Brownian motion of individual nanoparticles. In this mechanism, the Brownian motion of the nanoparticles does not directly augment the thermal transport within the nanofluid through their interactions with each other. Instead, in an indirect manner, the Brownian motion of nanoparticles induces convection in the base fluid which itself leads to enhancement in thermal transport (see Figure 3.2). Moreover, in this paper a new model explaining the effect of temperature and particle size was introduced. Chon et al. (2005) correlated an empirical model to the experimental data of thermal conductivity of Al_2O_3 nanofluid. They also observed the increase of thermal conductivity enhancement with increasing temperature and decreasing particle size and explained it to be due to the Brownian motion (see Figure 3.3 for the correlation function and selected graphs). Prasher et al. (2005 and 2006) extended the idea of the Brownian motion-induced convection of single nanoparticles to multiple nanoparticles. They proposed a correlation for the heat transfer coefficient based on the Reynolds number, the Prandtl number, nanoparticle diameter and volume fraction (see Figure 3.4). They compared their semi-empirical Brownian model with the experimental data of Lee et al. (1999) and Das et al. (2003), which were both for Al_2O_3 nanofluids.

Keblinski et al. (2008) published a paper to conclude the past arguments and discussions on the dominant mechanisms governing thermal transport in nanofluids. They concluded that the observed enhancement arises from the clustering of nanoparticles. They also concluded that the effective medium theories are able to predict the thermal conductivity of well-dispersed nanofluids and for the effect of aggregation, one should follow the modified effective medium models, e.g. the model proposed by Prasher et al. (2006). The paper was soon followed by a two-page comment by Murshed (2008) who stated that the enhancement is not due to aggregation of nanoparticles by referring to experimental data that show that the thermal conductivity enhances by improving the dispersion of nanoparticles.

Some experimental studies were performed to illustrate the effect of clustering since a group of researchers believed that the reason for observed anomalous enhancement in some experiments is clustering and enhancement does not occur in well-dispersed nanofluids. These works tried to control the clustering of nanoparticles and use such experimental tools that do not change the dispersion of nanoparticles. Putnam et al. (2006) used a micron-scale beam deflection technique for determining the thermal conductivity of well-dispersed 4 nm Au-MUD-ethanol and 2 nm Au-C_{12}-toluene nanofluids. They tested nanofluids with up to 0.35% volume fraction and just observed a maximum enhancement of around 1.3%. Gharagozloo et al. (2008 and 2010) investigated the effects of aggregation and diffusion on the thermal conductivity of Al_2O_3-water nanofluids with three volume fractions of 1%, 3% and 5% by using the cross-sectional infrared microscopy technique. They observed a continuous increase of the thermal conductivity over time for colloids of 3% and 5% volume fractions and no change for the 1% volume fraction colloid (see Figure 3.5). This phenomenon suggested that the aggregation of nanoparticles at higher volume fractions which increases over time is the reason behind the time-dependent increase in thermal conductivity enhancement. Gao et al. (2009) took a deeper look at the clustering and the Brownian motion effects on the thermal conductivity of nanofluids. They tested Al_2O_3 nanoparticles suspended in two different base fluids, hog fat and hexadecane. Firstly, they observed a thermal conductivity enhancement behavior close to the predictions of the effective medium theories and the change with temperature was not considerable (Figure 3.6 (a)). They observed a slight increase in thermal conductivity of the hog fat-based nanofluid upon changing phase from solid to liquid, whereas the thermal conductivity of the hexadecane-based nanofluid decreased with the phase changing from solid to liquid (Figure 3.6 (b)). In order to determine what had caused the trends for the two different nanofluids, they obtained TEM images before and after freezing (Figure 3.6 (c)). They noticed that the aggregation of nanoparticles in the hog fat-based nanofluid does not change with the phase of nanofluid, and hence the thermal conductivity is roughly identical in both phases. In contrast, the nanoparticles agglomerated in the hexadecane crystalline after freezing. After melting the frozen hexadecane-base nanofluid, they observed that the formed network-like clusters broken into short clusters, which was in agreement with the observed phenomenon that the thermal conductivity of molten sample is identical to the one before freezing.

Buongiorno et al. (2009) reported a benchmark study on the thermal conductivity of nanofluids by conducting measurements on identical nanofluids by using different measurement techniques. Thirty organizations worldwide were involved in the study. For all types of nanofluids studied, the results were in good agreement regardless of the measuring tools. The conclusion was that the thermal conductivity of well-dispersed nanofluids is predicted accurately by the model of Maxwell (1881) or the generalized model of Nan et al. (1997). The study also revealed that the thermal conductivities of the nanofluids increase with concentration and aspect-ratio of nanoparticles and decrease with the thermal conductivity of the base fluid.

Predictive MD simulation method was frequently utilized to prove or disprove the suggested underlying mechanisms that govern thermal transport in nanofluids. MD was utilized for the first time in the paper by Keblinski et al. (2002) that was discussed earlier in this chapter. Xue et al. (2004) utilized MD simulation for the solid/liquid containing simple Lennard-Jones (LJ) molecules and showed that the liquid layering on the solid is not significant and the ordering of the liquid molecules at the interface is not significant. Even if the ordering structure of the liquid molecules at the interface is identical to the crystalline structure of the solid molecules, the thickness of the layer is so small that it will not cause a significant thermal conductivity enhancement. In this investigation, the important LJ parameter, ε, for the solid-solid interactions was chosen as 10 times the one for liquid-liquid interactions and the Lorentz-Berthelot mixing rule (Allen and Tildesley, 1987) was used to calculate solid-liquid interaction. Evans et al. (2006) utilized the direct non-equilibrium MD (NEMD) to conduct a parametric study of the thermal conductivity enhancement of eight suspended nanoparticles in a liquid. The LJ potential was used between all molecules. In this study, $\varepsilon_{ss} = \varepsilon_{ll}$, the maximum value for ε_{sl} was equal to $2.25\varepsilon_{ll}$ and an attractive finite extensible nonlinear elastic (FENE) force field (Kremer and Grest, 1990) was used to keep the atoms making up the nanoparticles together. They used three different values for ε_{sl} and observed thermal conductivity enhancements comparable to predictions of the theoretical models. They concluded that the MD-based calculation of thermal conductivity enhancement for well-dispersed nanofluids proves the correctness of predictions of the effective medium theory and therefore the Brownian motion does not play any role in enhancement. Eapen et al. (2007) utilized the same strategy in terms of potentials between molecules but with stronger solid-liquid interactions from two to seven times the interaction between liquid-liquid molecules. They studied ten uniformly-dispersed clusters, each containing ten atoms, distributed within 1948 liquid atoms. They used the NEMD Muller-Plathe method (1997) and concluded that a cluster network of nanoparticles mediated by interfacial liquid atoms can be the reason for the observed deviation from the theoretical models. Same authors published another paper on the mechanism of thermal conductivity enhancement by using the Green-Kubo relation and MD simulations (2007). They took the LJ potential of a Xe-Pt nanofluid in their MD simulations. They tried to provide a physical reasoning on the observed behavior of different components of the heat flux autocorrelation function (HFACF) which is calculated in the MD simulations and used in the Green-Kubo relation, as will be explained in the methodology section. They concluded that the thermal conductivity enhancement is due to the strong solid-liquid interaction which shows up in the potential component in HFACF. Sarkar et al. (2007) performed MD simulations and utilized the Green-Kubo relation to study the thermal conductivity of a model Ar-Cu nanofluid. Their system included a single particle in the simulation box and by changing the radius of the nanoparticle, they varied the volume fraction. They speculated that the predicted marked enhancements in thermal conductivity are due to the Brownian motion-induced convection in nanofluids. Kang et al. (2011) took the same configuration, the same nanofluid and the same Green-Kubo method but utilized the embedded atom method (EAM) potential (Daw and Baskes, 1984) for Cu atoms instead of the LJ potential used in Sarkar et al. (2007). Interestingly, their results were of the order of the prediction based on the Maxwell model.

Finally, a schematic diagram of the different mechanisms of heat transfer in nanofluids is given in Figure 3.7. As explained in the text, clustering and the Brownian motion are believed to have higher impacts on thermal conductivity enhancement in nanofluids in comparison to the other mechanisms.

3.3 Effective medium theory

Prediction of the effective transport properties, such as thermal conductivity and electrical conductivity of binary mixtures/composites, has been of great interest (Batchelor, 1974). The essential assumption of the developed models is that such heterogeneous media (mixtures/composites) consist of a continuous base material (matrix) and a discrete phase (filler) dispersed in it (Progelhof et al., 1976). The effective thermal conductivity of a binary mixture/composite system depends on the thermal conductivity of constituents, the concentration, dimension, shape and distribution of the dispersed fillers, and the interfacial thermal conductance between the fillers and the matrix as well. Considering the assumption of random distribution of fillers, microscale properties of the mixtures/composites, i.e., dimension, shape and distribution of the fillers, have often been ruled out of the theoretical framework. Therefore, the effective thermal conductivity of mixtures/composites has mostly been correlated with the thermal conductivities of the matrix and the fillers and the concentration (volume fraction) of fillers.

The simplest effective medium theory formula was proposed by Maxwell (1881) for magnetic permeability of dilute stationary spherical composites. A similar approach is applicable for the thermal conductivity of dilute dispersions of stationary spherical particles (Hashin and

Shtrikman, 1962, and Hamilton and Crosser, 1962). The equation for the effective thermal conductivity, k_{eff}, due to Maxwell (1881) reads as follows

$$k_{eff} = k_m \frac{k_p + 2k_m + 2\phi(k_p - k_m)}{k_p + 2k_m - \phi(k_p - k_m)} \tag{3.1}$$

where k_m and k_p are the thermal conductivity values of the matrix and particle, respectively. Quantity ϕ stands for the volume fraction of the inclusions. The size of the spherical particles did not appear in the original theory, however many researchers have extended this relation to the case of inclusions in the nanometer size range. In effect, the improved thermal conductivity of nanofluids in comparison to the Maxwell's relation was deemed to be anomalous and attributed to the "superior" behavior of nanoparticle suspensions. Regardless of the size of the suspended spherical particles, the limitations of this equation are: (i) presence of dilute non-interacting particles and (ii) infinite value of the interfacial thermal conductance at the interface of the particle and the matrix.

For any geometrical shape of the particles, the effective thermal conductivity will assume a value within the range of limits coined the Hashin and Shtrikban (1962) (H-S) bounds. These correspond to the bounds derived by the Maxwell equation (Eq. 3.1) for the limiting cases of (i) the particles being the dispersed medium and fluid being the continuous medium or (ii) fluid being the dispersed medium and the particles being the continuous medium,

$$k_m\left(1+\frac{3\phi(k_p-k_m)}{3k_m+(1-\phi)(k_p-k_m)}\right) \le k_{eff} \le k_p\left(1-\frac{3(1-\phi)(k_p-k_m)}{3k_p-\phi(k_p-k_m)}\right) \tag{3.2}$$

This non-equality holds for $k_p > k_m$. For $k_p < k_m$, the upper and lower bounds get reversed. The schematic diagrams for the configuration of particles associated with the limiting H-S bounds (i.e. Eq. 3.2) are shown in Figure 3.8. The H-S bounds are within the thermal conductivity values associated with the series and parallel configurations, i.e. $1/k_{eff} = (1-\phi)/k_m + \phi/k_p$ and $k_{eff} = (1-\phi)k_m + \phi k_p$, respectively. The idealized series and parallel configurations are schematically shown in Figure 3.9. To illustrate the differences between the mentioned predictive models, the plots for thermal conductivity ratio of the effective thermal conductivity and base fluid (k_{eff}/k_m) with respect to the volume fraction and k_p/k_m are shown in Figures 3.10 (a) and (b), respectively. In Figure 3.10 (a), for a nanofluid case with k_p/k_m=100, the predicted thermal conductivity ratios for different models are plotted against the volume fraction of nanoparticles. It shows that for all volume fractions, the H-S bounds stay within the predicted curves by using the series and parallel models. In Figure 3.10 (b), for a typical nanofluid with ϕ =0.01, the predicted curves for k_{eff}/k_m from different models are plotted against k_p/k_m. It also indicates that for all k_p/k_m, the predictions of H-S bounds lie between the series and parallel configurations. Moreover, for the H-S lower bound and the series model, k_{eff}/k_m does not change with the value of k_p/k_m and it is approximately 1 for all k_p/k_m, whereas for predictions from the H-S upper bound and the parallel model, in which strong connected networks of nanoparticles are assumed, k_{eff}/k_m depends highly on the value of k_p/k_m.

For heterogeneous non-dilute two-component systems in which the two components are distributed randomly, with neither phase being necessarily continuous or dispersed, the effective medium theory gives the following equation for the effective thermal conductivity (Landauer, 1952)

$$(1-\phi)(k_m - k_{eff})/(k_m + 2k_{eff}) + \phi(k_p - k_{eff})/(k_p + 2k_{eff}) = 0 \tag{3.3}$$

Hasselman and Johnson (1987) introduced the effect of the interfacial thermal conductance into the Maxwell's effective medium equation and derived the following relation

$$k_{eff} = k_m \frac{k_p(1+2\alpha) + 2k_m + 2\phi[k_p(1-\alpha) - k_m]}{k_p(1+2\alpha) + 2k_m - \phi[k_p(1-\alpha) - k_m]} \tag{3.4}$$

in which the quantity α accounts for the effect of the interfacial resistance and is equal to Rk_m / r_p with R and r_p being the Kapitza thermal resistance and particle radius, respectively. For very small volume fractions of the dispersed particles, Eq. (3.4) reduces to

$$\frac{k_{eff}}{k_m} = 1 + 3\phi \frac{k_p(1-\alpha) - k_m}{k_p(1+2\alpha) + 2k_m} \tag{3.5}$$

Another simplified form of Eq. (3.4) is for the high-conductivity particles satisfying the limit $k_p >> k_m$

$$\frac{k_{eff}}{k_m} = \frac{1 + 2\phi(1-\alpha)/(1+2\alpha)}{1 - \phi(1-\alpha)/(1+2\alpha)} \tag{3.6}$$

The most simplified form will be for the dispersions satisfying the two limits of very small volume fractions and high-conductivity dispersed particles

$$\frac{k_{eff}}{k_m} = 1 + 3\phi \tag{3.7}$$

The above equations are only appropriate for spherical inclusions. Nan et al. (1997) derived the formulas for suspensions of spheroid particles (ellipsoids having equal diameters along two axes). The elements of the effective thermal conductivity tensor are the following equations

$$k_{eff,11} = k_{eff,22} = k_m \frac{2+\phi[\beta_{11}(1-L_{11})(1+\langle\cos^2\theta\rangle)+\beta_{33}(1-L_{33})(1-\langle\cos^2\theta\rangle)]}{2-\phi[\beta_{11}L_{11}(1+\langle\cos^2\theta\rangle)+\beta_{33}L_{33}(1-\langle\cos^2\theta\rangle)]} \tag{3.8a}$$

$$k_{eff,33} = k_m \frac{1+\phi[\beta_{11}(1-L_{11})(1-\langle\cos^2\theta\rangle)+\beta_{33}(1-L_{33})\langle\cos^2\theta\rangle]}{1-\phi[\beta_{11}L_{11}(1-\langle\cos^2\theta\rangle)+\beta_{33}L_{33}\langle\cos^2\theta\rangle]} \tag{3.8b}$$

with

$$\beta_{ii} = \frac{k_{ii}^c - k_m}{k_m + L_{ii}(k_{ii}^c - k_m)}, \quad i = 1,2,3 \tag{3.9}$$

and

$$\langle\cos^2\theta\rangle = \frac{\int \rho(\theta)\cos^2\theta\sin\theta d\theta}{\int \rho(\theta)\sin\theta d\theta} \tag{3.10}$$

where θ is the angle between the symmetry axis x_3' of the ellipsoidal particle and the axis x_3, whereas $\rho(\theta)$ is the distribution function for this angle. Quantity k_{ii}^c is the *i*-th element of the equivalent thermal conductivity tensor of the particle and its surrounding interfacial layer. By assuming a thin poorly-conducting interface region, it follows that

$$k_{ii}^c = \frac{k_p}{1+\gamma L_{ii} k_p / k_m} \tag{3.11}$$

with

$$\gamma = \begin{cases} (2+1/p)\alpha, & \text{for } p \ge 1 \\ (1+2p)\alpha, & \text{for } p \le 1 \end{cases} \tag{3.12}$$

in which p is the aspect-ratio of the ellipsoid. It is defined as a_3/a_1 where a_1 and a_3 are ellipsoid's diameters in the x_1' and x_3' directions, respectively with $a_2 = a_1$. Here, α is equal to Rk_m/a_1. Quantities L_{ii} are geometrical parameters and are defined as given in the following equations

$$L_{11} = L_{22} = \begin{cases} \dfrac{p^2}{2(p^2-1)} - \dfrac{p}{2(p^2-1)^{3/2}} \cosh^{-1} p, & \text{for } p > 1 \\ \dfrac{p^2}{2(p^2-1)} + \dfrac{p}{2(1-p^2)^{3/2}} \cos^{-1} p, & \text{for } p < 1 \end{cases}$$

(3.13)

$$L_{33} = 1 - 2L_{11} \tag{3.14}$$

Considering sphere-shaped fillers by taking p=1, $L_{33} = L_{11} = 1/3$ and $\langle \cos^2 \theta \rangle = 1/3$, the Nan's model reduces to the effective medium equation derived by Hasselman and Johnson (1987) (Eq. 3.4).

Using the Bruggeman (1935) model, the effective medium theory has been derived for high volume fraction composites. This has been done by taking into account a differential form of (Eq. 3.5), i.e. obtaining the differential of the effective thermal conductivity by adding particles incrementally. The resulting equation is as follows

$$\frac{dk_{eff}}{k_{eff}} = 3\frac{d\phi}{(1-\phi)}\frac{k_p(1-\alpha)-k_{eff}}{k_p(1+2\alpha)+2k_{eff}} \qquad (3.15)$$

Integrating the above equation for the limits $k_{eff} : k_m \rightarrow k_{eff}$ and $\phi : 0 \rightarrow \phi$ leads to the following expression for the effective thermal conductivity

$$(1-\phi)^3 = \left[\frac{k_m}{k_{eff}}\right]^{(1+2\alpha)/(1-\alpha)} \left[\frac{k_{eff} - k_p(1-\alpha)}{k_m - k_p(1-\alpha)}\right]^{3/(1-\alpha)} \qquad (3.16)$$

However, in order to predict the effective thermal conductivity of particulate composites accurately, the distribution of particles is required (Torquato, 1985).

It has been also shown (Prasher et al., 2006) that the classical effective medium theories can predict the effective thermal conductivity even when the nanoparticles aggregate and form network of percolated configurations. In such cases, the effective thermal conductivity is calculated in two steps. First, the thermal conductivity of the aggregate (k_a) is predicted by solving the equation for the effective thermal conductivity (Eq. 3.3)

$$(1-\phi_{\text{int}})(k_m-k_a)/(k_m+2k_a)+\phi_{\text{int}}(k_p-k_a)/(k_p+2k_a)=0 \qquad (3.17)$$

in which ϕ_{int} is the volume fraction of particles within the aggregates and is related to the overall volume fraction by $\phi = \phi_{\text{int}}\phi_a$, where ϕ_a is the volume fraction of the aggregates. Then, the overall effective thermal conductivity is obtained by using the Maxwell's model (Eq. (3.1))

$$k_{eff} = k_m \frac{k_a + 2k_m + 2\phi_a (k_a - k_m)}{k_a + 2k_m - \phi_a (k_a - k_m)} \tag{3.18}$$

In summarizing this section, different predictive theoretical models have been proposed for calculating the thermal conductivity of particle-fluid suspensions which range from the simple dilute well-dispersed spherical particle suspensions with no thermal boundary resistance to the complex non-dilute clustered non-spherical particle suspensions with boundary resistance. As explained in the literature review (section 3.2), some researchers have pointed to the Brownian motion-induced micro-convection as a new mechanism for thermal conductivity enhancement in well-dispersed nanofluids. Consequently, they have suggested new models to account for the Brownian motion of particles. In the following sections, comparison of the MD results with the predictions of the Maxwell's model for well-dispersed nanofluids will be presented, which shows that the MD results are well consistent with the Maxwell's model predictions and no extra enhancement is observed.

Moreover, based on our results presented in chapter 5, for suspensions containing high aspect-ratio particles and base fluids of long molecular chains, the particle-induced ordering effect on base fluid molecules is another improving parameter in thermal transport which has not been addressed in any of mentioned models.

3.4 Simulation Methodology

Thermal conductivity can be determined from EMD simulations via the Green-Kubo relationship:

$$k_{ij} = \frac{1}{Vk_B T^2}\int_0^\infty < J_i(t)J_i(0) > dt, \quad i = x, y \text{ or } z. \tag{3.19}$$

In Eq. 3.19, k_{ij} is the *ij*-th component of the thermal conductivity tensor at temperature *T*. Quantity *V* is the volume of the simulation cell and k_B is the Boltzmann constant. The time-integral is over the heat current autocorrelation function (HCACF) that is obtained from EMD simulations and the symbol < > indicates ensemble averaging. The molecular-scale expression for the heat current, **J**(*t*), for a two-component system is given by;

$$\mathbf{J}(t) = \overbrace{\left[\sum_{j=1}^{N}\mathbf{v}_j E_j - \sum_{\alpha=1}^{2} h_\alpha \sum_{j=1}^{N_\alpha}\mathbf{v}_{\alpha j}\right]}^{\mathit{Convective}} + \overbrace{\left[\frac{1}{2}\sum_{i=1}^{N}\sum_{j=1,\, j\neq i}^{N}\mathbf{r}_{ij}\left(\mathbf{v}_j.\mathbf{F}_{ij}\right)\right]}^{\mathit{Virial}}, \tag{3.20}$$

where $\mathbf{v}_j$ and E_j are the velocity and energy (sum of the potential and kinetic energies) of particle *j*, respectively. Quantities $\mathbf{r}_{ij}$ and $\mathbf{F}_{ij}$ are the displacement vector and the force between particles *i* and *j*, respectively. Quantity *N* is the total number of particles and N_α is the number of particles for species α, whereas h_α denotes the average partial enthalpy of species α. In Eq. 3.20, the first group of terms represents the convective current and the second group is identified as the heat current due to the particle-particle interactions. Subtracting of the correct average enthalpy term is extremely important since such quantity just moves silently with diffusing particles, but the associated energy is not exchanged and does not contribute to heat conduction. Interestingly, when a single-component system is simulated in equilibrium and at overall zero total momentum, the average enthalpy subtraction is irrelevant as the sum of the velocities is equal to zero ($\sum_{j=1}^{N_\alpha} \mathbf{v}_{\alpha j} = 0$).

For each of the species, the average enthalpy is defined as:

$$h_\alpha = \frac{\sum_{i=1}^{N_\alpha} \left[K_i + U_i + \frac{1}{3}\left(m_i v_i^2 + \frac{1}{2}\sum_{j=1}^{N} \mathbf{r}_{ij} . \mathbf{F}_{ij} \right) \right]}{N_\alpha} , \tag{3.21}$$

where K_i and U_i are the time-averaged kinetic and potential energies of particles of species α, respectively. The first two terms are the kinetic (K_i) and potential (U_i) energies that constitute the internal energy (E_i) and the third term is the PV term, which includes both kinetic and interaction (virial) terms. In chapter 2 of this dissertation, extensive validation of the partial enthalpy formula is provided by determining the thermal conductivity of various two-component systems, including gas, liquid and solid mixtures.

3.5 Analysis Methodology

As presented in Eq. (3.20), the heat flux can be divided into two main components: convective and virial (interaction) terms. Correspondingly, HCACF will have four terms resulting from multiplying each one of these two terms by the other. Therefore, we formally decompose the expression for the HCACF into four terms:

$$HCACF = < CC > + < CV > + < VC > + < VV > . \tag{3.22}$$

In Eq. (3.22), for example, <*CC*> stands for the autocorrelation function of the convective heat current and <*CV*> is the cross-correlation function of the convective and virial currents.

For further analysis, the convective term is decomposed into the energy and average enthalpy terms as follows:

$$C = \frac{1}{V}\left[\sum_{j=1}^{N} \mathbf{v}_j E_j - \sum_{\alpha=1}^{2} h_\alpha \sum_{j=1}^{N_\alpha} \mathbf{v}_{\alpha j}\right] = E - H. \qquad (3.23)$$

The associated terms in the HCACF are *EE*, *HH*, *EH* and *HE*. For the average energy or average enthalpy, the autocorrelation function is determined by the autocorrelation function of the average velocity, i.e.:

$$\mathbf{v}(t) = \frac{1}{N}\sum_{j=1}^{N} \mathbf{v}_j \ . \qquad (3.24)$$

The velocity autocorrelation function has the dimension of the mass diffusion coefficient and can be defined as the diffusion constant:

$$D = \int_0^\infty < v_i(t) v_i(0) > dt, \quad i = x, y \text{ or } z. \qquad (3.25)$$

The above-described characterizing methodology will be used to analyze the results of the EMD simulations in relation to the dominance of the various contributions to the thermal conductivity.

3.6 Model

The nanofluid system was formed by carving a sphere within methane atoms and placing copper atoms on an FCC (face-centered cubic) crystal sites with a lattice constant of 3.61 Å. The Lennard-Jones (LJ) potential was chosen for intermolecular interactions among all pairs of particles. The LJ parameters (σ and ε) for copper atoms are 2.34 Å and 9.4512 kcal/mol, respectively (Halicioglu and Pound, 1975). For methane molecules, the Optimized Potentials for

Liquid Simulations (OPLS) united-atom force field was used (Jorgensen et al., 1984). In this force field, CH_4 is taken as a single interaction site for LJ interactions. The LJ parameters (σ and ε) for methane united atoms are 3.73 Å and 0.294 kcal/mol, respectively. The Lorentz-Berthelot mixing rule (Allen and Tildesley, 1989) was used for determining the LJ parameters between the methane pseudo atoms and copper atoms.

Simulations were carried out on systems with two different temperatures of 100 K and 110 K and two different copper particle diameters of 12.703 Å and 25.406 Å. For the cases of T=110 K and d=12.703 Å, a nanoparticle containing 87 copper atoms was suspended in different number of methane molecules leading to five different volume percentages of 0.15% (10957 methane molecules), 0.23% (6893 methane molecules), 0.35% (4612 methane molecules), 0.47% (3410 methane molecules) and 0.66% (2438 methane molecules). For the cases of T=100 K and d=12.703 Å, a nanoparticle containing 87 copper atoms was suspended in different number of methane molecules giving rise to three corresponding volume percentages of 0.36% (4612 methane molecules), 0.49% (3410 methane molecules) and 0.69% (2438 methane molecules). For the cases of T=110 K and d=25.406 Å, a nanoparticle containing 683 copper atoms was suspended in different number of methane molecules leading to three different volume percentages of 0.55% (23187 methane molecules), 0.86% (14754 methane molecules) and 1.06% (12054 methane molecules). As an example, the snapshot of one of the studied nanofluid systems is shown in Figure 2.3 (in chapter 2).

The velocity Verlet algorithm was used to integrate the Newton's equation of motion numerically with a time step of 1 fs. Systems were initially equilibrated for 200,000 time steps under isothermal-isobaric ensemble (NPT) with T= 100 K or 110 K (depending on the case) and atmospheric pressure and further equilibrated under constant volume and energy condition

(NVE) for 200,000 time steps. Finally, the process was followed with 1,000,000 time steps under the NVE condition and the fluctuating heat current was monitored every 5 fs. For each case, the HCACF curves were obtained by averaging over 8 different simulations having different initial velocity distributions. All simulations were performed with the large-scale atomic/molecular massively parallel simulator (LAMMPS) molecular dynamics package (Plimpton, 1995).

3.7 Results

For the pure base material case at T=110 K and the nanofluid case with d=12.703 Å nanoparticle at 0.35% volume percentage and T=110 K, the HCACF curves and the associated components defined in Eq. 3.22 are shown in Figures 3.11 and 3.12, respectively. The *VC* terms which are equal to the *CV* terms due to time reversal symmetry are not shown. For each case, the HCACF curves for eight different initial velocity distributions which are identified with eight different SEEDs in the figures are shown. The average curves are also presented in the figures which are the curves utilized in thermal conductivity analysis. For both pure and nanofluid cases, the HCACF curves for the total and *CC*, *VV* and *CV* components decay to zero within 1 ps which is a typical convergence time for liquids as explained in chapter 2. Moreover, for both cases, the *VV* component has the highest value at t=0 among all components of the HCACF and is the dominant component in HCACF. The *VV* curves for both pure and nanofluid cases are fairly smooth, while the *CC* and *CV* curves for the nanofluid contain oscillations believed to be corresponding to convection in methane induced by the Brownian motion of the nanoparticle.

For the pure and nanofluid cases mentioned above, the time-dependent curves for the total thermal conductivity and the components of thermal conductivity, which are obtained from the time-integral of the HCACF curves as given in Eq. 3.19, are shown in Figures 3.13 and 3.14, respectively. As shown in the figures, in both cases, the curves converge to the final value within 1 ps. For both cases, the dominant component is the thermal conductivity associated with the *VV* term. For the nanofluid case, the curves contain more oscillations with respect to the curves for the pure case.

In Figure 3.15, the variation of the MD-predicted values of the ratio of the thermal conductivity of nanofluid and the thermal conductivity of base fluid (k/k_f) as a function of the particle volume percentage is shown for two temperatures of 100 K and 110 K and two particle diameters of 12.703 Å and 25.406 Å. The EMD-predicted values for all cases are close to the Maxwell model for prediction of the thermal conductivity of well-dispersed suspensions of spherical particles.

To gain further insight into a potential role of the convective term for the nanofluid cases, the contributions of the *CC*, *VV*, and *CV* (which due to time reversal symmetry is equal to *VC*) terms are also shown in Figure 3.16. In all cases, by far, the major term in the thermal conductivity of the nanofluid is the virial contribution (*k_vv*). The predicted values for this term do not vary with the volume percentage. The remaining three terms involving convection, including the cross terms (*k_cv* and *k_vc*) and the *k_cc* term are small by comparison to the *k_vv* term. The *k_cc* term, which is directly associated with the Brownian motion-related micro-convection, increases slightly with the volume percentage, but is much smaller than the virial term. These results clearly demonstrate that the thermal conductivity of a nanofluid is dominated by the atom-atom interaction mechanism rather than the diffusion/micro-convection terms.

In Figure 3.17, the contributions to the thermal conductivity due to the *EE* and *HH* terms for the case of 12.703 Å nanoparticle at 0.35% volume percentage and 110 K are shown. These cancelling contributions that have been overlooked by some previous studies are more than one order of magnitude greater than the total conductivity value. However, as shown in the bottom panel of Figure 3.17, both *EE* and *HH* terms essentially follow the behavior of the integral over time of the velocity autocorrelation function. This means that the *EE* term is dominated by the constant value of the average energy. As a consequence, the *EE*+*HH* terms essentially cancel the *HE* + *EH* terms. This result indicates that it is extremely important to subtract the correctly-defined average enthalpies in the heat current expression. Otherwise, the cancellation will not occur, leading to significant and erroneous contributions to the thermal conductivity on behalf of the Brownian motion.

In complementing the above clarifications set forth in this chapter, the self-diffusion coefficient of the nanoparticle at T=110 K with d=12.703 Å is plotted versus the volume percentage in Figure 3.18. The diffusion coefficient rises with the particle volume percentage, which is due to the increasing magnitude of the velocity of the center of mass. Correspondingly, the *EE* and *HH* terms that have resulted from multiplying the energy and velocity terms follow the same trend, i.e., strong direct dependence on the volume percentage. However, as discussed above, these terms will cancel out with the *EH* and *HE* terms and will have no significant effect on the thermal conductivity.

3.8 Summary and Conclusions

Equilibrium molecular dynamics simulations were used to determine the role of micro-convection on thermal transport in nanofluids. While individual convective terms in the heat current expression are significant, they essentially cancel each other, leading to the conclusion that micro-convection has a minor role in thermal transport of nanofluids. It was demonstrated that the critical technical issue in EMD thermal conductivity determination is the subtraction of the correct value of the average enthalpy of each species from the energy in the convective term of the heat current.

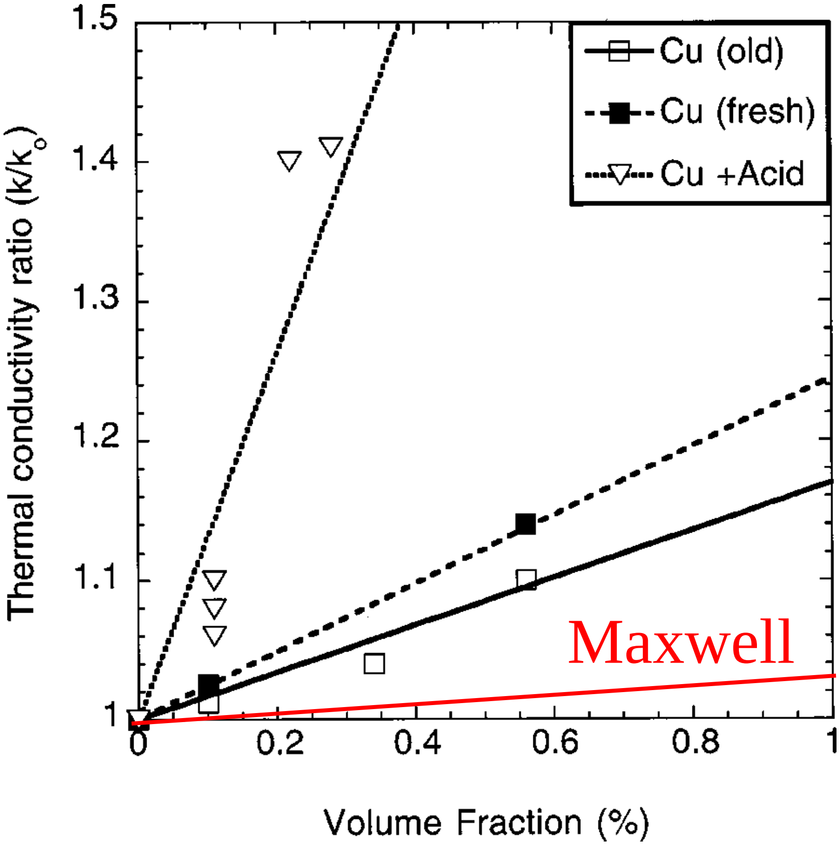

Figure 3.1 Anomalous thermal conductivity enhancement in nanofluids reported by Eastman et al. (2001) with the Maxwell model superimposed on it.

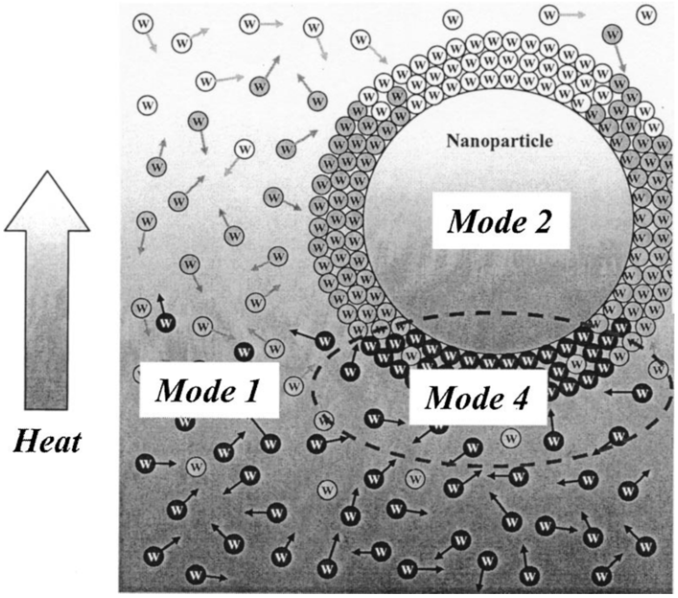

Figure 3.2 Schematic diagram proposed by Jang and Choi (2004) for the effect of the Brownian motion-induced convection on thermal transport. Mode 1: thermal transport in the base fluid due to its molecules' collisions; Mode 2: thermal transport within the nanoparticle; Mode 3 (not shown): thermal transport due to the nanoparticles' interactions; Mode 4: interfacial thermal transport between the base fluid and the nanoparticle.

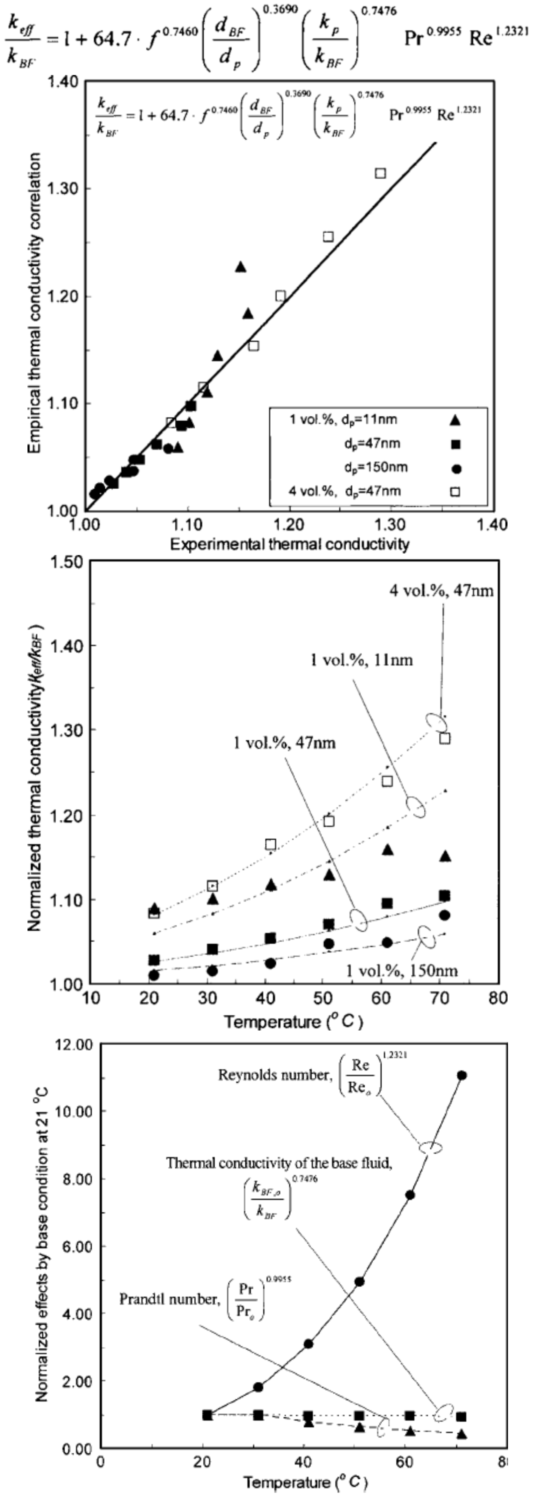

Figure 3.3 The correlation function and graphs reported by Chon et al. (2005) based on a Brownian motion-induced convection model.

$$\frac{k}{k_f} = (1 + A\mathrm{Re}^m \mathrm{Pr}^{0.333}\phi)\left[\frac{(1+2\alpha)+2\phi(1-\alpha)}{(1+2\alpha)-\phi(1-\alpha)}\right]$$

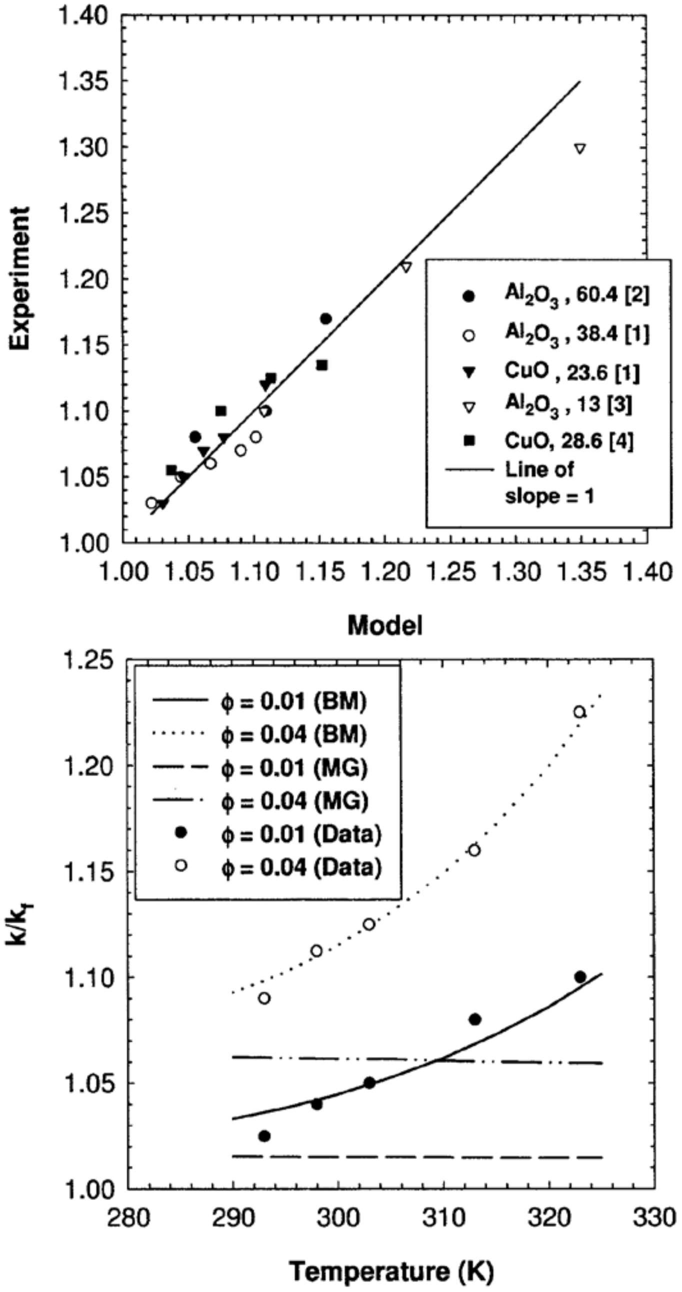

Figure 3.4 Brownian motion-induced model correlation function and graphs reported by Prasher et al. (2005 and 2006).

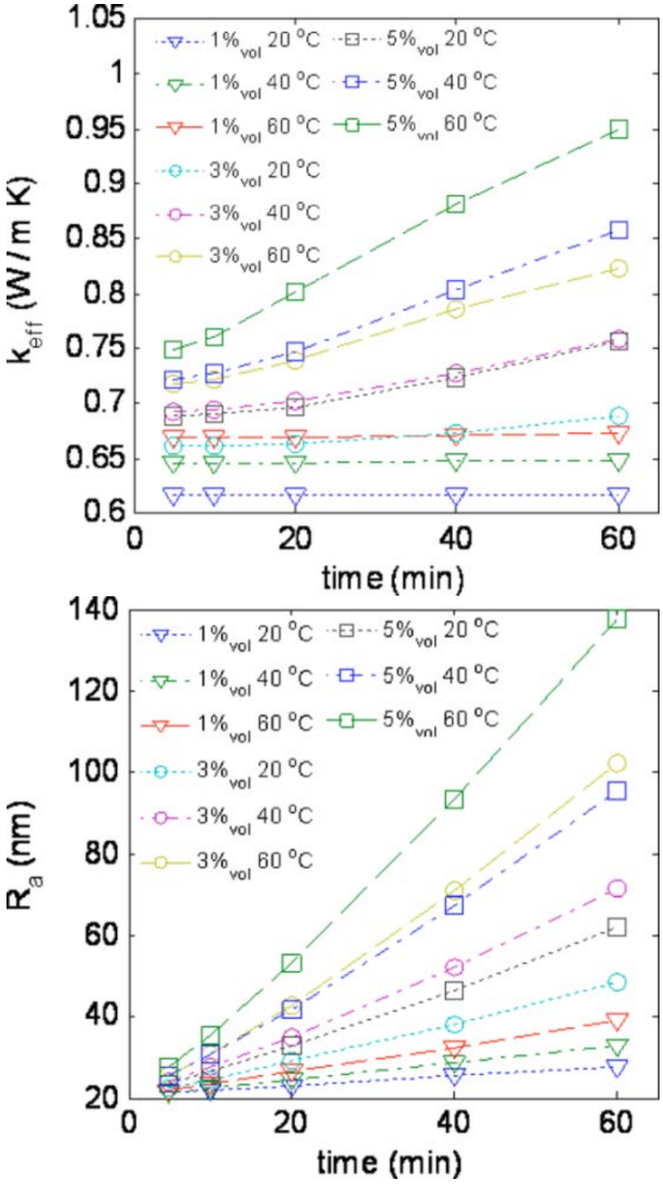

Figure 3.5 Increase of thermal conductivity with aggregation/clustering of nanoparticles over time observed for high volume fraction nanofluids by Gharagozloo et al. (2008 and 2010).

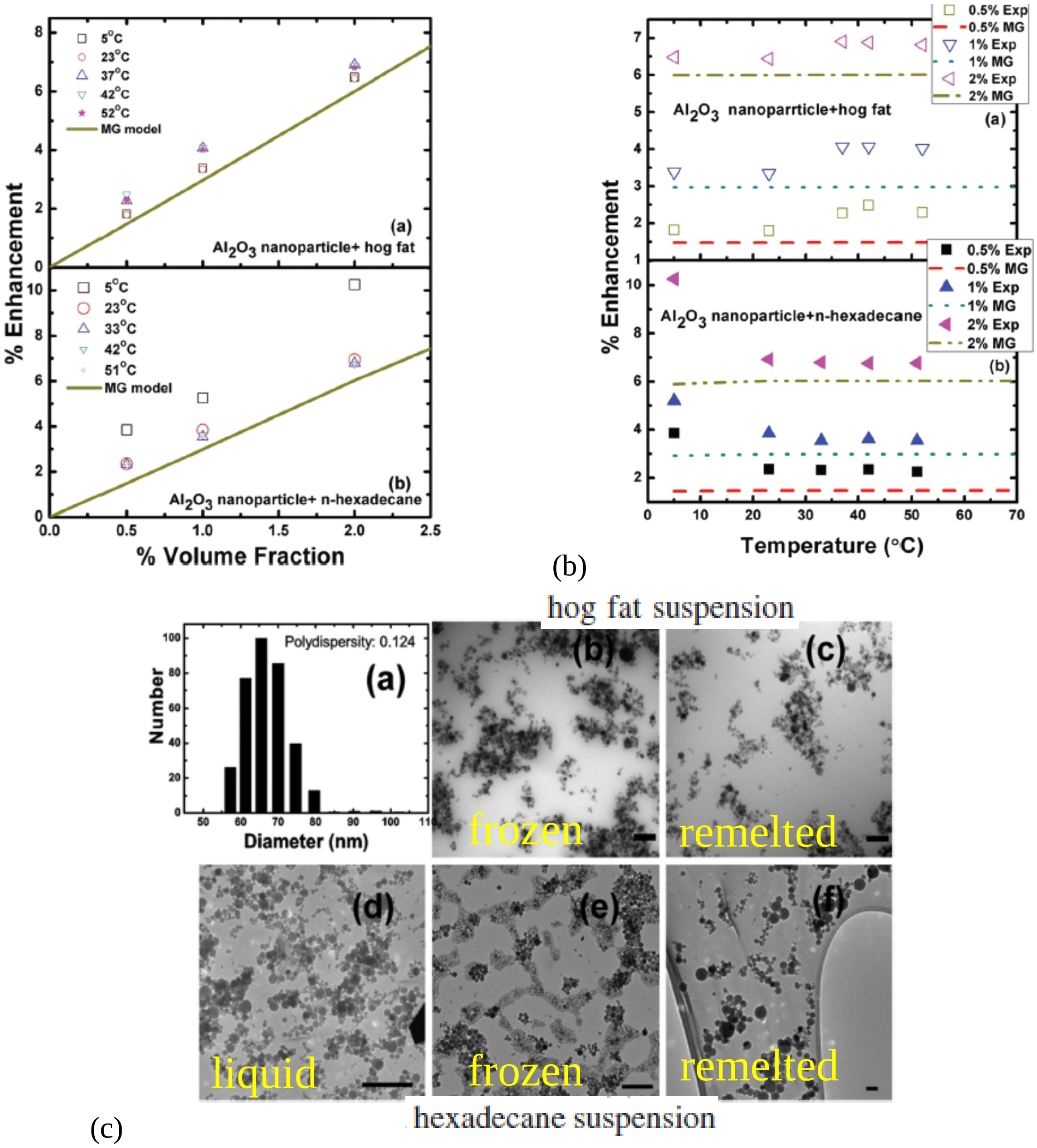

(a) (b)

(c)

Figure 3.6 Figures taken from the work by Gao et al. (2009) highlighting (a) consistency between experimental results and Maxwell's model predictions, (b) observed different behaviors of thermal conductivity change upon melting for hog fat and n-hexadecane based nanofluids and (c) TEM images of both nanofluids before melting, after freezing and after remelting.

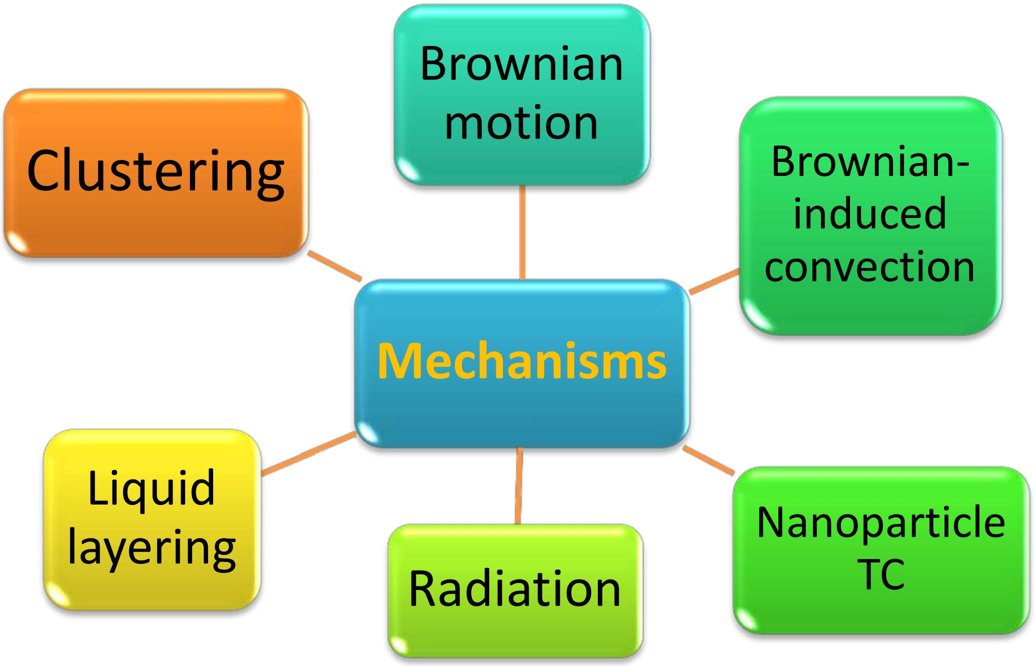

Figure 3.7 Different mechanisms presented to date that govern thermal transport in nanofluids.

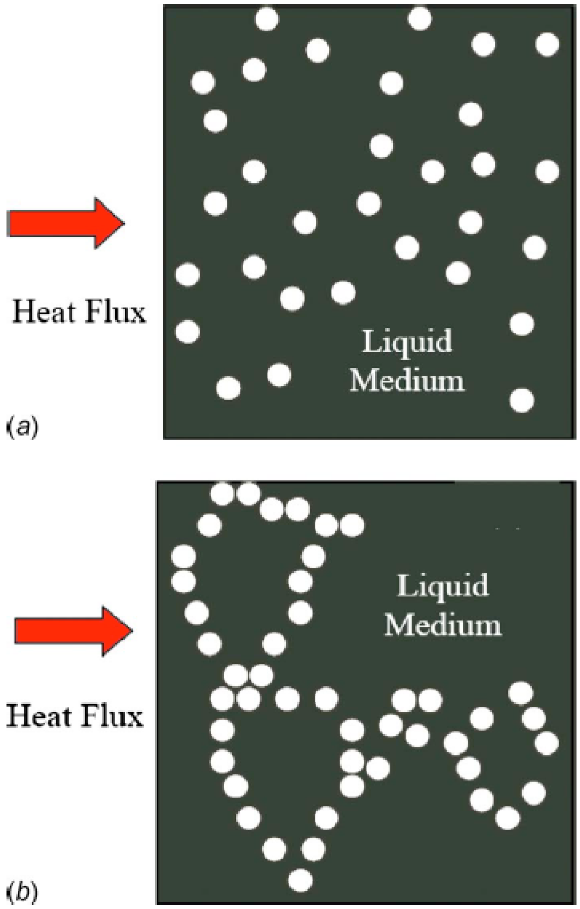

Figure 3.8 Schematic representations of (a) lower bound and (b) upper bound configurations for heat transfer in a binary nanofluid (Eapen et al., 2010).

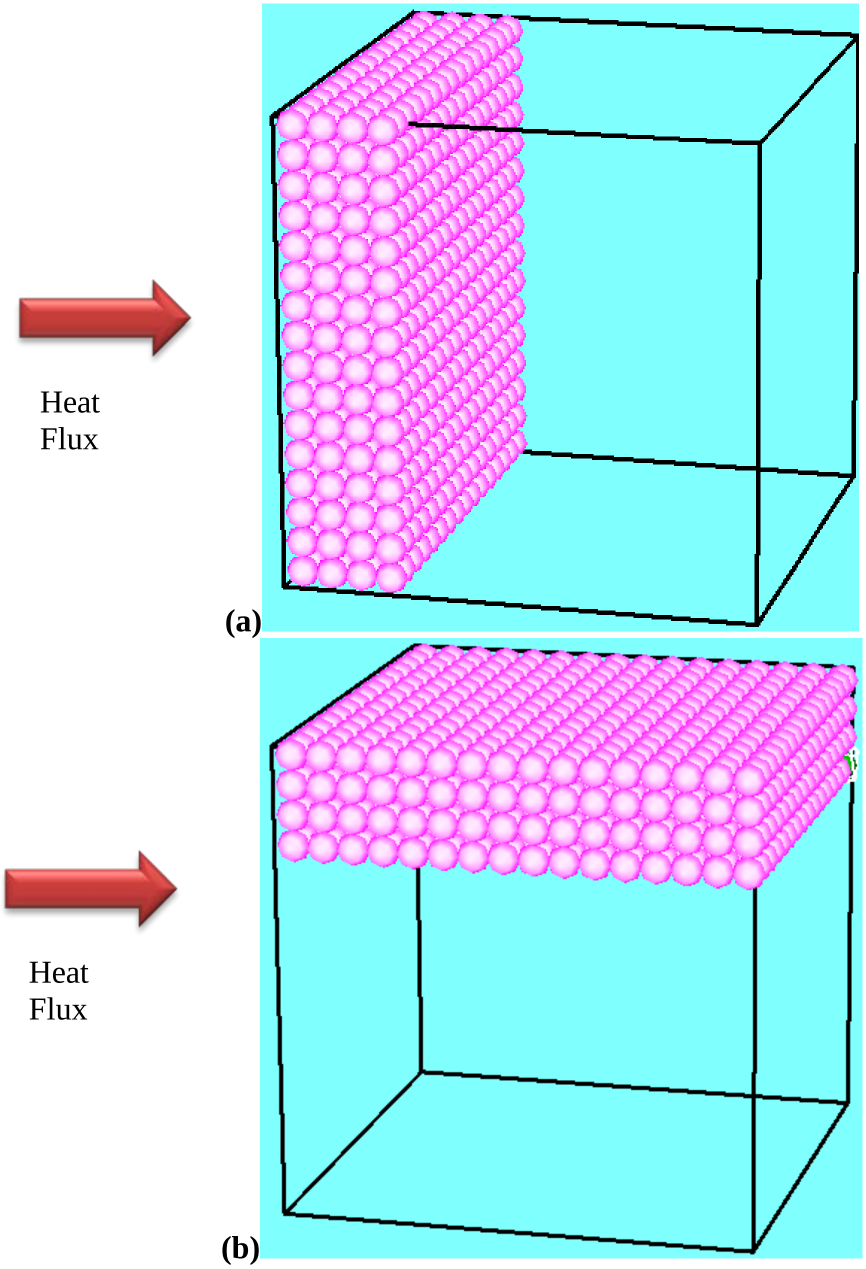

Figure 3.9 Schematic representations of idealized (a) series and (b) parallel configurations for heat transfer in a binary nanofluid.

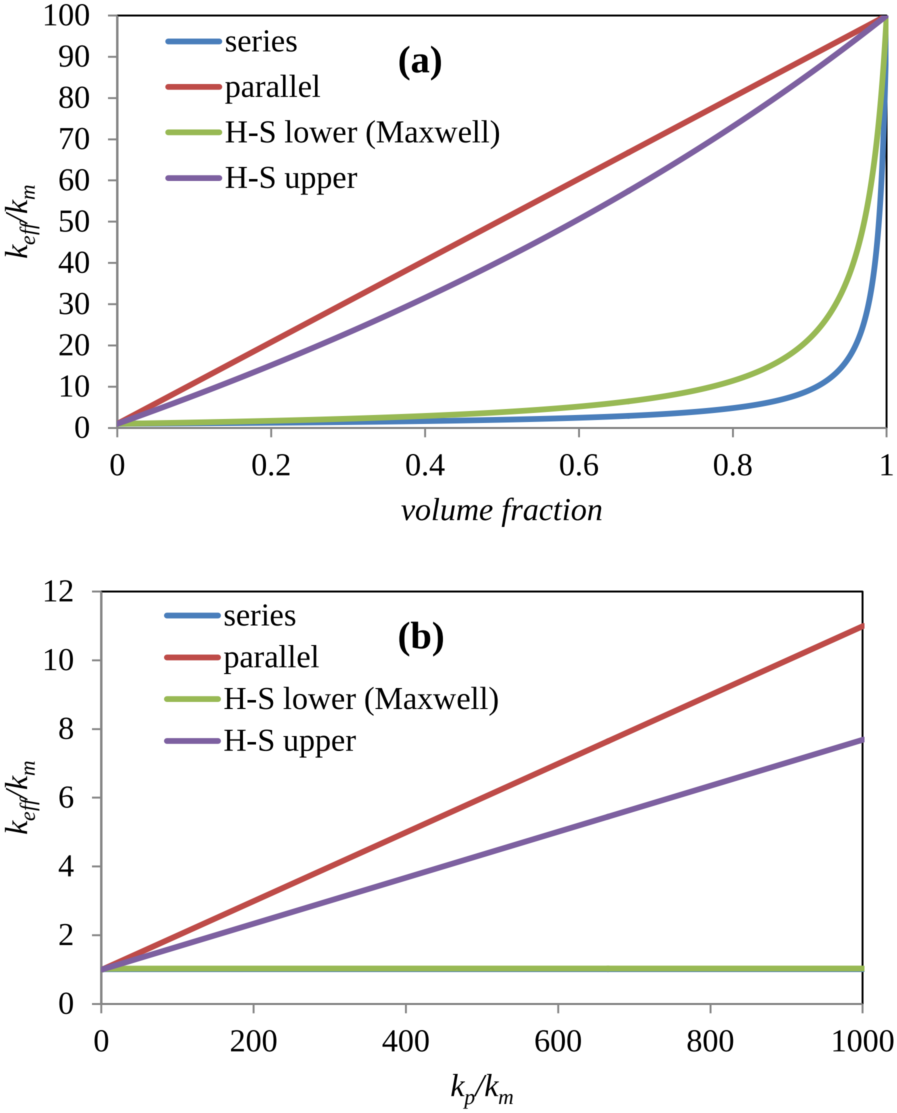

Figure 3.10 The curves for predicted ratio of effective thermal conductivity and base fluid from H-S bounds and series and parallel models versus (a) volume fraction for a typical nanofluid with k_p/k_m=100 and (b) k_p/k_m for a typical nanofluid with ϕ=0.01.

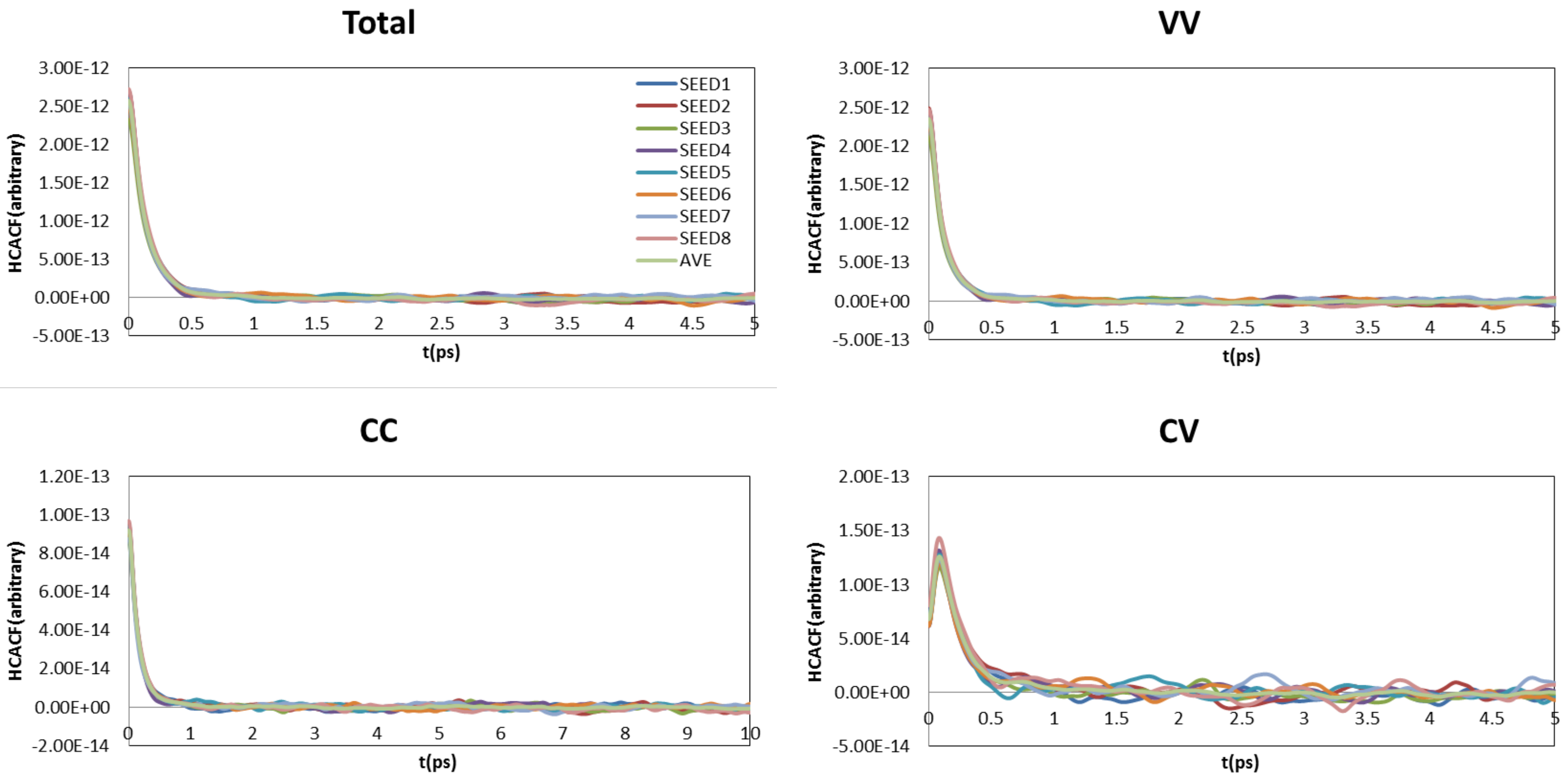

Figure 3.11 Total HCACF curve and curves for the *VV*, *CC* and *CV* components for pure methane at *T*=110 K.

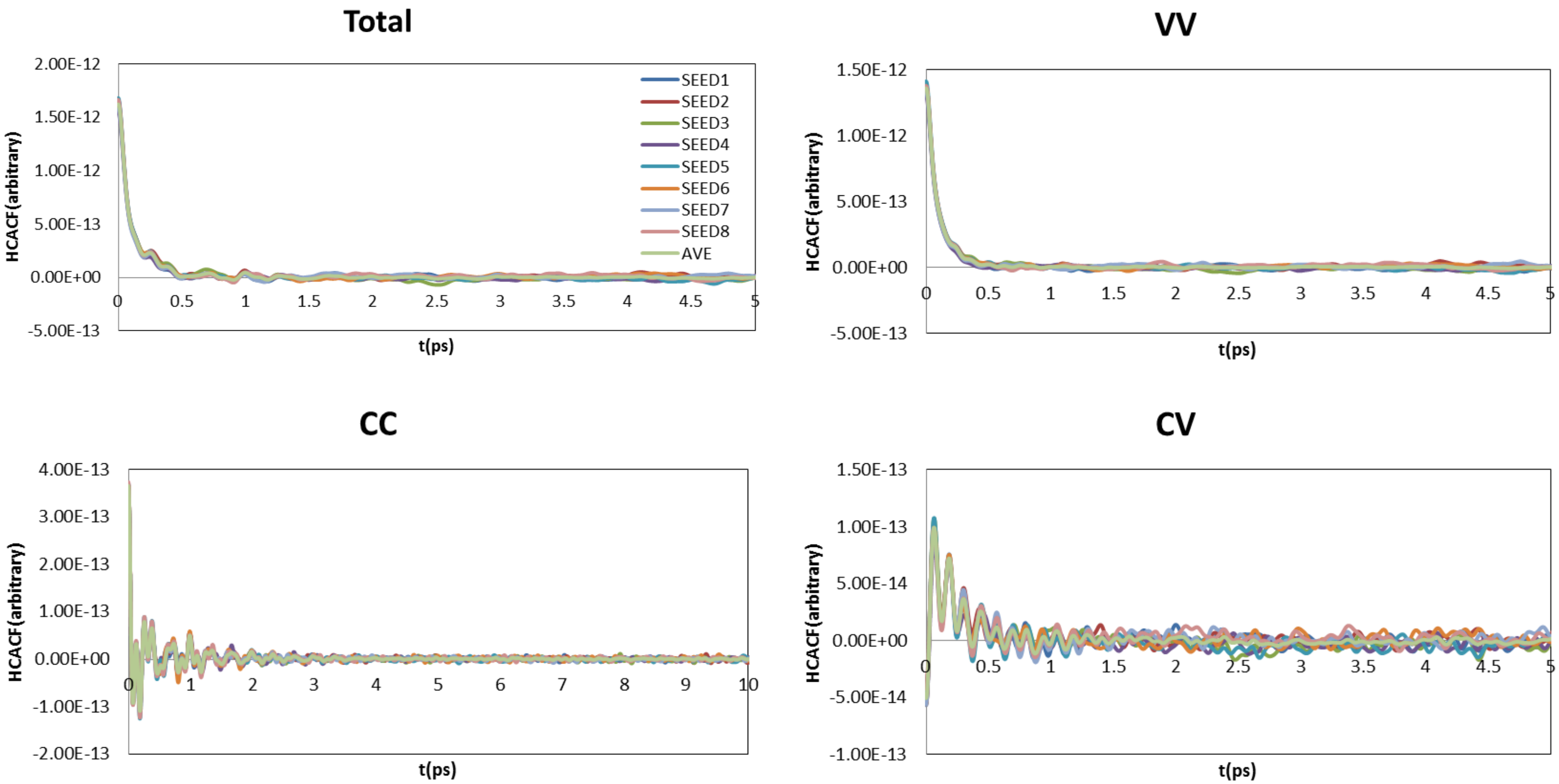

Figure 3.12 Total HCACF curve and curves for the *VV*, *CC* and *CV* components for the nanofluid case with *d*=12.703 Å nanoparticle at 0.35% volume percentage and *T*=110.

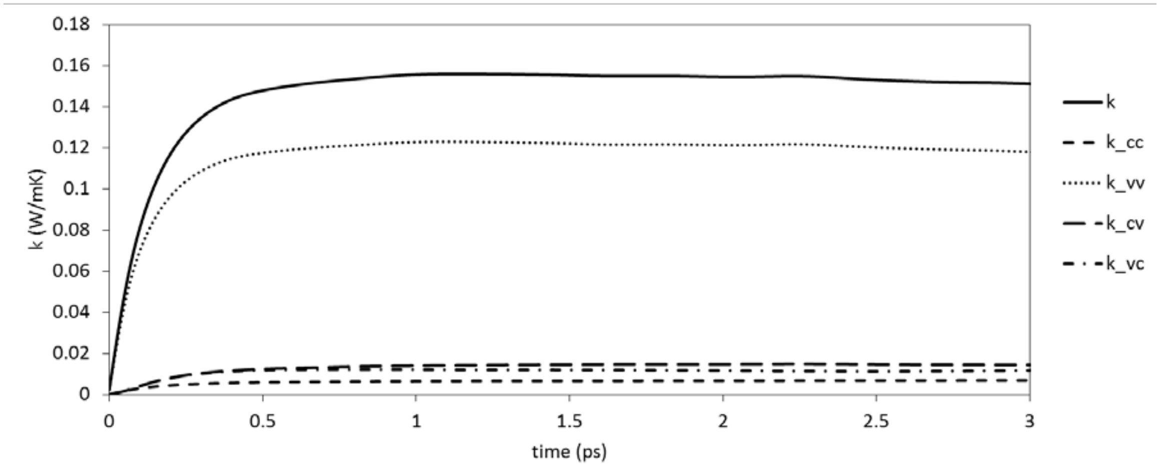

Figure 3.13 The curves for the total thermal conductivity and its components for pure methane at *T*=110 K. (The curves represent the time-integral for the HCACF curves)

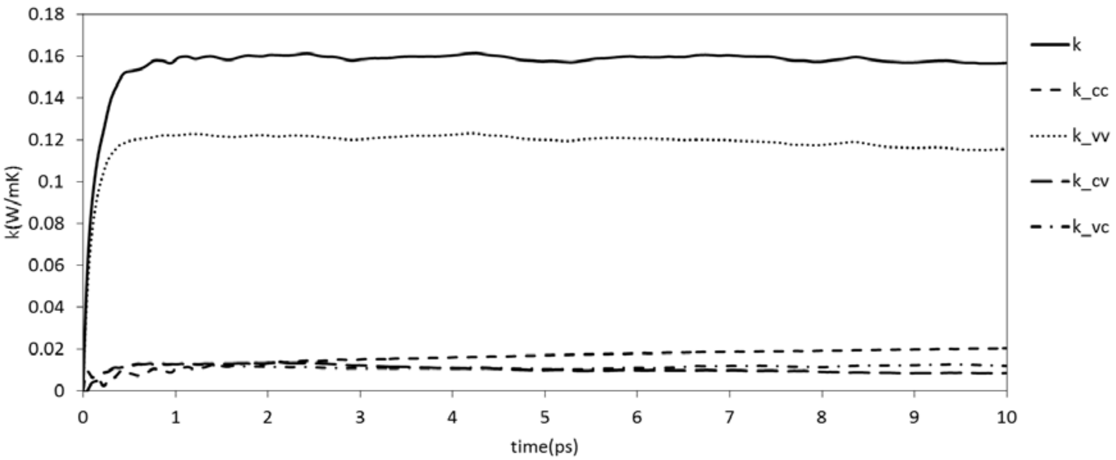

Figure 3.14 The curves for the total thermal conductivity and its components for the nanofluid case with *d*=12.703 Å nanoparticle at 0.35% volume percentage and *T*=110. (The curves represent the time-integral for the HCACF curves)

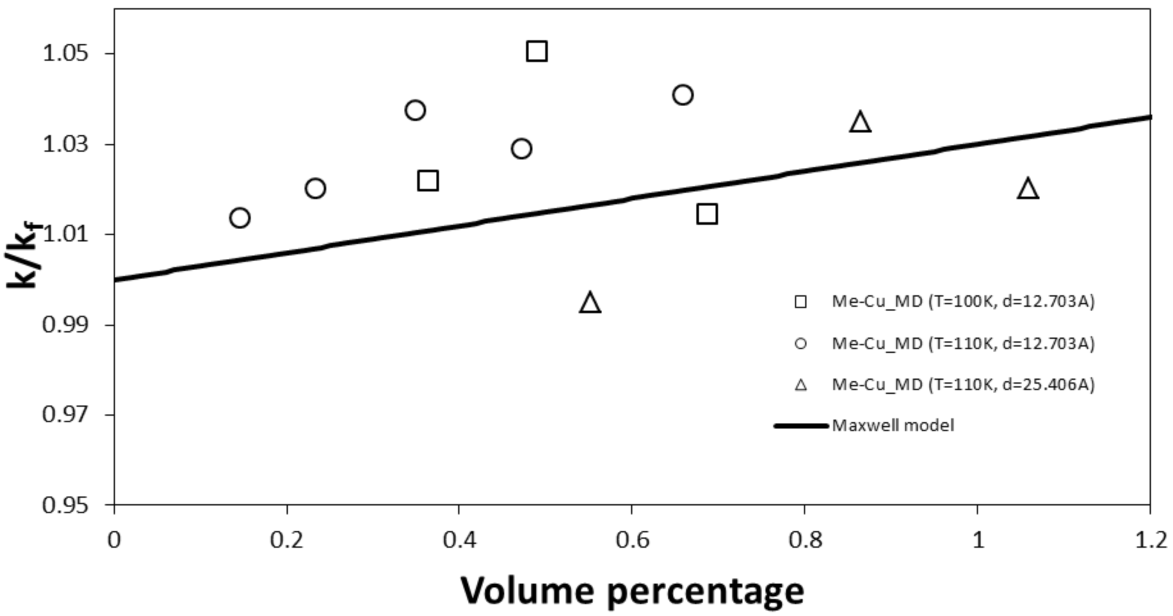

Figure 3.15 Thermal conductivity enhancement for different nanofluid cases along with the predicted results based on the Maxwell's model.

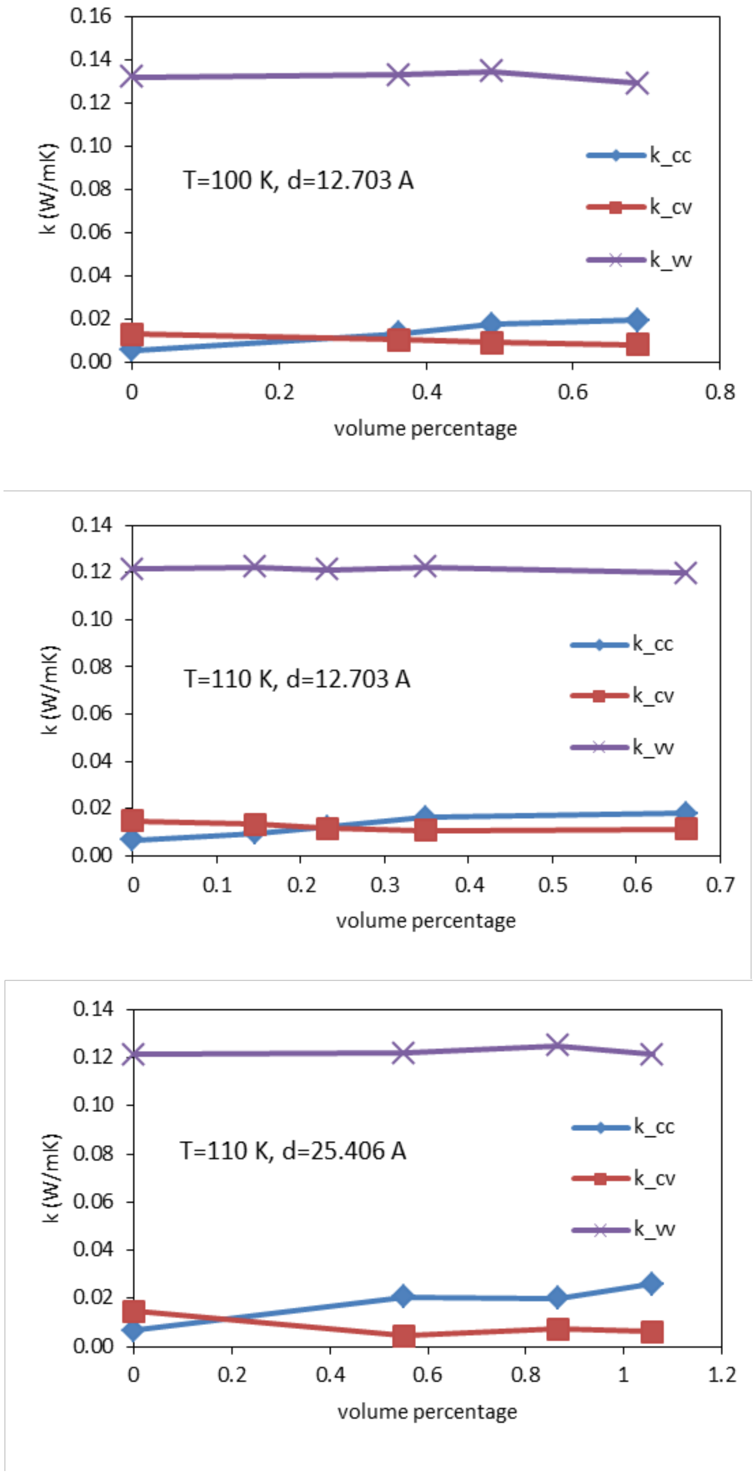

Figure 3.16 Contributions of various terms to the thermal conductivity as a function of particle volume percentages for various temperatures and particle sizes.

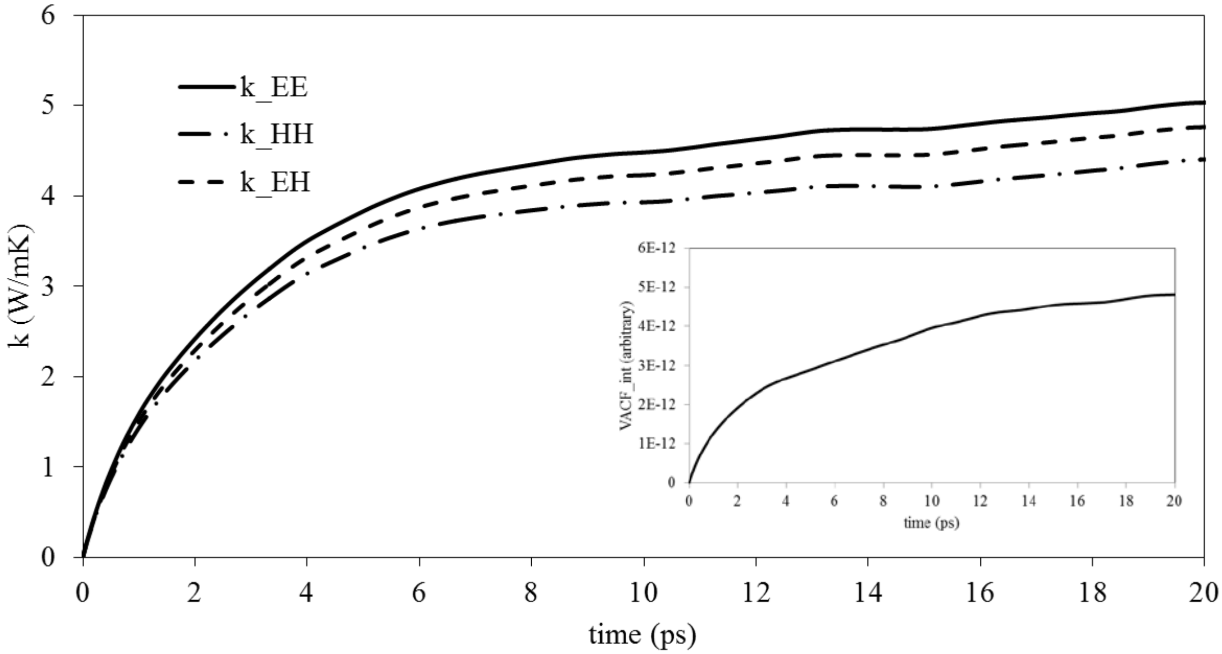

Figure 3.17 Time integrals of the correlation functions associated with the convective term contributions to the thermal conductivity for a nanofluid with 12.703 Å nanoparticle at 0.35% volume percentage and 110 K. The inset shows time integral of the center of mass velocity autocorrelation function.

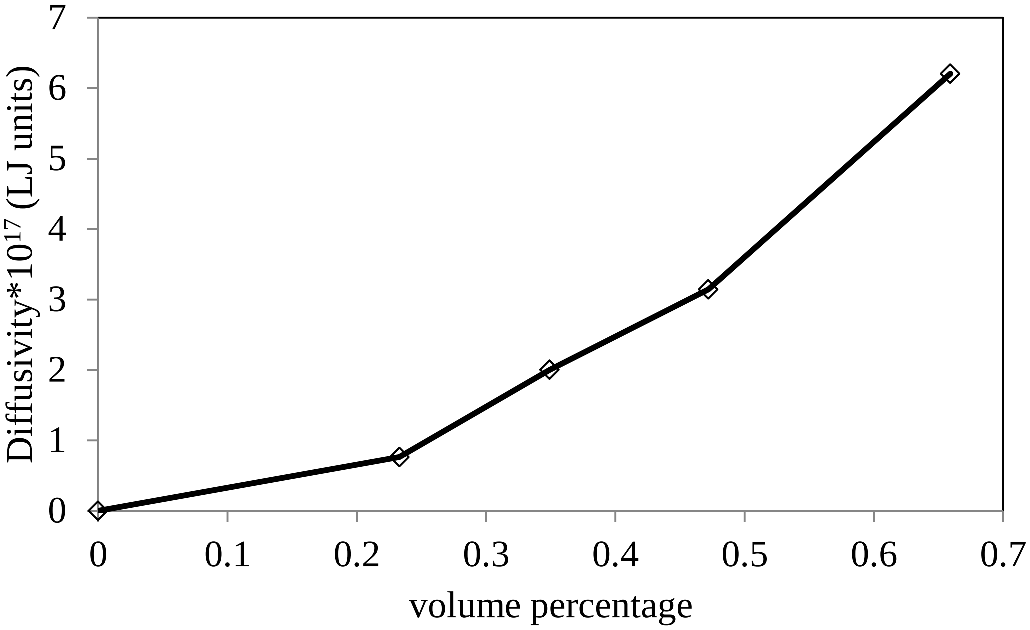

Figure 3.18 Self-diffusion coefficient of the nanoparticle as a function of the volume percentage.

Chapter 4 Improvement in thermal conductivity of paraffin by adding high-aspect ratio carbon-based nano-fillers

In this chapter, molecular dynamics (MD) simulations have been utilized to study the thermal conductivity of liquid and solid mixtures of paraffin and carbon-based high aspect-ratio nano-additives, i.e. carbon nanotubes and graphene.

Firstly, the relationship between the structure of paraffin in both solid and liquid states and its thermal conductivity has been studied. It is observed that upon crystallization, a nano-crystalline paraffin structure develops and the value of the thermal conductivity doubles, in agreement with experimental data. The introduction of carbon nanotubes or graphene layers leads to ordering of the liquid phase and associated thermal conductivity enhancement. More prominently, high aspect-ratio carbon-based nano-fillers provide a template for directed crystallization and lead to even greater thermal conductivity increases. Our results indicate that introducing carbon nanotubes and graphene into long-chain paraffins leads to a considerable enhancement in thermal conductivity, not only due to the presence of a conductive filler, but also due to the filler-induced alignment of paraffin molecules.

Secondly, the overall thermal conductivity values for mixtures of solid and liquid paraffin and CNT/graphene are calculated by MD simulations. In agreement with existing experimental data, high enhancements in thermal conductivity through adding these graphitic nano-additives into paraffin, particularly in the solid phase were observed. It will be demonstrated that this significant improvement is mainly achieved by the enhancement in thermal conductivity of the matrix itself due to the presence of the nanofiller rather than the high thermal conductivity of the additive.

4.1 Introduction

It was explained in the previous chapter that for well-dispersed suspensions of spherical nanoparticles, the thermal conductivity is described adequately by the effective medium theory and does not exhibit significant enhancement. However, carbon-based high aspect-ratio nano-additives, e.g. graphene and carbon nanotubes (CNT), have attracted great attention in thermal transport applications due to their promising role in improving the thermophysical properties. Improved phase change materials (widely known as nanostructure-enhanced phase change materials (NePCM)) (Khodadadi et al., 2013, Yavari et al., 2011, Elgafy and Lafdi, 2005, Kim and Drzal, 2009, Wang et al., 2009, Shaikh et al., 2008, Xiang and Drzal, 2011, Yu et al., 2013, Shi et al., 2013, Zeng et al., 2008, Zeng et al., 2009, Liu et al., 2009 and Cui et al., 2011) and paraffin-based nanofluids (Yu et al., 2010, Xie et al., 2009, Yu et al., 2007, Yu et al., 2008, and Yu et al., 2011) are such examples. Measurements and simulations have shown that adding graphene and CNT into paraffin, which is one of the common phase change materials, can lead to considerable improvement of its thermal conductivity (Elgafy and Lafdi, 2005, Kim and Drzal, 2009, Wang et al., 2009, Xiang and Drzal, 2011, Yu et al., 2013, Shi et al., 2013, Zeng et al., 2008, Zeng et al., 2009, Liu et al., 2009 and Cui et al., 2011, Yu et al., 2010, Xie et al., 2009, Yu et al., 2007, Yu et al., 2008, and Yu et al., 2011). Considering the high aspect-ratio of these fillers, such enhancement is also predicted from the modified version of the effective medium theory (the model proposed by Nan et al., 1997). However, the magnitude of the enhancement can be potentially reduced by the high value of the interfacial thermal resistance between

CNT/graphene and matrix material (Huxtable et al., 2003, Shenogin et al., 2004, Hu et al., 2001, and Hu et al., 2011).

The filler-matrix interface can also have a potentially positive effect on the thermal conductivity due to the ordering of the atomic structure at the solid-liquid interface (Keblinski et al., 2002). This idea is motivated by the fact that crystalline solids exhibit much greater thermal conductivity than their amorphous counterparts (Cahill and Pohl, 1989 and Cahill et al., 1992) due to the lack of polarized thermal waves (phonons) in amorphous materials as well as in liquids. However, molecular simulations of simple, small molecule liquids at solid interfaces indicate that interfacial order in the liquid has little effect on thermal transport (Xue et al., 2004).

The origin of the reported significant enhancement of thermal conductivity in such mixtures is still not quite clear. In the context of paraffin-graphene composites, Zheng et al. (2011) linked the thermal conductivity enhancement with clustering and percolation of fillers creating paths for rapid heat flow. They speculated that the internal high stress generated upon solidification increases the interfacial thermal conductance between particles and the matrix, leading to higher enhancement of thermal conductivity. However, the results of our molecular dynamics (MD) simulations suggest that the key to the improved thermal conductivity is the ordering of paraffin molecules induced by the carbon nanofillers that basically act as templates.

In the first part of this chapter (section 4.4), molecular dynamics simulation is utilized to study the thermal conductivity-structure relation for n-alkane (n-paraffins) molecules. In doing so, systems of pure solid/liquid paraffin, perfect crystal of paraffin molecules and mixtures of liquid/solid paraffin and CNT/graphene are modeled. To create the needed solid cases, the corresponding liquid systems are solidified except for the perfect crystal case for which the paraffin molecules were initially located on a crystal lattice points. The thermal conductivity calculations were carried out on the obtained systems. For solid cases, the potential size effect was also investigated. It should be noted that in this part of the chapter, for the mixture cases, the effect of fillers were not directly considered in determination of the thermal conductivity. In these cases, the fillers were just present in the systems in order to investigate their potential induced-ordering effect on the thermal conductivity of paraffin molecules. As a result, in this part of the chapter, the overall thermal conductivity values for mixtures are not calculated. The overall thermal conductivities will be presented in the second part of the chapter where unbounded suspended particles are considered within paraffin.

In the second part of this chapter (section 4.5), results of MD simulations for which the motion of the fillers is either frozen or fully unrestricted are reported. By comparing the predicted thermal conductivities from these two limiting sets of simulations, it will be demonstrated that the dominant factor leading to the enhancement in thermal conductivity originates from the ordering effect induced by the fillers on the matrix molecules.

Chapter 4 starts with a literature review on two subjects related to this study in section 4.2. In the first subsection of this section, the works related to thermal conductivity enhancement of PCM by adding high-aspect ratio carbon-based nano-fillers are reviewed. In the second subsection, a literature review is given on solidification/melting of paraffin and associated molecular dynamics studies. The simulation methodology is explained in section 4.3. We report the results of calculated thermal conductivity values in sections 4.4 and 4.5. In these two sections, the studied model structures are also presented. Finally, the summary and pertinent conclusions are presented in section 4.6.

4.2 Literature Review

4.2.1 Utilizing carbon-based high aspect-ratio nano-fillers and application to PCM

Yu et al. (2007) reported great enhancements in the thermal conductivity of epoxy by adding exfoliated graphite nanoplatelets. Based on the temperature used during the exfoliation process, the thickness of the nanoparticles could be varied. The measurements indicated that for thinner nanoplatelets, the thermal conductivity enhancement is higher, whereas for a loading of 25 vol% of 1.7 nm thick additives, the enhancement was 3000%. They attributed the observed high thermal conductivity values to the high value of the aspect-ratio, stiffness and interfacial thermal conductance of such particles.

Yu et al. (2011) performed thermal conductivity measurements on poly ethylene-based nanofluids containing graphene and graphene oxide nanosheets. The thermal conductivity enhancements for 5 vol% dispersion of graphene and graphene oxide nanosheets were reported to be 86% and 44%, respectively. The results indicated that graphene is more effective than graphene oxide in giving rise to thermal conductivity enhancement. To interpret the observed difference, they speculated that the shorter mean free path of the phonons in the graphene oxide due to the scattering brought about by the defects due to oxygen bonds causes the lower value of the thermal conductivity.

Yu et al. (2009) investigated the thermal conductivity of dispersions of graphene oxide nanosheets into different base fluids. For the same loading of 5 vol%, they reported 30.2%, 62.3%, and 76.8% improvements of thermal conductivity for the base fluids of distilled water, propyl glycol and liquid paraffin, respectively. For all reported volume fractions, paraffin base nanofluids exhibited the highest enhancements. They claimed that the high in-plane thermal conductivity of the graphene oxide nanosheets is the reason for the achieved high enhancements.

Yu et al. (2013) investigated the effect of utilizing different carbon nanofillers with different shapes and sizes on the thermal conductivity improvement in liquid paraffin. They tried different particles including pristine and carboxyl-functionalized short multi-walled carbon nanotubes (MWCNTs), long MWCNTs, carbon nanofibers, and graphene nanoplatelets (GNPs). Among these variety of nanoparticles, GNPs exhibited the highest thermal conductivity improvement. They suggested that the high interfacial thermal conductance for GNPs can be the reason behind the high enhancement.

Zheng et al. (2011) commented on different levels of thermal conductivity enhancement achieved for the liquid and solid phase graphite-hexadecane mixtures. They linked the thermal conductivity enhancement to clustering/aggregation and percolation of fillers creating paths for effective heat flow. They speculated that the internal high stress generated upon solidification increases the interfacial thermal conductance between the particles and the matrix, leading to higher enhancement for the solid phase mixtures.

Kim and Drzal (2009) observed noticeable improvements in thermal conductivity by dispersing exfoliated graphite nanoplatelets into paraffin-based PCM while the latent heat did not reduce considerably, indicating a desirable characteristic in phase change performance. Xiang and Drzal (2011) confirmed that the latent heat remains roughly unchanged after adding exfoliated graphite nanoplatelets into paraffin. Results corresponding to utilization of two kinds of exfoliated graphite nanoplatelets having two distinct aspect-ratios exhibited that the nanoplatelets with higher value of the aspect-ratio gave rise to greater enhancement in the thermal conductivity of the composite.

Yavari et al. (2011) reported attaining great enhancement in thermal conductivity of 1-octadecanol-based PCM through adding graphene. The observed that enhancement of thermal conductivity for only 4 mass% of graphene was 140% with a low reduction in the value of the latent heat.

Measurements by Shi et al. (2013) indicated that while graphene sheets are more effective in shape-stabilization of paraffin PCM, utilization of exfoliated graphite nanoplatelets give rise to higher enhancements in thermal conductivity of paraffin. For a 10 mass% loading of exfoliated graphite nanoplatelets, the observed enhancement was surprisingly as much as 1000%. The measured thermal conductivity values for solid and liquid phase mixtures suggested that for both nanoparticles, the solid phase mixtures exhibit higher enhancements in comparison with the liquid counterparts.

In the context of utilizing CNTs, Elgafy and Lafdy (2005) observed good thermal conductivity enhancement by adding carbon nanofibers (CNF) into paraffin wax PCM. They pointed out that surface characteristics of CNF have an important role in enhancement.

Xie and Chen (2009) investigated the thermal conductivity improvement by dispersing MWCNTs into ethylene glycol. By observing the thermal conductivity trends for samples prepared under different milling time durations, they concluded that the thermal conductivity enhancement depends mainly on the straightness ratio, aspect-ratio and aggregation of particles. The insignificant effect of temperature on the thermal conductivity, a phenomenon which has also been confirmed by most of other works mentioned earlier, suggested that the Brownian motion-induced convection is not an important element in thermal transport of such mixtures.

Wang et al. (2010) reported high thermal conductivity enhancement of CNT-Palmitic Acid composite PCM. They also observed that the hydroxyl functional group added on CNT surface augments the thermal conductivity of such composites. They also reported that temperature does not change the thermal conductivity of the composites.

Khodadadi, Fan and Babaei (2013) authored an overarching review paper on the effect of different nanofillers on thermal conductivity of liquid and solid phase base materials and concluded that the carbon-based high-aspect ratio nanofillers have the most marked effect on the thermal conductivity enhancement. Figure 4.1 (taken from the review paper) clearly shows that among mixture cases with different nanoparticle inclusions and phases, firstly, the carbon-based high aspect-ratio nanoparticles show greatest improvements in the thermal conductivity. Secondly, in these mixture cases, the solid phase cases exhibit higher thermal conductivity enhancements with respect to the corresponding liquid cases.

4.2.2 Molecular dynamics simulations of melting/solidification of n-paraffins

N-paraffins (n-alkanes) are long chains of hydrocarbons with the chemical formula C_nH_{2n+2}. By using X-ray on a single crystal of $C_{30}H_{62}$, Muller (1928) was the first to find a zig-zag structure for such molecules. Thereafter, researchers have been studying the crystals made of n-paraffin molecules (Bunn, 1939, Smith, 1953 and Luth et al., 1974). In addition, phase change of n-alkanes has been of great interest in academia.

Molecular dynamics simulation has been demonstrated to be a useful tool for researchers to study the topics related to crystal structure and phase change of paraffin molecules. In this context, features and phenomena such as crystal structure, surface crystallization of alkane chains, high-temperature crystalline rotator phases and order-disorder transition for n-paraffins have been investigated by MD simulations. Here, a selected number of such works are reviewed.

To my knowledge, the papers by Ryckaert et al. (1987 and 1995) are the first papers published on the investigation of rotator phase structures for paraffin molecules by using MD simulations. The structure and dynamics of solid phases (crystalline and pseudo-hexagonal rotator phases) of $C_{23}H_{48}$ around its melting temperature (at temperatures 38 ^{o}C and 42 ^{o}C, for orthorhombic and pseudohexagonal crystals, respectively) was investigated by Ryckaert et al. (1987). The disorder at the interface of the bilayer of alkane molecules was shown to be dominated by the longitudinal diffusion of the chains which was observed through enhanced fluctuations in the position of the central C atom. Simulations showed that the bilayer interface is the most hospitable place for the birth of intra-molecular defects. The structure of phase rotator R_I and dynamics of C_{19} molecules were also investigated and compared with spectroscopic experiments data by Ryckaert (1995). The results from simulations showed good agreements with the experimental data.

Marbeuf and Brown (2006) investigated the transition from ordered crystalline to melt for odd and even alkanes (alkanes having odd and even numbers of carbons are odd and even alkanes, respectively) C_{18}, C_{19}, C_{20} and C_{22} (C_n is used as abbreviation for C_nH_{2n+2}). Based on the number of carbons and whether it is odd or even, alkanes show different behaviors in melting process in terms of rotator phases before complete melting. They observed spontaneous transition of C_{19} to R_I rotator phase and C_{18} and C_{20} to R_I and R_{II}. They investigated the molecular motions initiating the transition to phase rotators before melting. They reported lattice parameters for the crystal of paraffins to be in good agreement with the experimental data. They used the all-atom condensed-phase optimized molecular potentials for atomistic simulation studies (COMPASS) force field (Sun, 1998) in the MD simulations.

Wentzela and Milner (2010) performed MD simulation to investigate the rotator phases of C_{23} and a 50-50 mixture of C_{21}-C_{23}. They examined different all-atom force fields for the alkane molecules and based on the comparison of the phase transition sequence (orthorhombic crystal to phase rotators and finally to melt) with the experimental observations, they reported the Flexible Williams force field (Williams, 1967) to be more accurate. They found that the time needed for structural equilibration to a final phase is considerable. They observed a more stable phase rotator for the 50-50 C_{21}-C_{23} mixture compared to the pure C_{23}.

Esselink et al. (1994) studied the phase change of different n-alkanes from butane to n-dodecane by utilizing MD simulations. They obtained the melting and crystallization temperatures for those n-alkanes. Moreover, they calculated the crystallization rate of nucleus.

Crystallization of n-decane molecules forming a film containing a free surface was investigated by Shimizu and Yamamoto (2000). They first performed simulation for melting of two types of crystals: one has a surface which had chain ends and the molecule axes were perpendicular to the surface and the other has a surface formed by the sides of molecules. They showed that the first type of crystal is more stable. They then investigated different crystalline structures corresponding to both slow and fast quenching of the more stable melt. In the slow crystallization, both surface monolayer and crystalline lamella exhibited hexagonal packing.

Waheed et al. (2002) utilized MD simulations to investigate the crystal growth of n-eicosane as a model n-alkane. They observed that introducing a crystal surface promotes crystallization in n-alkane. In order to obtain the rate of crystallization, they used the plots of local order parameter versus time and distance.

4.3 Simulation Methodology

The direct method for the determination of thermal conductivity was utilized in combination with the Non-equilibrium Molecular Dynamics (NEMD) simulation method (Schelling et al., 2002). In the direct method, a heat flux is imposed through the simulation box by adding heat to the molecules inside a planar slab (heat source) in one region of the box and extracting the same amount of heat from the molecules inside another slab (heat sink) in another region. Upon reaching the steady state, based on the Fourier's Law, the thermal conductivity of the material in the simulation box subject to the periodic boundary condition becomes $k = \frac{dQ/dt}{A(dT/dx_1 + dT/dx_2)}$, where dQ/dt is the rate of heat addition or extraction from the heat source and heat sink, respectively. Quantity A is the cross-sectional area of the simulation box normal to the direction of the imposed heat flux, whereas dT/dx_1 and dT/dx_2 are the temperature gradients of the two sides of the heat sink or heat source, respectively.

To describe n-alkane chains (n-octadecane in this study) interactions, the Nath, Escobedo and de Pablo-revised (NERD) force field (Nath et al., 1998) was used to describe the interactions among paraffin molecules. This potential consists of bonded interactions including bond stretching, bending and torsion as well as non-bonded interactions among CH_2 and CH_3 sites described by the LJ potential acting among sites in different molecules or among sites in the same molecule but at least four bonds away. The Tersoff potential (Tersoff, 1988) with Lindsay and Broido modification (Lindsay, 2010) was used to model the carbon atoms' interactions in carbon nanotubes (CNTs) and graphene. For the cross potential among carbon atoms in the CNT/graphene and the interaction sites of n-octadecane, the Lorentz-Berthelot mixing rule (Allen and Tildesley, 1989) was used for determining the LJ parameters between the n-octadecane sites and carbon atoms. The required LJ parameters for the carbon atoms in CNT and graphene for mixing calculations are extracted from Stuart et al. (2000).

The velocity Verlet algorithm was used to numerically integrate the Newton's equation of motion with MD time steps of 1 fs and 0.5 fs for pure n-octadecane and CNT/graphene-octadecane mixture cases, respectively. However, in the first part, after structure preparation and equilibration, the atoms forming CNTs and graphene were kept fixed, thus allowing for the determination of thermal conductivity solely due to alkane chains. All simulations were performed with the large-scale atomic/molecular massively parallel simulator (LAMMPS) molecular dynamics package (Plimpton, 1995).

4.4 Dependency of the thermal conductivity on molecule's alignment

In this section, the effect of alignment of paraffin molecules on its thermal conductivity will be investigated. In the first subsection, the model structures used in this study are presented. The models include pure liquid/solid paraffins, a perfect crystal of paraffin and mixtures of liquid/solid paraffin and CNT/graphene. In the second subsection, the alignment parameter is defined to assess the structural organization of the system. Finally, the thermal conductivity results are presented.

4.4.1 Model structures

4.4.1.1 Bulk Structures

The reference pure n-octadecane structure contains 600 $CH_3(CH_2)_{16}CH_3$ molecules in a cubic simulation box. The system was initially equilibrated at 300 K and 1 atm for 4,000,000 time steps under isothermal-isobaric ensemble (NPT) leading to an equilibrium liquid structure. To obtain the solid phase of the paraffin, the system was first heated to 320 K and then cooled down to 190 K at the rate of 2 K/ns. Snapshots of the solid and liquid structures at 190 K and at 300 K are shown in Figures 4.2 (a) and (b), respectively. The solid system clearly exhibits structural organization containing nano-domains of crystalline structures aligned in different directions.

As shown in Figures 4.2 (c) and (d), the abrupt drops in the potential energy and specific volume curves indicate that solidification occurs within the 230-250 K range, which is lower than the experimental value of 300 K (Gulseren and Coupland, 2007). The lower predicted crystallization point of the paraffin is believed to be caused by the lack of a nucleation core in the pure system and the existence of a barrier to crystallization. It should be noted that the unit of the potential energy is kcal per mole of n-octadecane. The thermal expansions of liquid n-octadecane at 300 K and solid n-octadecane at 280 K, based on the fitted straight lines to the volume curves in the liquid and solid phases, are 0.00117 K^{-1} and 0.00056 K^{-1}, respectively. The predicted thermal expansion for the liquid n-octadecane is in reasonable agreement with the reported experimental value of 0.00087 K^{-1} (Gulseren and Coupland, 2007). The re-melting process was performed by heating the system at the 2 K/ps rate. As shown in Figures 4.2 (c) and (d), melting occurs at a higher temperature of around 300 K. The melting temperature is very close to the experimental value of 300 K (Gulseren and Coupland, 2007). The calculated latent heat of fusion is 8.5 kcal/mol, whereas the experimental value is 14.67 kcal/mol (Himran and Suwono, 1994). This discrepancy might be associated with the fact that a united atom model is used without explicit representation of H atoms. The calculated density of the liquid n-octadecane at 310 K is 0.75 g/cm^3, which is in good agreement with the experimental value of 0.778 g/cm^3 (Gulseren and Coupland, 2007). The calculated density of the solid n-octadecane at 290 K is 0.86 g/cm^3, which is also in good agreement with the experimental value of 0.91 g/cm^3 (Gulseren and Coupland, 2007).

4.4.1.2 Perfect Crystal Structure

The basic unit of the model perfect crystal structure included 100 molecules located on a hexagonal structure. This structure was thermalized under the NPT conditions at 150 K and atmospheric pressure for 4,000,000 time steps and then heated to T=270 K over 4,000,000 time steps to reach T=270 K and thermalized for 2,000,000 time steps at 270 K. Fourteen repeated snapshots for perfect crystals at 150 K and 270 K are given in Figure 4.3. The perfect crystal at 150 K, in agreement with reported experimental and MD data (Marbeuf and Brown, 2006), is a triclinic crystalline structure with its *a*, *b* and *c* parameters equal to 4.2, 4.63 and 25.7 Å, respectively. At 270 K, the structure is slightly transformed (see Figure 3), which is perhaps due to the fact that the united atom model is not quite capable of describing the correct crystal structure (Ryckaert and Klein, 1986). However, this structure is almost perfectly-ordered and aligned, thus it can be used to determine the reference value of the maximum possible thermal conductivity that is realized along the direction parallel to the molecular axis due to efficient heat flow along the chain backbone.

4.4.1.3 Composite Structures

The system of n-octadecane-CNT suspension was made by suspending a 120 Å long (10, 10) single-walled carbon nanotube (SWCNT) containing 1,980 carbon atoms within 750 n-octadecane molecules (overall 15,480 atoms). The system was thermalized at 300 K and atmospheric pressure under the NPT conditions. The *x*- and *y*-dimensions of the simulation box were changing at the same rate responding to the average *xx* + *yy* stress, while the z-dimension (along the tube axis) changed independently. Periodic boundary conditions were used in all directions and the nanotube length of 123.6 Å was commensurate with the length of the simulation cell. The cross-section dimensions were 60.3 by 60.3 Å for the liquid and 56.4 by 56.4 Å for the solid. With these dimensions, the liquid and solid composites have CNT volume fractions of 7% and 7.9%, respectively. The snapshots of the solid and liquid suspensions are shown in Figures 4.4 (a) and (b), respectively.

The thermalized system was heated up to 340 K and then cooled down to 200 K at a rate of 2 K/ns. Then, the crystallized system was heated up with the same rate to 340 K. The potential energy curve for the cooling and heating cycle is shown in Figure 4.4 (c). Interestingly, crystallization occurs within the 250-270 K range, i.e., about 20 K higher than in the case of the bulk liquid. This indicates that the presence of the nanotube provides a nucleation site with a significantly lower energy barrier for crystallization. This is consistent with the snapshot of the solid structure at 200 K (Figure 4.4 (a)), which clearly shows that the nanotube provides a template for crystallization leading to paraffin molecules being aligned with the nanotube. As described in the next section, such an alignment has a major effect on thermal transport characteristics. Upon heating of the solid, there is a signature of gradual melting in the potential energy vs. temperature curve in Figure 4.4 (c) starting at 300 K. However, the abrupt completion of meting occurs at about 325 K, which is also higher than the 300 K characterizing the bulk system. The above results indicate that the presence of the nanotube filler significantly alters the kinetics, and perhaps also thermodynamics of melting and crystallization.

The system of n-octadecane-graphene mixture was made by suspending a 70 by 120 Å graphene sheet containing 3277 carbon atoms within 1000 n-octadecane molecules (overall 21,277 atoms). The system was thermalized at 320 K under the NPT condition, however, the graphene sheet was considered as a rigid plate that was allowed to move only in the direction normal to the sheet. A snapshot of the liquid system is shown in Figure 4.5 (b). The thermalized system was heated up to 360 K and then cooled down to 190 K at a rate of 4 K/ns. The snapshot of the solid mixture at 190 K is shown in Figure 4.5 (a). Then, the crystallized system was heated at the same rate to 360 K. The potential energy curve for the whole procedure is shown in Figure 4.5 (c).

According to Figure 4.5 (c), crystallization occurs within the 270-290 K temperature range, i.e. about 40 K higher than in the case of bulk liquid. This suggests that the planar solid interface accommodates nucleation even more effectively than the cylindrical CNT discussed earlier. As in the case of CNT, graphene also serves as a template for crystallization, leading to a highly ordered structure with molecules parallel to the graphene (Figure 4.5 (a)). Upon heating, the solid melts abruptly at T=320 K, which, as in the case of the CNT system, is about 20 K above the temperature at which the bulk structure melts.

4.4.2 Orientational Characterization

It is well known that due to the strong covalent bonding along the alkane chain, thermal energy can be effectively propagated when the chain is straight (Sasikumar and Keblinski, 2011). In all solid structures, chains are indeed straight, thus the thermal conductivity might be related to the orientation of the chains relative to the direction of the temperature gradient. To investigate this relationship, we will evaluate the molecular alignment parameter, *s*, defined as follows (Rigby and Roe, 1988).

$$s = \left| \frac{\langle \cos^2 \theta \rangle - 1/3}{2/3} \right| \tag{4.1}$$

where θ is the angle between the end-to-end vector of the individual molecules and the desired axis, with $\langle \ \rangle$ standing for the average over all molecules. The alignment parameter can vary from 0 to 1 with the limits corresponding to completely random orientation of molecules and molecules perfectly aligned along the desired direction, respectively.

4.4.3 Thermal Conductivity

The temperature profile within the bulk liquid in response to application of the direct method is shown in Figure 4.6. The curve exhibits a linear dependence which varies smoothly away from the heat source/sink regions. Based on the heat current and temperature gradient of the linear regions of the curve, the thermal conductivity of the liquid n-octadecane is determined to be 0.164 W/m K, which is in good agreement with the experimental value of 0.153 W/m K (Powell and Challoner, 1961). The alignment parameter for the liquid system is 0.02, which is close to the expected value of zero for randomly-distributed molecular end-to-end vectors with no structural organization.

It should be noted that for thermal conductivity calculations of all liquid and solid cases, the systems at stable points within the phase transition diagrams are considered where there is no chance of phase change during thermal conductivity calculations. For example, if a liquid system at low temperatures where solidification has not occurred yet is considered there is a high chance of phase change as perturbations are introduced in systems along with NEMD simulations.

Thermal conductivity of the solid at 270 K was also calculated by using the direct method. Since the system is potentially anisotropic, the thermal conductivity values were determined in all three directions (*x*, *y* and *z* axes). Furthermore, to evaluate the possible size effect, we replicated the original system two, three and four times in the direction of the heat flux. The thermal conductivity values along the *x*-, *y*- and *z*-directions and different simulation cell sizes are given in Table 4.1. The finite-size effect is observed to be insignificant in all cases, and the average value (over 3 directions) of the thermal conductivity of the solid is about 0.3 W/m K, which is close to the reported measured thermal conductivity value of 0.33 W/m K for solid n-octadecane at 275 K (Yarborough and Kuan, 1981).

For the perfect crystal system at *T*=270 K, in order to obtain the thermal conductivity, the system was replicated in the directions parallel and normal to the molecular axis, and the systems were then equilibrated for 1,000,000 time steps. To investigate the size effect on the thermal conductivity, the system was replicated 6, 10, 12 and 14 times in the direction of the molecular axis and it was replicated 3, 6, 8 and 10 times in the normal-to-molecular direction. The systems attained the steady-state after 4,000,000 MD steps and the temperature profiles (see Figure 4.7) were averaged over 2,000,000 time steps. The temperature profile in Figure 4.7 exhibits a stepwise behavior wherein the entire temperature drops occur essentially at the interfaces between the crystalline layers of n-octadecane. Within each layer, the temperature is constant due to the ballistic phonon transport along straight alkane chains (Sasikumar and Keblinski, 2011). From the thermal conductivity value of k=1.13 W/m K, one can estimate the interfacial thermal conductance, G, as $G=k/d$, where d is the layer thickness. Using d=2.7 nm, one obtains G≈400 MW/m^2 K.

It should also be noted that the calculated temperature differences for interfaces of the layers where the heat source and sink slabs are located are higher than the temperature differences for other interfaces. These regions next to the heat source and sink slabs are excluded in evaluating the temperature gradient required for the thermal conductivity calculations. There could be two possible reasons behind the observed higher temperature differences at these interfaces. Firstly, locating the heat source or sink on a region in the simulation box introduces boundary thermal resistance which leads to higher temperature differences. Secondly, as it has been demonstrated by Hu et al. (2011), there is an internal resistance for interfaces containing the heat source or sink on one of its sides. This internal resistance is explained by the observation that heat transfer at interfaces is mainly due to low frequency phonon modes and thermal energy of high frequency modes should first cascade to low frequency modes in order to pass across interfaces.

To extrapolate the data to macroscopic lengths, in Figure 4.8, we plot the inverse of the computed thermal conductivity vs. the inverse of the simulation cell length (1/L) in the z- and x-directions. The intercept of the vertical axis at the 1/L = 0 limit yields the inverse of the macroscopic thermal conductivity (Schelling et al., 2002). By applying the curve-fit to the data, we obtained the thermal conductivity along the directions of the molecular chains and perpendicular to the chains to be equal to 1.13 and 0.35 W/m K, respectively. The first value that is above 1 W/m K is several times greater than that characterizing bulk solid paraffin and is identified as the upper limit for the thermal conductivity enhancement associated with molecular alignment. The perpendicular-to-the-chain thermal conductivity is also quite high; this is likely associated with the collective phonon motions over long distances in the perfect crystal structure.

The above results suggest that the molecular alignment along a particular direction can increase the thermal conductivity in that direction significantly. Such alignment can be induced/promoted by the presence of a carbon nanotube (CNT), and is clearly observed for solid paraffin, as shown in Figure 4.4(a). To determine the thermal conductivity of such structures, the solid (270 K) and liquid (300 K) CNT composites structures described in section 4.4.1.3 were first duplicated in the direction of the CNT axis. In the case of the solid composite, to investigate the size effect, we further replicated the structures two, three and four times. It should be noted that replicating the system gives rise to a longer CNT with no defects/disorder at the sides of the original simulation box because the periodic boundary conditions were applied on the original simulation box. The snapshots and temperature profiles for the solid and liquid CNT composite are shown in Figure 4.9. It should be noted that during the production run, the CNT carbon atoms were kept at fixed positions, thus allowing an investigation of the effect of the presence of the CNT on the paraffin’s thermal conductivity. The temperature profile for the liquid system (Figure 4.9 (b)) shows a linear smooth curve while for the solid system, the temperature profile (Figure 4.9 (d)) similar to the perfect crystal case exhibits a stepwise behavior corresponding to temperature drops at the interfaces between layers of n-octadecane (see Figure 4.9 (c)).

The thermal conductivity values along the CNT axis for the liquid and solid phases and the corresponding alignment parameter values are given in Table 4.2. Both liquid and solid phases exhibit enhancement with respect to the thermal conductivity values of pure liquid and solid n-octadecane, respectively.

For the case of the liquid CNT mixture, the thermal conductivity value of about 0.25 W/m K constitutes an increase of 48% over the bulk liquid value. This increase is likely associated with the alignment of molecules, even in the liquid phase. While the alignment parameter has a relatively low value of 0.11, the molecules next to and near the tube wall exhibit much stronger alignment. In fact, according to Figure 4.10, the alignment parameter on the tube surface is about 0.8 and even at several nanometers away from the tube, the orientation of the molecules are still not random. We attribute this long-range structural interfacial effect to the relatively long length of the liquid molecules. In the case of short liquid molecules, the interfacial effect on the structures is limited to ~1 nm distance (Xue et al., 2004).

The local thermal conductivity as a function of the distance from the nanotube’s axis is also shown in Figure 4.10. The value of the local thermal conductivity was obtained by calculating a local heat current via a molecular-level formula (Irving and Kirkwood, 1950), averaging the heat current over cylindrical shells concentric with the nanotube axis, and normalizing it by the cross-sectional area of the shell. The local thermal conductivity obtained in this manner has a high value of 0.4 W/m K at the closest distance from the surface of the nanotube, and remains elevated over the bulk value even 2 to 3 nm away from the surface of the nanotube. Therefore, by contrast to the small molecule liquids (Xue et al., 2004), in the case of long linear molecule liquids, the ordered interfacial structure of the liquid has a significant effect on the thermal conductivity enhancement.

The thermal conductivity of the solid paraffin-CNT system is 0.5 W/m K that is over 66% greater than the corresponding value for the bulk solid. The alignment parameter is 0.908, which is very close to the value characterizing a perfect crystal. While the enhancement of the thermal conductivity is noticeable, despite a highly-aligned molecular structure, the thermal conductivity is only about half of the value of the perfect crystal upper limit. One might attribute this to the somewhat defective structure (see Figure 4.9 (c)) and the presence of the nanotube. Both factors can scatter phonons and thus reduce the signature thermal conductivity.

Using analogous procedures similar to the CNT-based composite systems, we also determined the thermal conductivity for n-octadecane-graphene systems. We observed that both liquid and solid phases exhibit enhancement with respect to the thermal conductivity values of pure liquid and solid n-octadecane. The predicted thermal conductivity for the liquid-graphene suspension is 0.25 W/m K, which is about 52% above the bulk value. For the solid-graphene composite, the thermal conductivity is 0.56 W/m K, which is about 87% above the bulk value. The experimental values for the thermal conductivity enhancement for a 5 vol% liquid paraffin-graphene oxide suspension (Yu et al., 2011) and a 4 wt% solid 1-octadecanol-graphene composite (Yavari et al., 2011) are 86% and 140%, respectively. In agreement with the experimental data, the predicted values show that the thermal conductivity enhancement for the solid mixture is higher than the thermal conductivity enhancement for the liquid mixture.

4.5 A proof for the dominant role of ordering mechanism in thermal conductivity enhancement

In this part of the chapter, a study on the role of the molecular alignment on the overall thermal conductivity of CNT/graphene-paraffin mixtures is presented. In doing so, two sets of MD simulations are designed for the mixtures. In one set of simulations, the thermal conductivity of the mixtures are obtained while the motion of the carbon atoms within the nano-fillers are fully considered. In the other set of simulations, the thermal conductivity values for the mixtures are calculated while the carbon atoms inside nano-fillers are frozen in space. The effect of the molecular alignment on the overall thermal conductivity is determined by comparing the results of these two sets of MD simulations.

4.5.1 Model structures

4.5.1.1 Graphene mixtures

The first model system of a graphene-octadecane mixture was made of 2000 octadecane molecules and a suspended single-layer 40×40 $Å^2$ graphene sheet including 666 carbon atoms. Periodic boundary conditions were applied in all directions of the simulation box. The time step was 0.5 fs. The system was first thermalized under the isothermal-isobaric conditions (NPT ensemble) at T=320 K and P=1 atm. The size of the simulation box becomes ~100×113×100 $Å^3$ at the end of the thermalization process.

To generate the solid mixture, this system was first cooled down to 220 K and then heated up to 280 K at a rate of 4 K/ns. The resulting volume fractions for the liquid and solid mixtures were 0.46% and 0.54%, respectively. The snapshots of the liquid and solid mixtures along with the corresponding views of the graphene sheet with the matrix molecules removed at the same instants are shown in Figure 4.11. The snapshots for the liquid and solid mixtures indicate that upon solidification, the paraffin's molecules mostly aligned in parallel-to-the-graphene surface direction. It should be noted that the different direction of the graphene sheet with respect to the sides of simulation box that is observed for the liquid and solid mixtures is due to the motion and rotation of the graphene sheet before solidification gets started.

4.5.1.2 CNT mixtures

For the CNT-paraffin mixture, the model structure and all the steps of obtaining the liquid and solid mixtures are similar to the graphene-paraffin mixture case except that instead of the graphene sheet, a 6 nm long (5, 5) CNT containing 490 carbon atoms is suspended in the system yielding a mixture with 1.14 wt%. In this case, the liquid is thermalized at 300 K. The solidification process is similar to the graphene case. The volume fractions for the liquid and solid mixtures were 0.43% and 0.49%, respectively. The snapshots of the liquid and solid mixtures along with the corresponding view of only the suspended CNT are shown in Figure 4.12.

It should be noted that in all the studied systems, no aggregate or overlap forms among nanoparticles. The simulation setup is selected so that a well-dispersed mixture is modeled, a mixture in which the distance among the nano-objects is too long to create a percolated network of nanofillers.

In order to directly evaluate the contribution of the thermal conductivity of the matrix alone, for selected simulations we fixed the position of the carbon atoms in the CNT and graphene. In doing so, heat transport is only due to the paraffin matrix molecules. Of course, the presence of the frozen fillers affects the structure of the paraffin, thus indirectly influencing the thermal conductivity. However, direct contribution of the carbon fillers to thermal transport is completely eliminated in this case.

4.5.2 Thermal Conductivity

For all thermal conductivity simulations, the amount of heat added/extracted into/from heat source/sink is 0.04 kcal/mol per 1 fs. Then, the systems were allowed to reach the steady-state condition. Upon attaining the steady-state condition, the temperature profiles were obtained by averaging temperatures of the slabs normal to the heat flux direction over 1,000,000 time steps. As an example, the temperature profile for the liquid graphene-octadecane mixture in the *x*-direction is shown in Figure 4.13. The temperature profile is nearly linear and smooth from which the temperature gradient is extracted in order to determine the thermal conductivity of the liquid mixture.

Since the size effect should be studied for calculating the thermal conductivity of crystals, for solid cases, the solid systems were replicated two, three and four times in all directions of the simulation boxes. Then, the inverse of the computed thermal conductivities are plotted against the inverse of the length of the simulation box and the value of the thermal conductivity is obtained by extrapolating the curve-fit to $1/L=0$. As an example, for the solid graphene-octadecane mixture in the x-direction, the inverse of the thermal conductivity is plotted against the inverse of length of the domain in Figure 4.14.

A summary of MD direct method-determined thermal conductivity values are given in Table 4.3. For the liquid graphene-octadecane mixtures, the calculated thermal conductivity values based on the temperature gradients and the imposed heat flux values are 0.21, 0.21 and 0.20 W/m K in the *x*-, *y*- and *z*-directions, respectively. For the liquid CNT-octadecane mixtures, the calculated thermal conductivity values are 0.20, 0.22 and 0.21 W/m K in the *x*-, *y*- and *z*-directions, respectively. The thermal conductivity values in all directions are very similar, suggesting isotropic behavior for this specific thermal transport property. The thermal conductivity enhancement with respect to the thermal conductivity value for pure octadecane (0.164 W/m K) (previously calculated in section 4.4.3) is 28% for both graphene and CNT mixtures.

For the solid graphene-octadecane mixture, the molecules of octadecane are more aligned in the *x*- and *y*- directions. This might lead to higher thermal conductivity values as well as possible size effects. To assess the size effects, the inverses of the thermal conductivities were plotted against the inverse of the length of the simulation box size (L) and the value of thermal conductivity was obtained by extrapolating the curve-fit to $1/L=0$. For the *z*-direction case, the values of the thermal conductivity for different box lengths were similar and they did not increase with length. The calculated thermal conductivities are 0.57, 0.48 and 0.43 W/m K along the *x*-, *y*- and *z*-directions, respectively. The average of mixture thermal conductivity values over different directions is 0.49 W/m K. With respect to the solid pure octadecane (see section 4.4.3), the average thermal conductivity enhancement is 64%.

For solid CNT-octadecane mixture, the calculated thermal conductivity values are 0.52, 0.57 and 0.42 in the *x*-, *y*- and *z*-directions, respectively. The average value of the thermal conductivity over different directions shows an enhancement of 68% with respect to the thermal conductivity of pure octadecane.

The predicted thermal conductivity values for the liquid and solid phase mixtures exhibit considerable enhancements with just ~0.5 vol% of CNT/graphene loading. The results also demonstrate higher enhancements for the solid cases when compared to the liquid cases. This is in agreement with the results of recent experiments (Yavari et al., 2011, Yu et al., 2013, Shi et al., 2013, Zeng et al., 2008 and Zeng et al., 2009) on mixtures of different graphitic nano-particles and paraffin in solid/liquid phases.

The calculated high thermal conductivity enhancements are generally consistent with the reported experimental data on thermal conductivity enhancement by adding carbon-based high aspect-ratio nanofillers (see Table 4.4). Note that in Table 4.4, data are extracted from the papers based on the volume fractions or mass fractions that are used in the present simulations (0.5 vol% or 1 wt%). A figure of merit can be defined and added to the table to exhibit the performance of different carbon-based high aspect-ratio nanofillers. The figure of merit is defined as the relative thermal conductivity divided by the volume fraction of the sample

(Khodadadi et al., 2013). It is observed that GNP has the highest performance in enhancing the thermal conductivity of the matrix.

For the solid graphene-octadecane mixture case in which the motions of the carbon atoms of the filler are frozen, the calculated matrix thermal conductivity in the *x*-direction is 0.56 W/m K that is very close to the thermal conductivity of the mixture when the filler exhibits its full dynamics. It should be noted that for all lengths of the simulation box, the thermal conductivity values (not given here) were also very close. For the solid CNT-octadecane mixture, the matrix thermal conductivity in the *y*-direction is 0.63 that is a little different from the thermal conductivity of the whole mixture. In this case, the thermal conductivities for two lengths were similar and the difference arises from just one of the lengths. These results suggest that the increase in the thermal conductivity of paraffin upon adding carbon-base nano-fillers originates mainly from the ordering of matrix molecules due to the presence of such fillers. CNT and graphene additives act as templates for forming a more structurally-organized paraffin. Due to the polarized vibrational waves, structured materials exhibit higher thermal conductivity values. Consequently, ordering of the paraffin molecules induced by these nano-fillers results in the observed enhancement in the thermal conductivity. Based on this finding, moving toward methods in which more ordered matrices are formed will be more effective in thermal transport considerations.

Finally, in order to investigate the effect of the inclusion fraction on the thermal conductivity of mixtures, MD simulations were performed for cases with a doubled value of graphene mass fraction. We doubled the mass fraction in two different ways: (1) using two particles with the same size and (2) using a bigger single particle with doubled surface area. For the solid phase of case (1), the thermal conductivity values in the *x*-, *y*- and *z*-directions are 0.66, 0.57 and 0.53

W/m K, respectively, whereas for case (2), the corresponding values are 0.67, 0.43 and 0.45 W/m K, respectively. The results for both cases exhibit markedly higher improvements when compared to the lower mass fraction case discussed previously. However, the thermal conductivity for the liquid phase of both cases is 0.22 W/m K, suggesting a modest increase in enhancement comparing to the lower mass fraction case.

4.6 Summary and Conclusions

Molecular dynamics simulations were performed to investigate the effect of the alignment of n-octadecane molecules on its thermal conductivity. The influence of adding CNT and graphene on the alignment of molecules and consequently, on the thermal conductivity in the direction along which the molecules are aligned was also studied.

A summary of the thermal conductivity values obtained using the direct method and alignment parameter values for all different systems were provided. The predicted thermal conductivity values exhibit a strong dependency of the thermal conductivity along a particular direction on the alignment parameter in that direction. The solid CNT-octadecane mixture exhibits an enhancement of 66% when compared to the pure solid. The enhancement for the liquid CNT-octadecane suspension is 48%. Also, for the graphene-octadecane mixture, the enhancement of the solid phase (87%) is higher than the liquid phase (52%). The fact that the solid mixture accommodates greater enhancement of the thermal conductivity is due to significant ordering brought about by directed crystallization.

Moreover, the overall thermal conductivity enhancement in suspensions of carbon-based nano-fillers and paraffin was investigated. The numerical results, in agreement with existing experimental data, exhibited much higher thermal conductivity values with respect to the effective medium theory predictions. The contribution of the thermal conductivity of the matrix -

when the filler is present but does not conduct heat - on the overall thermal conductivity was studied. The results suggest that the thermal conductivity enhancement is linked mainly to the structuring effect of these high aspect-ratio fillers on the matrix molecules. The more-ordered structure of the matrix molecules in presence of fillers, which in turn becomes more similar to the perfect crystal structure, exhibits improved thermal transport property. The results demonstrate that this ordering mechanism is responsible for the observed high enhancements of the thermal conductivity.

Table 4.1 Thermal conductivity and alignment parameter values for the solid n-octadecane system in different directions with three different lengths of the simulation cell.

Direction	**Length (Å)**	**k (W/m K)**	**Alignment parameter**
X	133	0.364	0.22
X	200	0.324	0.22
X	265	0.329	0.22
Y	133	0.219	0.05
Y	200	0.280	0.05
Y	265	0.285	0.05
Z	133	0.251	0.16
Z	200	0.235	0.16
Z	265	0.271	0.16

Table 4.2 Summary table for thermal conductivity values and alignment parameters for all cases.

Case	**Phase**	**Temperature (K)**	**k (W/m K)**	**Alignment parameter**
Pure	**Liquid**	300	0.164	0.02
Pure	**Solid**	270	0.30	0.15
Pure	**Perfect crystal – along molecules**	270	1.126	0.987
Pure	**Perfect crystal perpendicular**	270	0.347	n/a
CNT-mixture	**Liquid**	300	0.243	0.11
CNT-mixture	**Solid**	270	0.499	0.908
Graphene-mixture	**Liquid**	320	0.249	0.20
Graphene-mixture	**Solid**	270	0.560	0.28

Table 4.3 MD-calculated thermal conductivity of CNT/graphene-octadecane mixtures in liquid and solid phases.

Filler	Phase	direction	Overall thermal conductivity (W/m K)	Octadecane thermal conductivity (W/m K)
Graphene	liquid	x	0.21	
		y	0.21	
		z	0.20	
	solid	x	0.57	0.56
		y	0.48	
		z	0.43	
CNT	liquid	x	0.20	
		y	0.22	
		z	0.21	
	solid	x	0.52	
		y	0.57	0.63
		z	0.42	

Table 4.4 Experimental data for thermal conductivity enhancements and observed figure of merit by adding different carbon-based nanofillers including graphene nanoplatelet (GNP), CNT, graphene oxide nanosheet (GON) and graphene.

Authors	Filler	Matrix	Volume or weight percentage	Phase	Thermal Conductivity Enhancement	Figure of Merit
Kim and Drzal (2009)	GNP	paraffin	1 wt%	solid	~40%	
Xiang and Drzal (2011)	GNP	paraffin	2 vol%	solid	~195%	97.5
Yu et al. (2013)	GNP	paraffin	1 wt%	liquid	20%	
Shi et al. (2013)	GNP	paraffin	1 wt%	solid	~60%	
Shi et al. (2013)	GNP	paraffin	1 wt%	liquid	~55%	
Xie and Chen (2009)	CNT	Ethylene Glycol	0.6 vol%	liquid	~20%	33.33
Yu et al. (2010)	GON	paraffin	5 vol%	liquid	76.8%	15.36
Wang et al. (2009)	CNT	Palmitic Acid	1 wt%	solid	46%	
Yu et al. (2007)	Graphene	Ethylene Glycol	5 vol%	liquid	86%	17.2
Yavari et al. (2011)	Graphene	1-octadeconal	1 wt%	solid	38%	

Figure of Merit = Thermal Conductivity Enhancement / Volume Fraction

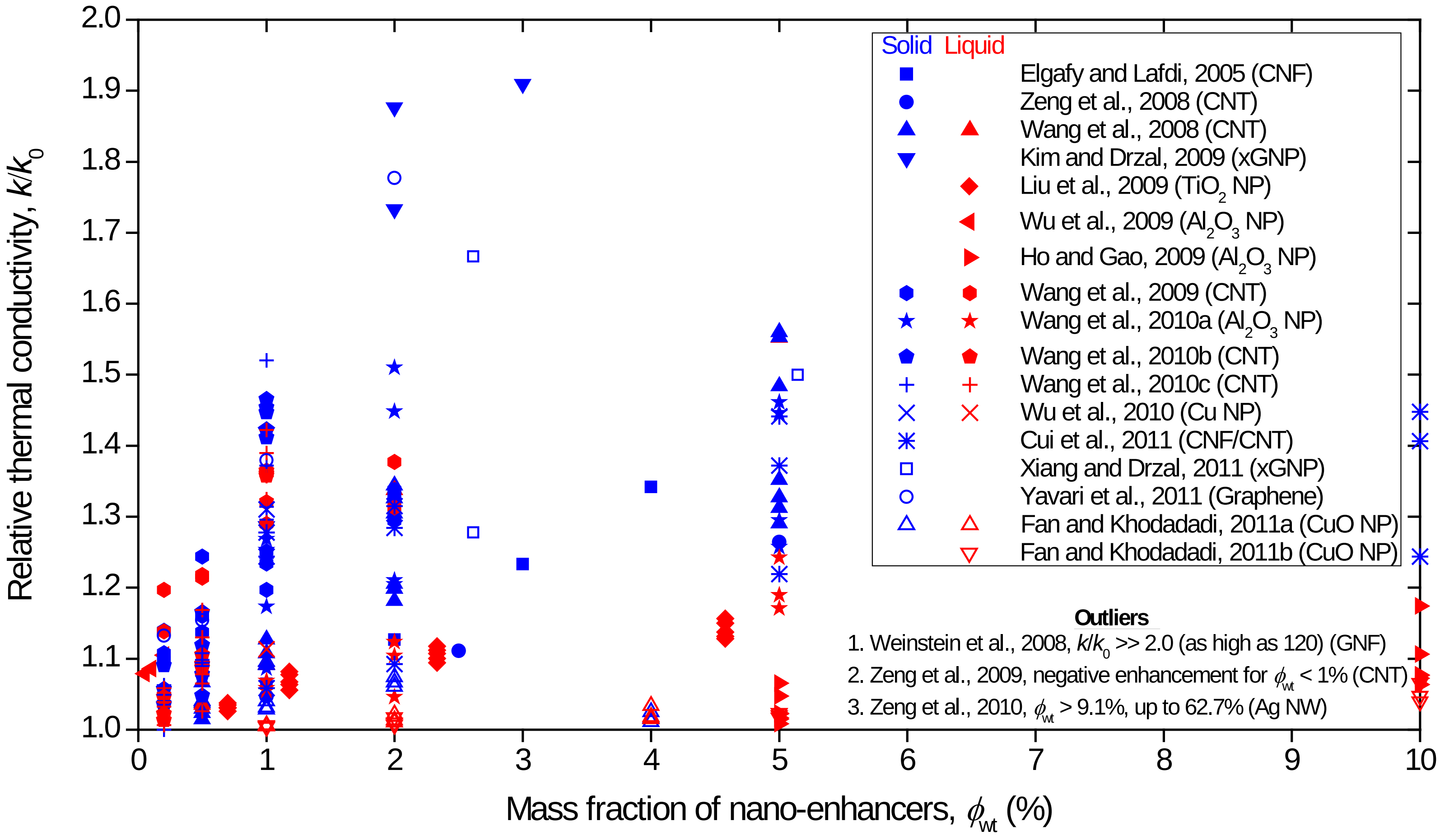

Figure 4.1 Effect of different nano-additives on thermal conductivity enhancement of liquid and solid phase base materials (Khodadadi et al., 2013).

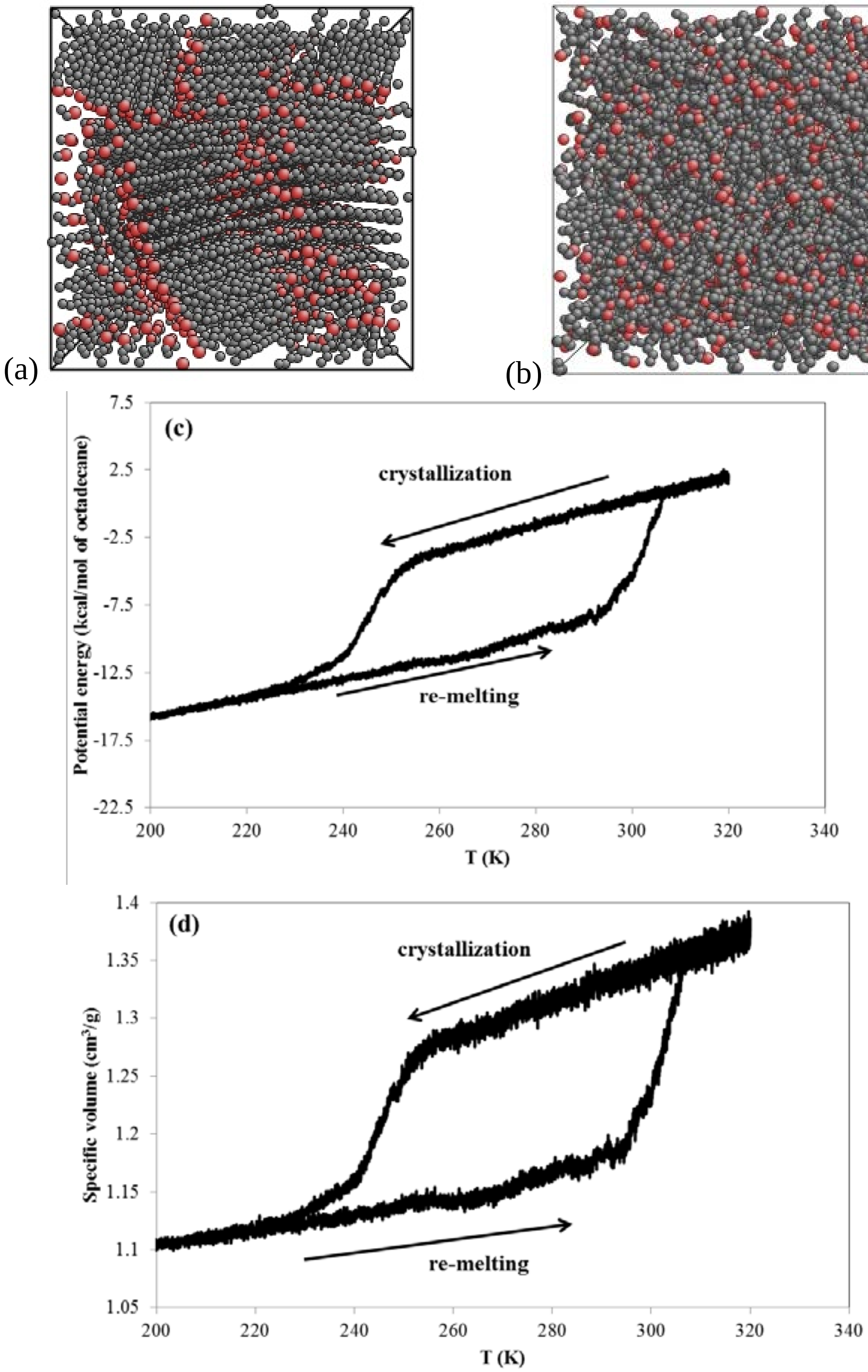

Figure 4.2 Snapshots of the (a) solid at 190 K and (b) liquid at 300 K. The potential energy (c) and the specific volume (d) curves for crystallization and re-melting processes.

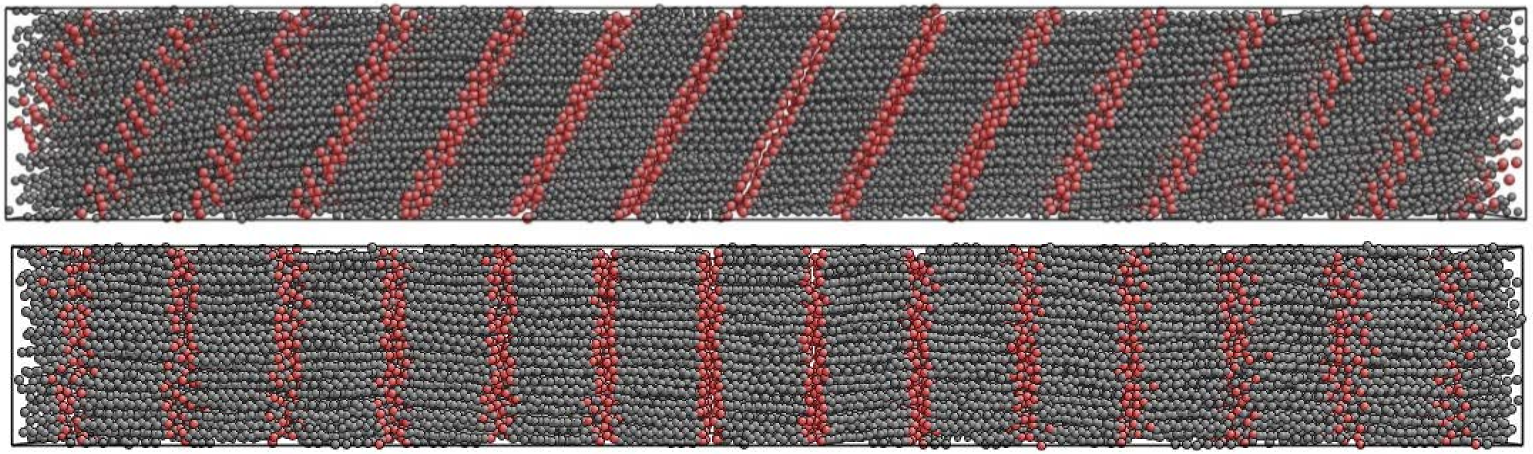

Figure 4.3 Snapshots of the perfect crystal structure at *T*=150 K (top panel) and *T*=270 K (bottom panel)

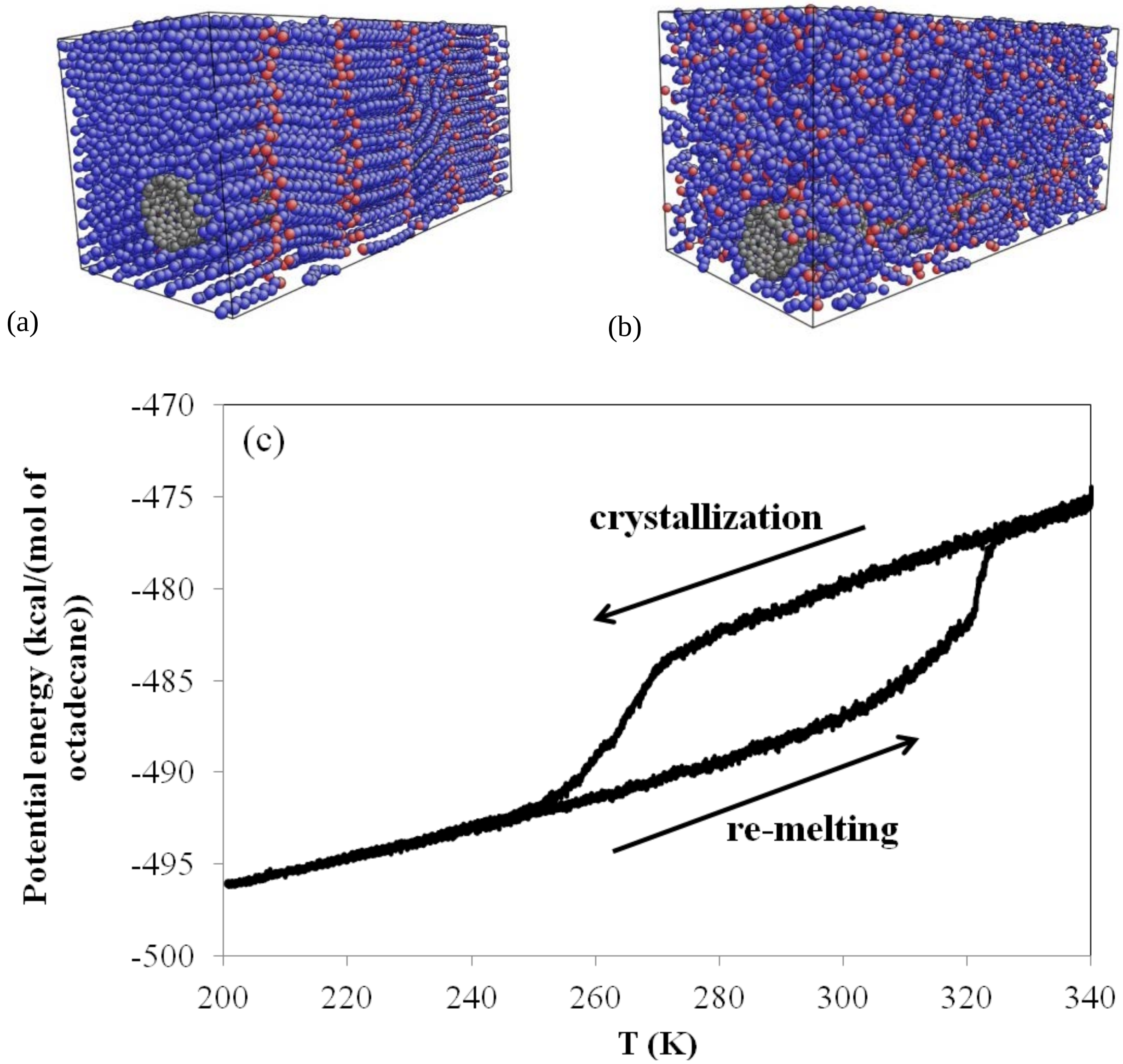

Figure 4.4 Snapshots of the (a) solid and (b) liquid CNT mixtures. The potential energy curve (c) for crystallization and re-melting processes for n-octadecane-CNT suspension.

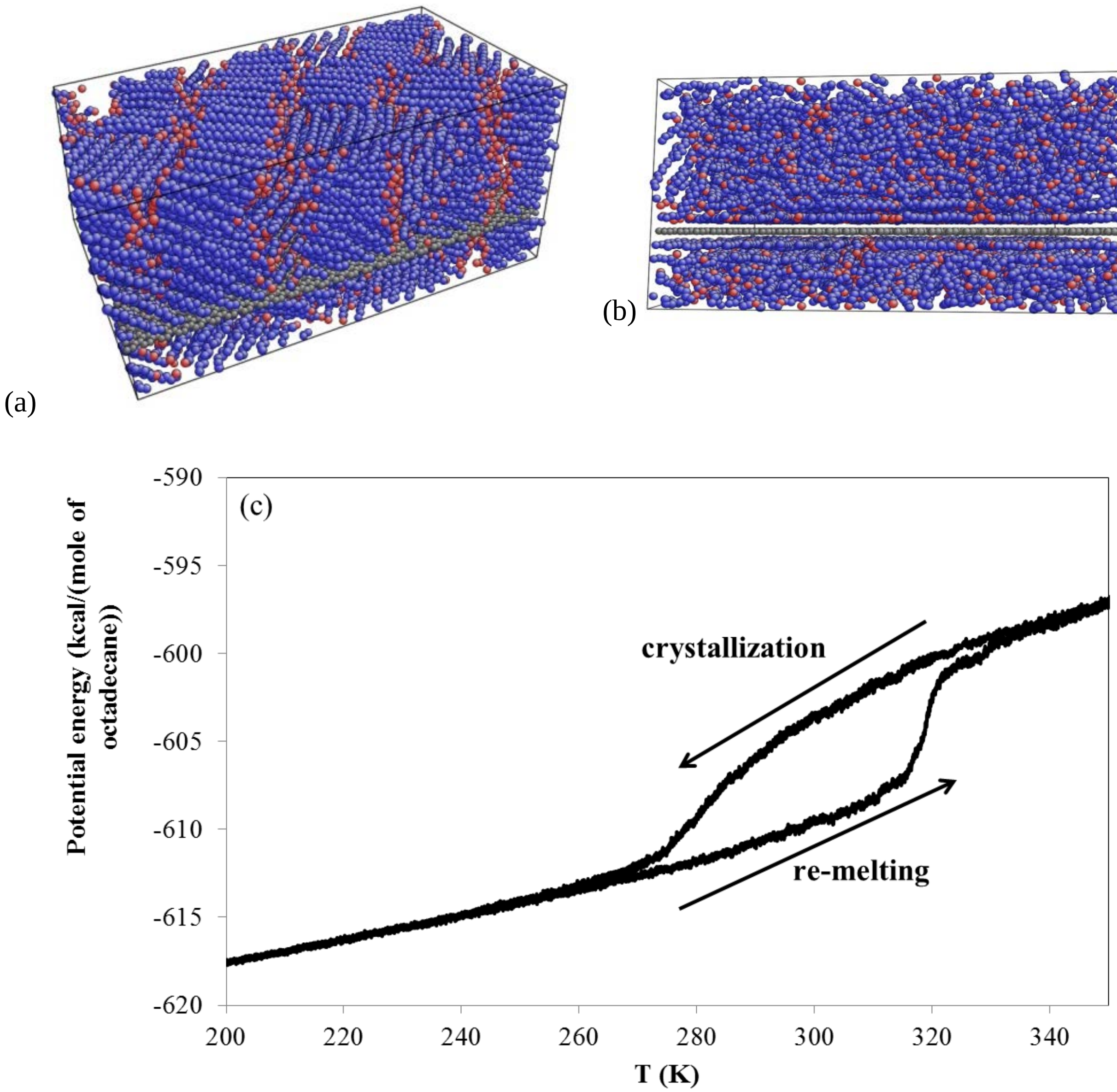

Figure 4.5 Snapshots of the (a) solid and (b) liquid graphene mixtures. The potential energy curve (c) for crystallization and re-melting processes for n-octadecane-graphene suspension.

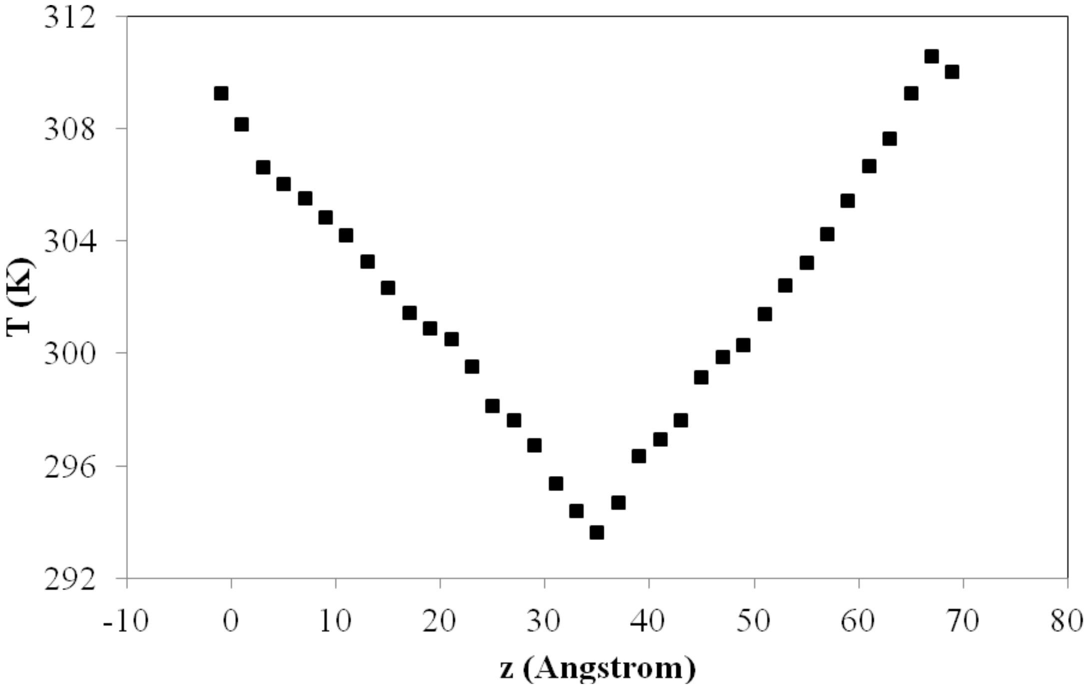

Figure 4.6 Temperature profiles for pure n-octadecane liquid phase at 300 K.

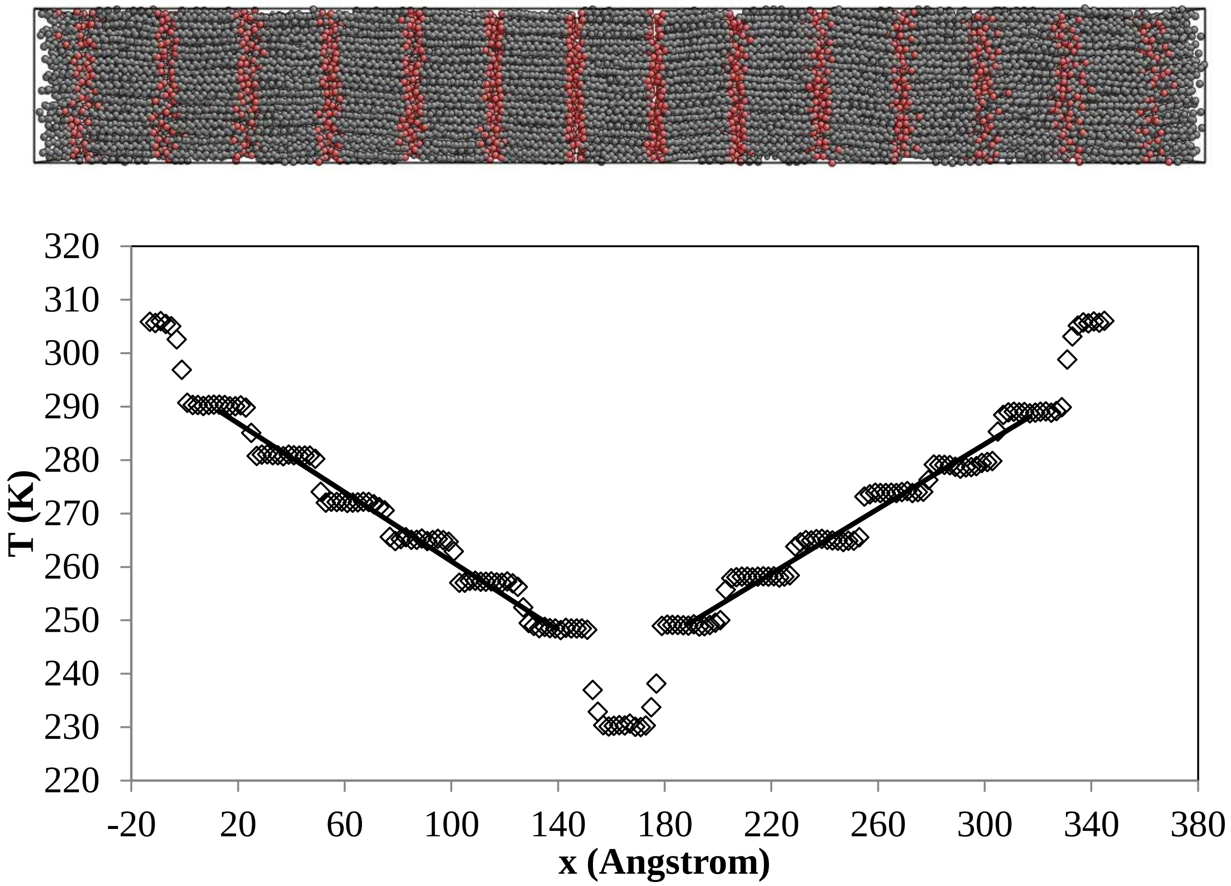

Figure 4.7 Temperature profile for thermal conductivity calculation along the direction of the molecular axis.

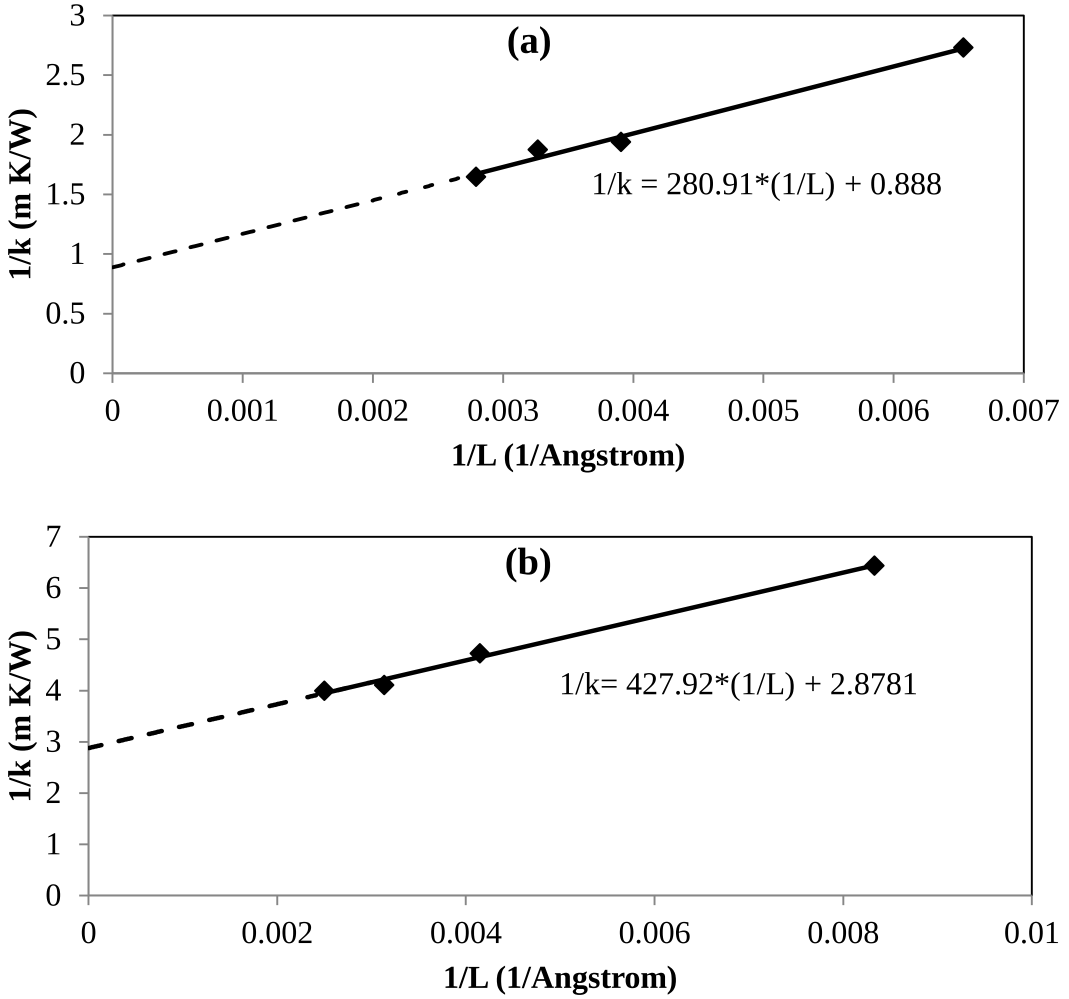

Figure 4.8 Inverse of the thermal conductivity as a function of the inverse of the length of the simulation cell for the perfect crystal at 270 K along the (a) *x*- and (b) *z*-directions.

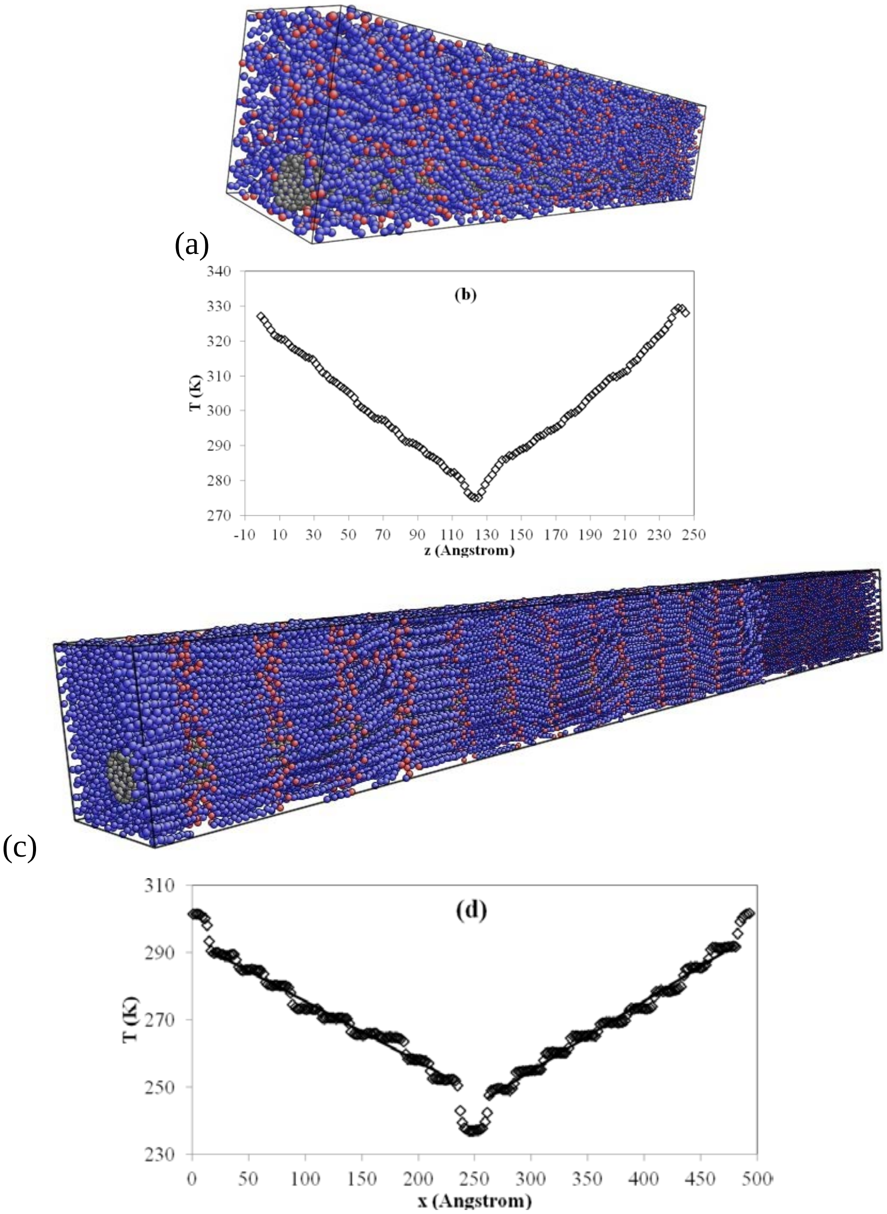

Figure 4.9 (a) Snapshot and (b) temperature profile for liquid n-octadecane-CNT suspension at 300 K and (c) Snapshot and (d) temperature profile for solid n-octadecane-CNT mixture at 270 K along the CNT axis.

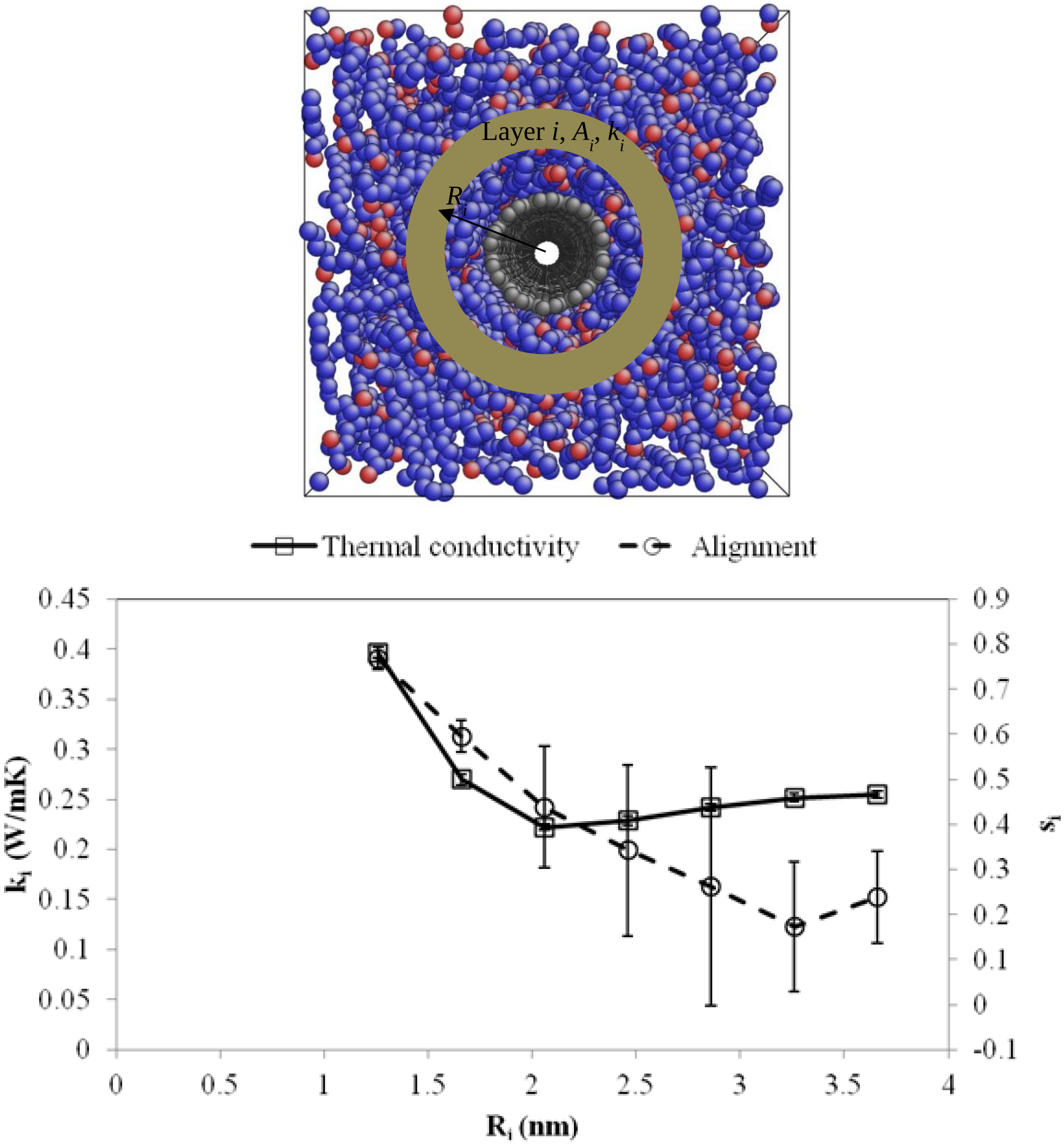

Figure 4.10 Local thermal conductivity and alignment parameter as functions of the distance from the CNT axis (CNT radius is equal to 0.7 nm).

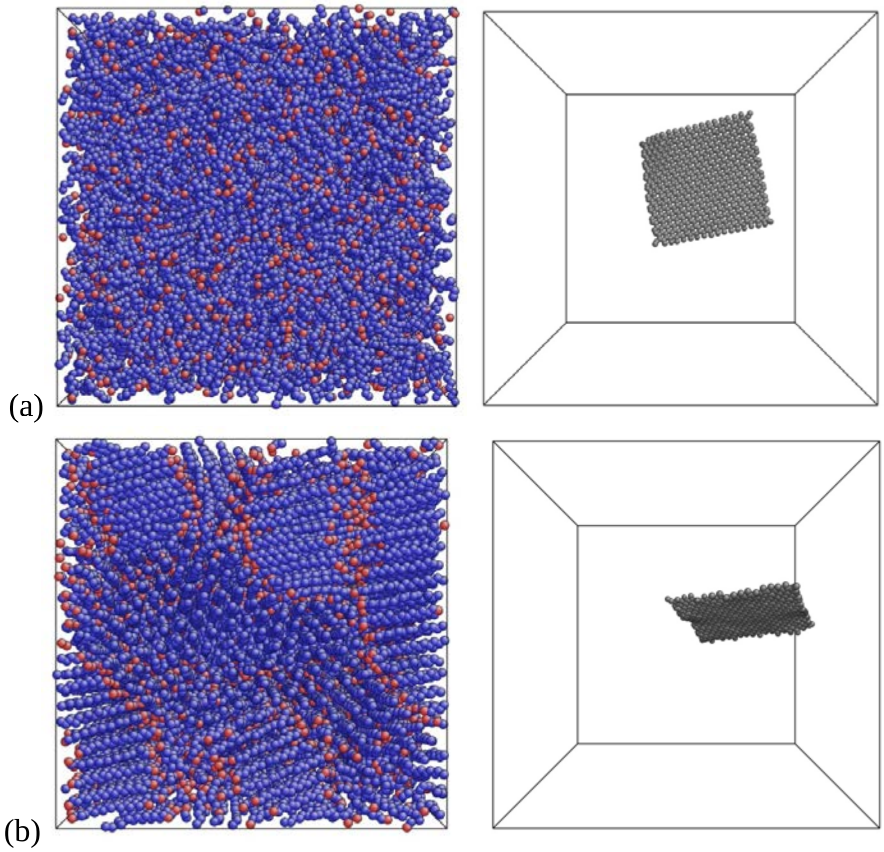

Figure 4.11 Snapshots of the (a) liquid and (b) solid phase graphene/octadecane mixtures.

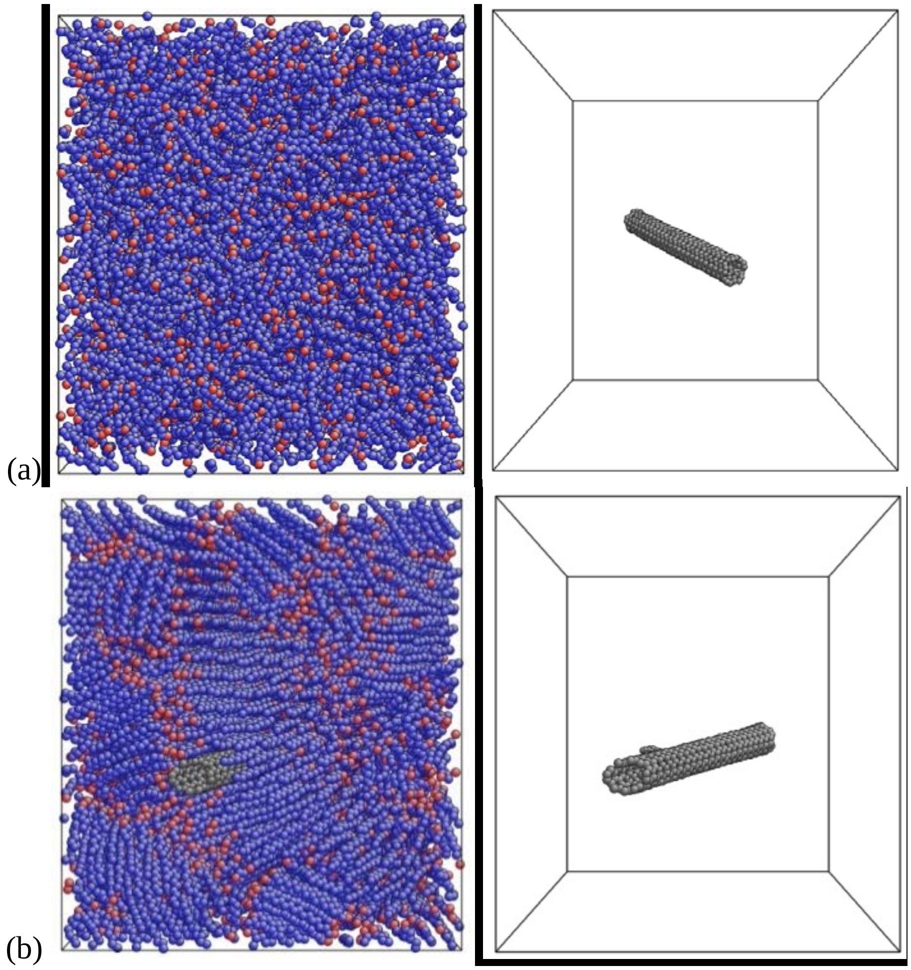

Figure 4.12 Snapshots of the (a) liquid and (b) solid phase CNT/octadecane mixtures.

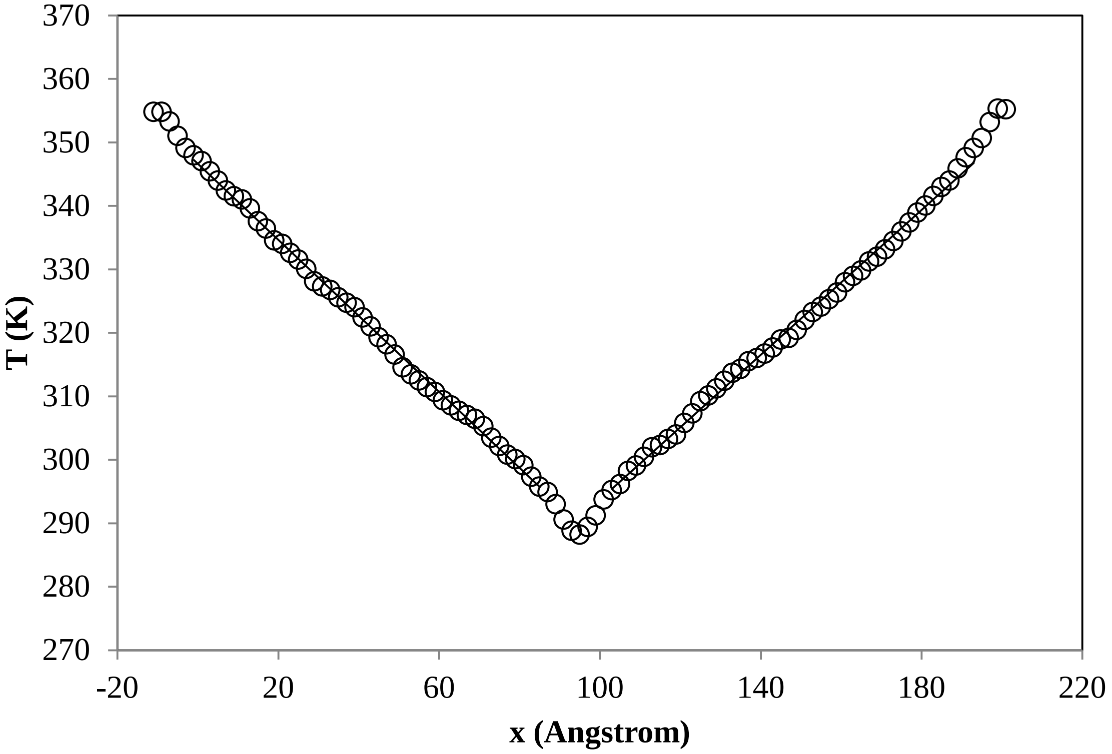

Figure 4.13 Temperature profile in the x-direction for the liquid graphene/octadecane mixture.

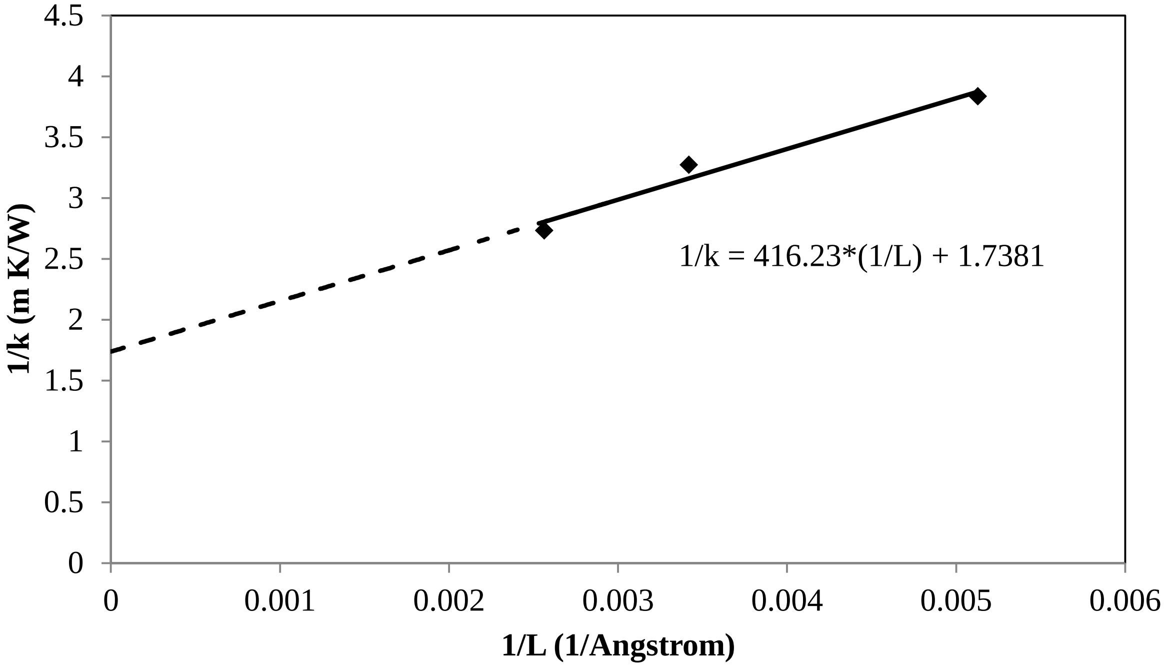

Figure 4.14 Inverse of the thermal conductivity in the x-direction versus the inverse of the length of the simulation cell for the 0.56 vol% solid graphene-octadecane mixture.

Chapter 5 Interfacial thermal conductance between graphene and paraffin

In this chapter, molecular dynamics simulations are utilized to study the interfacial thermal conductance between the graphene nanofillers and paraffin matrix. The effects of the paraffin phase and the thickness of the filler on the interfacial thermal conductance are investigated. The results indicate that the systems containing thin graphene layers exhibit higher values of the interfacial thermal conductance which for the liquid mixtures converges to 110 MW/m^2 K with increasing the thickness of the filler. In addition, due to existence of more structured layers of paraffin upon phase change, the interfacial conductance for the solid paraffin-graphene system is higher than the conductance of the corresponding liquid paraffin-graphene interface.

5.1 Introduction

In the context of thermal transport in graphene-paraffin mixtures, few researchers have tried to explain the underlying mechanisms associated with the thermal conductivity enhancement (Zheng et al., 2011 and Babaei et al., 2013). Zheng et al. (2011) related the improvement of thermal conductivity to the aggregation and percolation of particles creating paths for improved transfer of heat current. They speculated that upon freezing - due to a high internal stress - the interfacial thermal conductance between the fillers and matrix increases, thus leading to the observed higher enhancement in solid phase mixtures. In chapter 4, through using molecular dynamics (MD) simulations, it was demonstrated that ordering of the paraffin molecules brought about by the fillers increases the thermal conductivity of the matrix parallel to the axis of the CNT and plane of graphene. It was also observed that the enhancement of thermal conductivity is more marked for the solid phase matrix. However, the observed higher enhancement was related to the finding that upon freezing, matrix molecules become more ordered leading to more polarized phonon waves and improved thermal transport.

One of the key elements of thermal transport in mixtures is the interfacial thermal conductance between the filler and the matrix, also known as the Kapitza resistance (Kapitza, 1941). A low value of the interfacial thermal conductance can reduce thermal conductivity enhancement due to presence of the conductive fillers.

In this chapter, the values of the interfacial thermal conductance between graphene and paraffin are calculated by using the direct NEMD simulations. The results indicate that for the solid phase paraffin, the interfacial thermal conductance is higher than the value for the liquid phase. Moreover, the effect of the thickness of the graphene fillers on the interfacial thermal conductance is studied.

5.2 Literature Review

Two main theoretical models have been considered to date for the phonon-based interfacial thermal conductance. These are the acoustic mismatch model (AMM) and the diffuse mismatch model (DMM). In AMM, it is assumed that all the incident phonons from one side are transmitted to the other side of the interface by a transmission probability which depends on the phonon modes, frequency and wave vectors of bulk materials on both sides of the interface without depending on temperature (Swartz and Pohl, 1989). In DMM, the incident phonons are scattered and can propagate through any side of the interface based on a transmission probability that depends on the phonon density of states of both materials. The two models are similar except in the way the transmission coefficient is calculated. In both of the methods, the interfacial thermal conductance is based on the bulk properties of materials without accounting for the interfacial structure itself. Speaking qualitatively, depending on how similar the materials are, either AMM or DMM may dominate the interfacial thermal resistance. For more studies on the utilization of analytical and numerical approaches for determination of the thermal conductance based on these models, the reader can refer to Lumpkin et al. (1978), Swartz and Pohl (1987, 1989), Schelling et al. (2002), Wang et al. (2008) and Hu et al. (2010).

To date, both experimental and numerical tools have been used to provide insight into the interfacial thermal conductance, or the Kapitza resistance, for mixtures containing CNT/graphene fillers (Huxtable et al., 2003, Shenogin et al., 2004, Hu et al., 2011, and Hu et al., 2011). In the context of numerical determination of the thermal conductance, which is partially linked to the molecular structure and interactions between two neighboring materials at the interface (Obrien et al., 2012), molecular dynamics has shown the capability of being an appropriate tool to gain insight into the thermal transport at interfaces. Both equilibrium- (Barrat and Chiaruttini, 2003) and non-equilibrium-based methods (Shenogin et al., 2004, Hu et al., 2011, and Hu et al., 2011, and Barrat and Chiaruttini, 2003) have been established for MD determination of the interfacial thermal conductance. In the equilibrium method, a Green-Kubo-based formula is used to calculate the conductance through evaluating the autocorrelation function of the power crossing the interface. In this method, the transport property is related to the corresponding microscopic fluctuations at equilibrium, whereas in the non-equilibrium MD (NEMD) methods, either a transient or a steady-state temperature change is imposed in the system.

Huxtable et al. (2003) utilized both experimental and modeling tools to investigate the interfacial thermal conductance between CNT and matrices. By using the picosecond transient absorption technique, they obtained the interfacial thermal conductance for CNTs suspended in surfactant micelles in water experimentally. In the modeling approach, they used the NEMD-based transient method to evaluate the conductance between the CNT and octane molecules. They reported a very limited value of thermal conductance (~12 MW/m^2 K) obtained from both approaches.

Shenogin et al. (2004) used MD-based relaxation simulations to calculate the interfacial thermal conductance between the CNT and liquid octane. They obtained relatively high thermal conductance values which were dependent on the length of CNT. Their analysis on phonon mode-dependent temperature revealed that low-frequency vibration modes have the dominant contribution to the interfacial thermal conductance. For long CNTs where low-frequency modes exist, the thermal conductance is higher when compared to shorter CNTs.

Hu et al. (2011) used different NEMD-based methods and showed that the thermal relaxation method, which mimics transient heating experiments (Huxtable et al., 2003), underestimates the value of the thermal conductance at the interface of graphene and organic matrix. They also reported that utilization of the direct method with the heat source placed on graphene will result in lower thermal conductance, consistent with the relaxation method. They claimed that the internal thermal resistance associated with the cascade of energy within graphene from the high-frequency modes to the low-frequency modes (the modes that have the dominant contribution in the heat transfer across the interface) to be the reason behind the lower thermal conductance.

5.3 Methodology and Model Structures

For calculating the interfacial thermal conductance, we use the direct method in which the heat flux is perpendicular to the graphene's plane (Hu et al., 2011). In this method, the interfacial thermal conductance is the ratio of the heat flux to the temperature difference between the matrix and the filler at the interface. The relation reads as

$$G = \frac{q}{\Delta T} \tag{5.1}$$

where quantity G is the interfacial thermal conductance, q is the heat flux crossing the interface and ΔT is the temperature difference at the interface. In this study, since there are multiple interfaces, we take the average value of quantity ΔT over all interfaces.

To study the effect of the number of sheets of graphene on the value of the interfacial thermal conductance, we consider graphenes containing 1 and 3 layers and graphite flakes containing 9, 20 and 30 layers of graphene. Each layer of graphene has a cross-sectional area of ~70×70 Å^2 and contains 1856 carbon atoms. For the systems containing 1, 3 and 9 layers, the graphene sheets were immersed within 1000 molecules of octadecane (500 molecules each side), whereas for the systems with 20 and 30 graphene layers, the graphite flakes were initially located adjacent to 900 octadecane molecules.

The Nath, Escobedo, and de Pablo revised (NERD) force field (Nath et al., 1998) was used among octadecane molecules. This potential takes into account bond stretching, angle bending, dihedral torsion and pairwise Lennard-Jones (LJ) interactions. For in-plane interactions among graphene carbon atoms, the Tersoff potential (Tersoff, 1988) in combination with the Lindsay and Broido modification (Lindsay and Broido, 2010) was used. The LJ potential was used for the interlayer interactions between carbon atoms in different layers of graphene (Alen and Tildesley, 1989). For the cross-potential interaction between carbon atoms in the graphene and interaction sites of n-octadecane, the Lorentz-Berthelot mixing rule (Stuart et al., 2000) was used for determining the LJ potential parameters. While the Lorentz-Berthelot mixing rule is a well-known method for obtaining the weak van der Waals interaction for dissimilar atoms when the van der Waals interactions between individual atoms are known, it should be noted that altering this cross potential interaction can affect the value of interfacial thermal conductance. Therefore, there is potentially an approximation in the calculated interfacial thermal conductance due to the use of a special form of cross-interaction. Periodic boundary conditions were used in all directions. The velocity Verlet algorithm was used to integrate the Newton's equation of motion numerically with a time step of 0.5 fs. All simulations were performed with the large-scale atomic/molecular massively parallel simulator (LAMMPS) molecular dynamics package (Plimpton, 1995).

The liquid systems were obtained by equilibrating at 320 K and 1 atm under isothermal-isobaric ensemble (NPT). For the 1-, 3- and 9-layer systems, the solid mixtures were obtained by cooling systems to 250 K at the rate of 4 K/ns and heating to 280 K at the rate of 12 K/ns. The solidification process is explained in detail in chapter 4. For the 20- and 30-layer systems, due to excessive time needed for simulations, realizations of solid structures were not attempted.

For the 1-, 3- and 9-layer graphene mixtures, similar procedures were utilized to calculate the values of the thermal conductance. For each case, the system was first duplicated along the graphene's out-of-plane direction (*z*-direction in Figure 5.1 (a) that shows a 3-layer system), thus introducing a pair of 3-layer graphene systems in the simulation cell. Then, the systems were equilibrated under canonical dynamics (NVT) and then under microcanonical dynamics (NVE). Upon equilibration, a heat flux was imposed in the graphene's out-of-plane (*z*) direction by adding/extracting heat to the source/sink slabs that were located in the middle of paraffin regions. Upon reaching the steady-state condition, the temperature profiles were obtained by averaging the temperatures for 2,000,000 time steps. The temperature profiles for the liquid and solid 3-layer graphene-octadecane mixtures are shown in Figures 5.1 and 5.2, respectively. For the 9-layer graphene-octadecane mixtures, the temperature profiles for the liquid and solid phases are shown in Figures 5.3 and 5.4, respectively. Common among these figures, distinct temperature drops are observed for the temperature profiles due to the interfacial thermal resistance. Since there are four interfaces throughout these shown simulation boxes, the values of the thermal conductance are calculated based on the average of the temperature differences over these four interfaces.

For the 20- and 30-layer cases, a heat flux was imposed through the simulation box by adding heat into a few layers within the graphite flake and extracting heat from a slab located in the middle of the octadecane region. The snapshots and temperature profiles for the 20- and 30-layer cases are shown in Figures 5.5 and 5.6, respectively. Similar to the thin graphene cases, the noticeable temperature drops at the paraffin-graphene interfaces are indicative of the interface thermal resistance. In these cases, the values of the thermal conductance are determined by considering the average temperature difference over the two existing interfaces.

5.4 Results and Discussion

The calculated values of the thermal conductance for the systems considered here are given in Table 5.1. For the 1-, 3- and 9-layer cases, the stated errors are calculated based on the different thermal conductance values obtained for interfaces of two graphene sheets, whereas for the 20- and 30-layer cases, the errors are calculated based on the different values of the interfacial thermal conductance at two interfaces corresponding to two sides of the filler. The values of the interfacial thermal conductance for the solid paraffin-graphene interfaces are higher than the corresponding ones for liquid mixtures. This is attributed to the existence of more structured interfacial layers of octadecane when it is in solid phase. Upon phase change, planar structures of octadecane are formed parallel to the surface of graphene (see also chapter 4). Such distinct planar structures of octadecane next to the interfaces of the solid and liquid mixtures are shown in Figure 5.7.

Another influencing attribute to the interfacial thermal conductance is the thickness of the graphene sheet. Nanoscopic and macroscopic fillers can potentially exhibit different range of values of the interfacial thermal conductance. To study the effect of the thickness of the nano-filler on the thermal conductance, we considered graphene and graphite flakes with different numbers of layers. The computed values of the thermal conductance indicate that a higher number of graphene layers consistently leads to a lower value of thermal conductance for both liquid and solid phase paraffin. For the liquid systems, by increasing the number of layers, the interfacial thermal conductance converges to ~110 MW/m^2 K. This behavior is clearly observed in Figure 5.8. The higher values of the interfacial thermal conductance for the cases of layers with a smaller number of graphene sheets indicate that the interfacial thermal conductance values for nanoscopic level structures are higher than the conductance values for macroscopic structures. This phenomenon may be intuitively explained by the reasoning that the out-of-plane vibrational behavior of carbon atoms within a graphene structure composed of a few layers is correlated more strongly with the vibrational behavior of octadecane molecules rather than exhibiting independent vibrational motion of carbon atoms in bulk graphite.

5.5 Summary and Conclusions

In this chapter, the interfacial thermal conductance, a principal factor in thermal transport within multicomponent systems, was investigated for the solid and liquid mixtures of paraffin and graphene. Graphene sheets and graphite flakes having different numbers of layers were considered. The results for all cases with various numbers of graphene layers indicated that the values of the interfacial thermal conductance for solid mixtures are higher than the corresponding values for liquid mixtures. For solid or liquid mixtures, the predictions indicated that graphene sheets with a lower number of layers (thinner graphenes) exhibit higher values of the interfacial thermal conductance. For the liquid systems, by increasing the number of layers, the interfacial thermal conductance converges to a value around 110 MW/m^2 K.

Table 5.1 Predicted values of the interfacial thermal conductance for systems with different number of graphene layers.

Number of layers	Phase	Thermal conductance (MW/m^2 K)
1	Liquid	198±13
	Solid	288±4
3	Liquid	187±19
	Solid	254±55
9	Liquid	146±13
	Solid	198±30
20	Liquid	110±11
30	Liquid	111±12

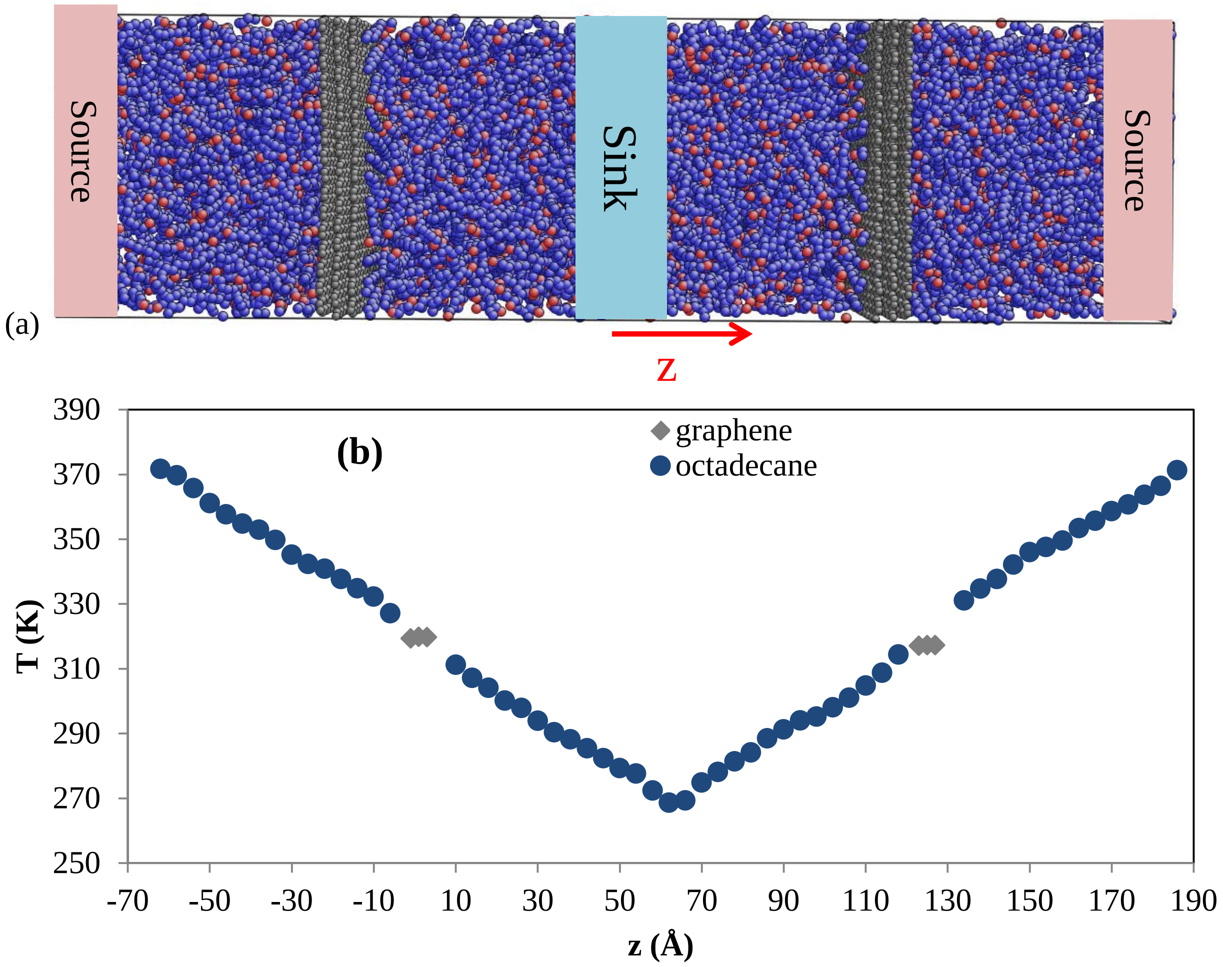

Figure 5.1 (a) The snapshot and (b) temperature profile of the liquid 3-layer graphene-octadecane mixture.

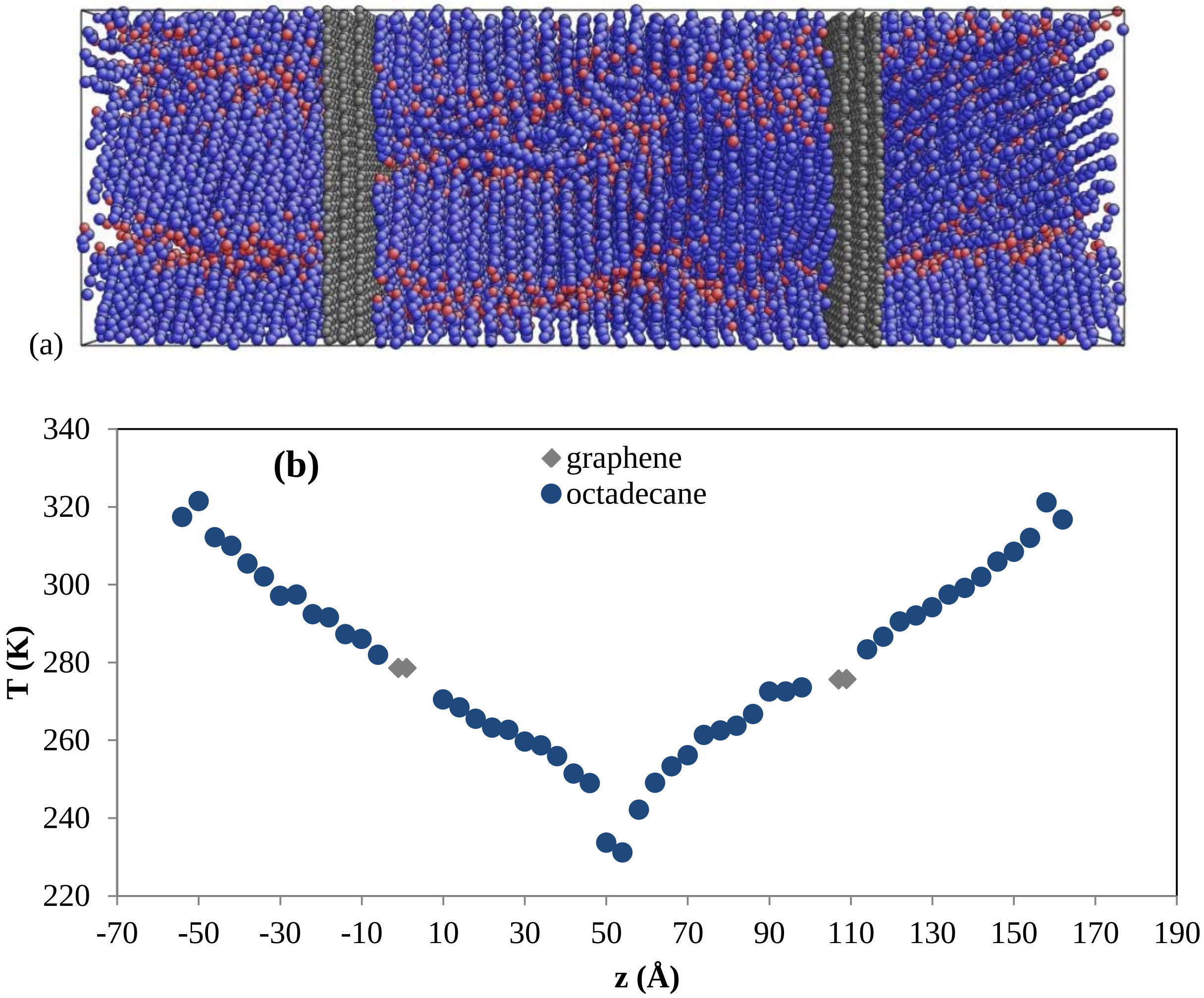

Figure 5.2 (a) The snapshot and (b) temperature profile of the solid 3-layer graphene-octadecane mixture.

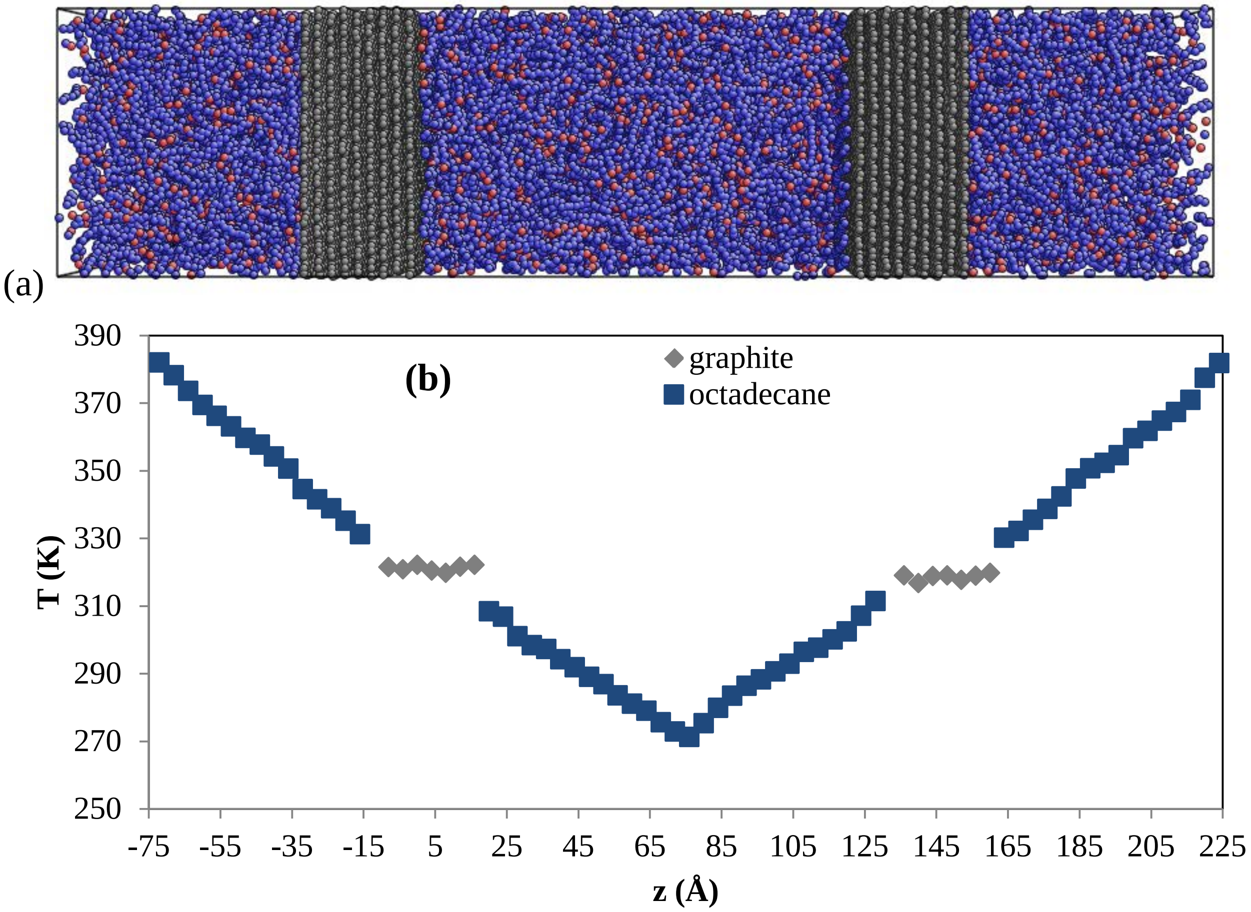

Figure 5.3 (a) The snapshot and (b) temperature profile of the liquid 9-layer graphene-octadecane mixture.

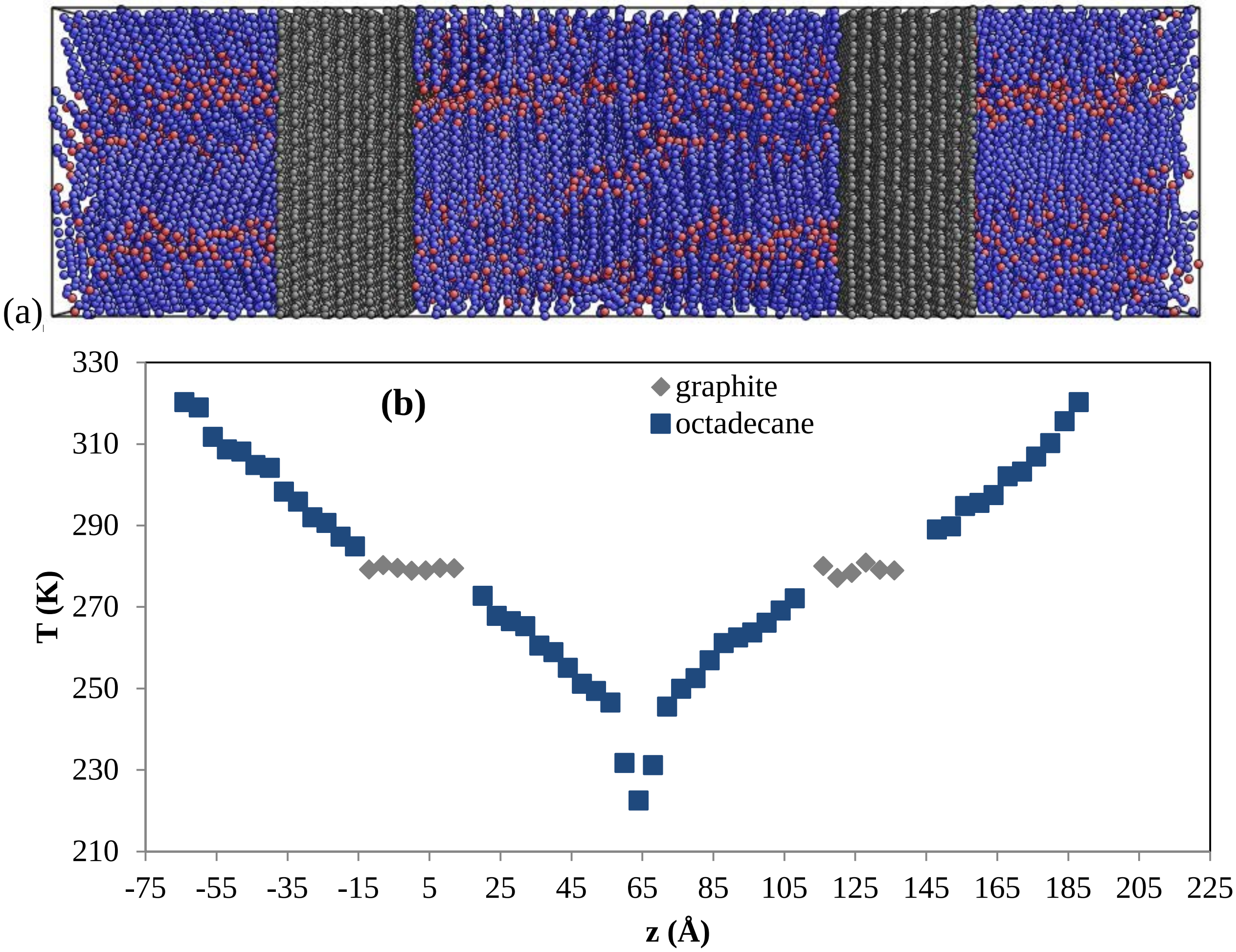

Figure 5.4 (a) The snapshot and (b) temperature profile of the solid 9-layer graphene-octadecane mixture.

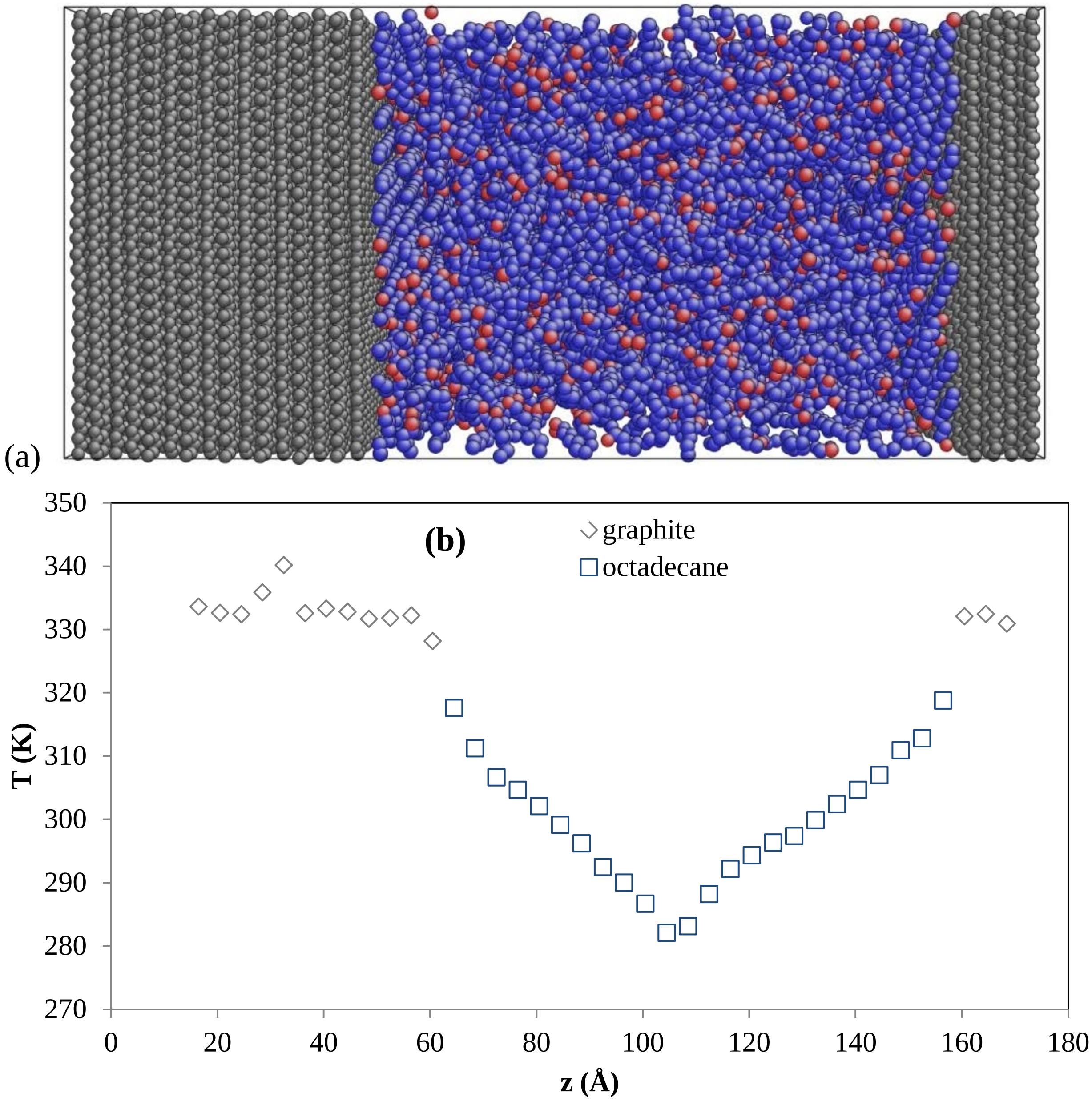

Figure 5.5 (a) The snapshot and (b) temperature profile of the liquid 20-layer graphene-octadecane mixture.

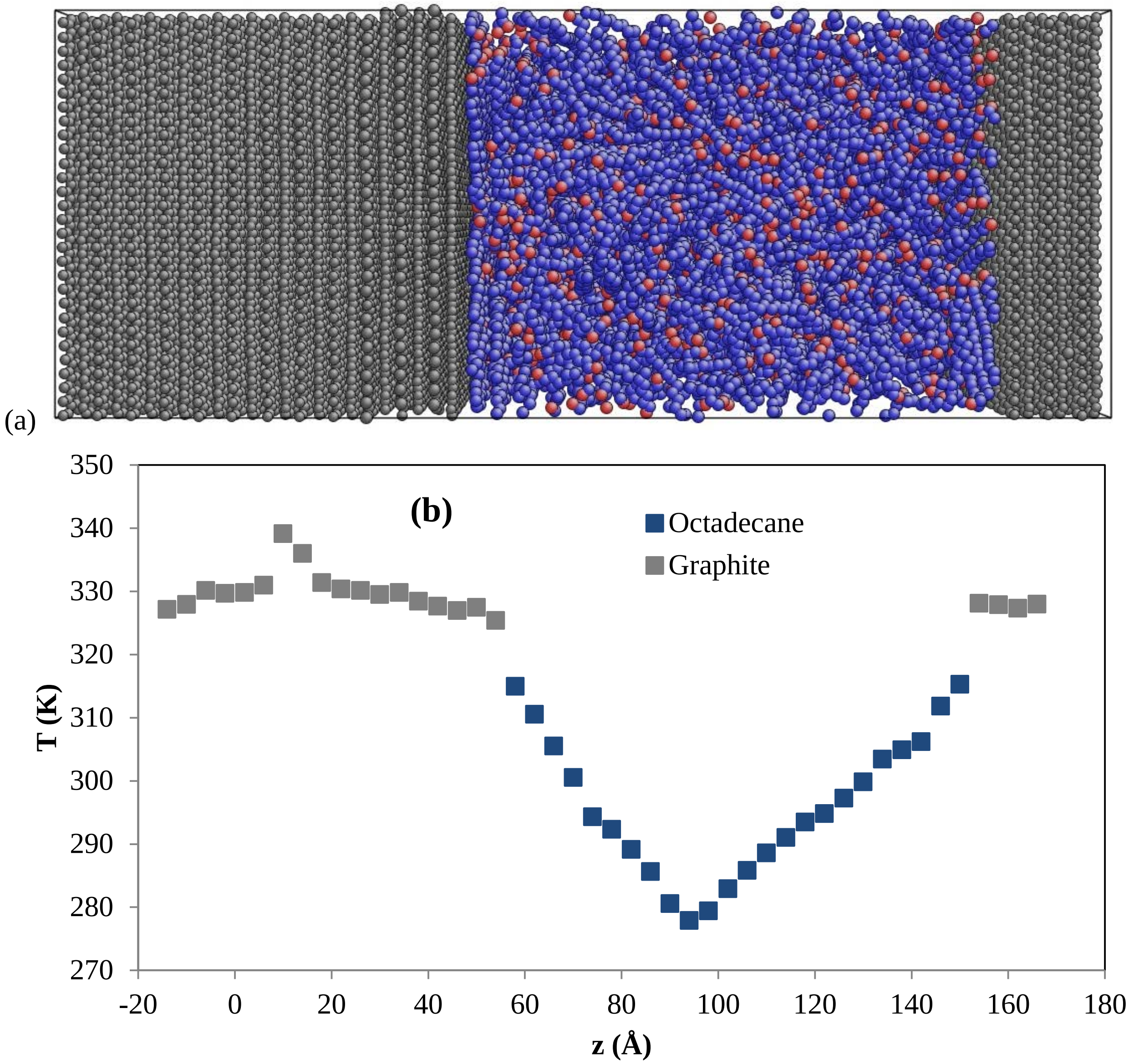

Figure 5.6 (a) The snapshot and (b) temperature profile of the liquid 30-layer graphene-octadecane mixture.

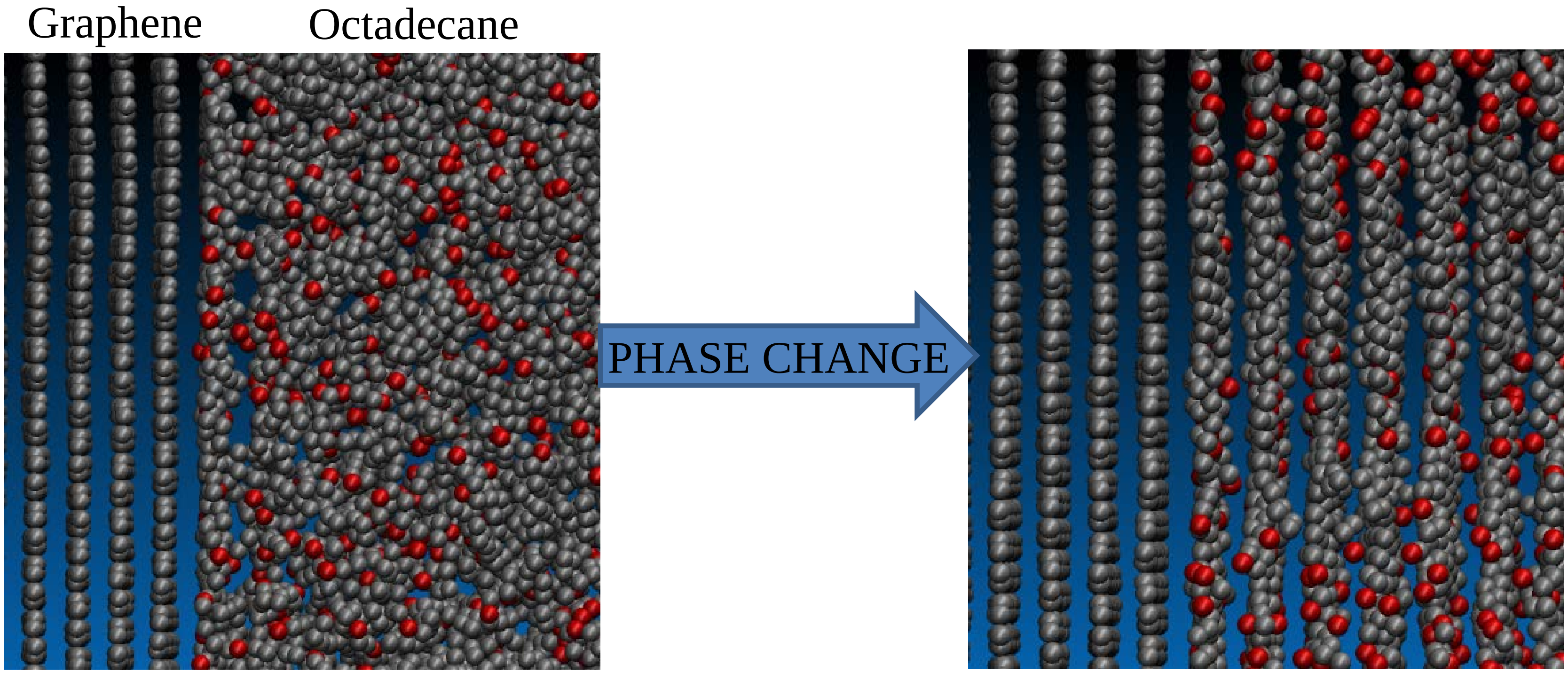

Figure 5.7 Close-up snapshots of the interface for the liquid (left) and solid (right) mixtures.

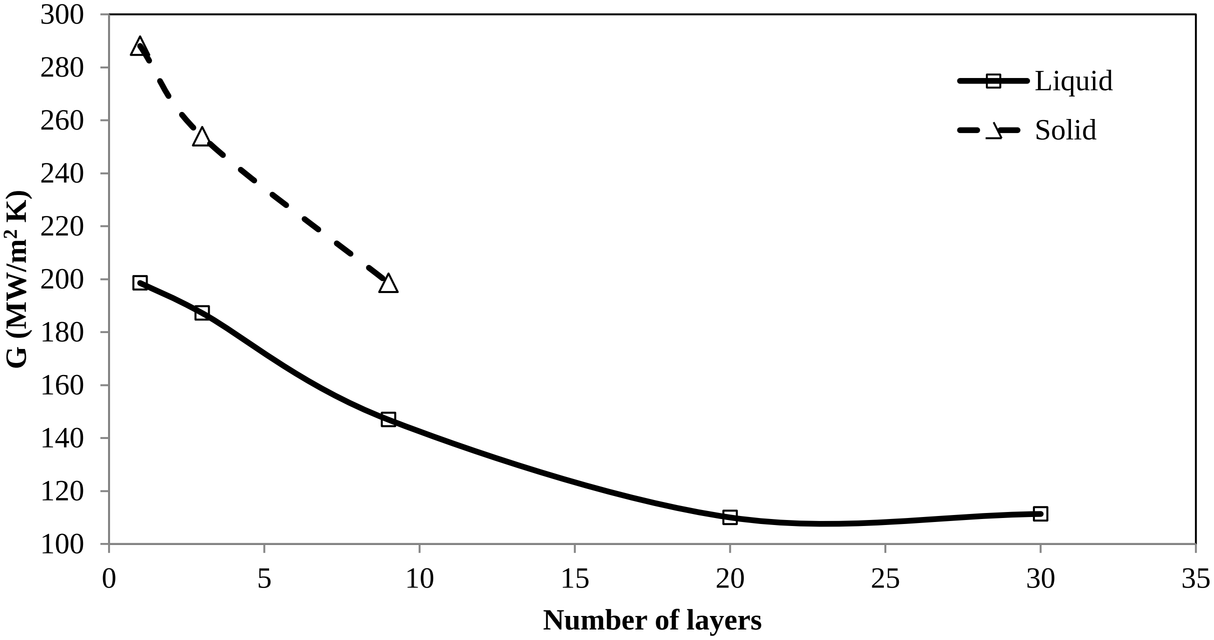

Figure 5.8 Dependence of the interfacial thermal conductance on the number of layers of graphene.

Chapter 6 Conclusions and future research directions

In this chapter, the concluding remarks of this dissertation and some suggestions for future research are presented in sections 6.1 and 6.2, respectively.

6.1 Conclusions

In this dissertation, thermal transport in nanostructure-enhanced phase change materials was investigated by using molecular level simulations.

- *Thermal conductivity of nanofluids*

Firstly, in relation to improvement in thermal conductivity of spherical nanoparticle suspensions, a precise definition for heat current utilized in the Green-Kubo method for multicomponent systems is determined. The key component in heat current expression was the kinetic term involved in the partial enthalpy which has been overlooked in some previous works resulting in erroneous reported high enhancements in thermal conductivity of nanofluids. In order to validate the heat current expression, extensive simulations were carried out on different multicomponent systems including a nanofluid system and mixture systems in gas, liquid and solid phases. The consistent results from the Green-Kubo and the non-equilibrium direct methods corroborate the correctness of the heat flux expression. For nanofluids at different temperatures and volume fractions, the thermal conductivity improvements are in agreement with the Maxwell's model predictions for well-dispersed nanofluids and no additional enhancement was observed. By decomposing the resulting thermal conductivity values, the effect of the Brownian motion-induced micro-convection was studied. It is found that while the convection-based potential and enthalpy components in thermal conductivity are considerably high, these terms cancel each other leaving an insignificant contribution to the overall thermal conductivity.

- *Improvement in thermal conductivity of paraffin by adding high aspect-ratio carbon-based nano-fillers*

Regarding carbon-based high aspect-ratio nano-fillers, e.g. graphene and carbon nanotubes, the effect of such nanoparticles on thermal conductivity of liquid and solid paraffin was investigated. Introduction of CNT and graphene nanofillers leads to considerable ordering of paraffin molecules and associated thermal conductivity enhancement. More notably, carbon nano-fillers provide a template for directed crystallization and lead to even greater thermal conductivity increases in solid phase mixtures. The results indicate that introducing carbon nanotubes and graphene into long-chain paraffins leads to a considerable improvement in thermal conductivity, not only due to the presence of a conductive filler, but also due to the filler-induced alignment of paraffin molecules. The dependency of thermal conductivity of paraffin on the alignment factor for its molecules suggests that there is a strong relationship between thermal conductivity and the alignment factor. Thermal conductivity of liquid paraffin which has the lowest alignment factor (0.02) due to the random distribution of molecules is the minimum, whereas the thermal conductivity of perfect crystal which has the highest alignment factor (0.99) is the maximum value. Comparing the predicted thermal conductivity values based on two sets of simulations, in one set, considering the full dynamics of carbon atoms in graphene/CNT and in another one, freezing the atomic motions for graphene/CNT atoms, showed that the main mechanism for thermal conductivity improvement in such mixtures is the nanofiller-induced ordering in paraffin molecules.

- *Interfacial thermal conductance between graphene and paraffin*

The interfacial thermal conductance between graphene nanofiller and paraffin matrix was also studied. The effect of the paraffin phase and the filler's thickness on the interfacial thermal conductance was investigated. The results indicated that the systems containing thin graphene layers exhibit higher interfacial thermal conductance which for liquid mixtures converges to 110 MW/m^2 K with increasing filler thickness. The other finding was that the interfacial conductance for solid paraffin-graphene is higher than the conductance of the corresponding liquid paraffin-graphene interface.

6.2 Future research directions

The new findings in this dissertation open the door for more ideas concerning improving thermal transport of not only PCM but also other applications. Some possible immediate future research projects are listed below:

- Effect of the length of molecules on the ordering-induced improvement in thermal conductivity of paraffins. Based on findings associated with perfect crystal discussed in chapter 4, it is expected that increasing the length of molecules reduces the density of interfaces between layers, which has the key role in increasing the resistance to thermal transport.
- Relevant to the latter topic, investigating the effect of the length of molecules on the interfacial thermal conductance between those layers forming in perfect crystals would be of interest. The interfacial thermal conductance between the layers is directly

influential on the thermal conductivity of perfect crystals of long chain molecules. The perspective research can also shed light on more fundamental concepts related to the dependency of the interfacial thermal conductance on the phonon modes present in neighboring materials at the interface.

- Effects of surfactants on (1) thermal conductance between CNT/graphene and the matrix and (2) alignment of matrix molecules. Recent studies (Losego and Cahill, 2013, Losego et al., 2012, Ong et al., 2013, Lin and Buehler, 2013, and Acharya et al., 2011) have reported strong correlation between chemistry of interfaces, strength of interaction between materials at the interface and functionalization of the fillers on the interfacial thermal conductance.
- The effect of the number of layers forming nanofillers on the overall thermal conductivity of the mixtures containing CNT/graphene is another topic that must be investigated. In chapter 5, it is pointed out that graphene with a smaller number of layers exhibit higher interfacial thermal conductance. However, other thickness-related factors can influence the overall thermal conductivity such as the capability of ordering base material and the aspect-ratio of nanoparticles in a given volume fraction with various thicknesses. It would have important application to discuss the capability of graphene sheets having different thicknesses in enhancing the overall thermal conductivity of a mixture.
- Relevant to discussions given in chapter 5, for validating the suggested reasoning behind the observed dependency of the interfacial thermal conductance on the phase of paraffin and thickness of graphene, it is suggested to investigate the mode-dependent

phonon-based thermal conductance across such interfaces by using the Green's function method.

Finally, based on the observed strong molecular alignment-thermal conductivity relation for paraffin, utilization of nanoparticles with high aspect ratio is recommended to manufacturers as far as the particles do not bend. Also, for applications where directional high thermal conductivity is needed, it is suggested to use external forces such as a strong magnetic field and the anisotropic properties of the nanofillers to align the particles in the desired direction.

Bibliography

Acharya, H., Mozdzierz, N. J., Keblinski, P., Garde, S., 2011, “How chemistry, nanoscale roughness, and the direction of heat flow affect thermal conductance of solid–water interfaces,” *Industrial and Engineering Chemistry Research*, **51**(4), pp. 1767-1773.

Allen, M. P., Tildesley, D. J., 1989, “*Computer simulation of liquids*,” Oxford University Press, New York.

Andersen, H. C., 1980, “Molecular dynamics simulations at constant pressure and/or temperature,” *The Journal of Chemical Physics*, **72**(4), pp. 2384-2393.

Babaei, H., Keblinski, P., Khodadadi, J. M., 2013, “Thermal conductivity enhancement of paraffins by increasing the alignment of molecules through adding CNT/graphene,” *International Journal of Heat and Mass Transfer*, **58**(1-2), pp. 209-216.

Barrat, J.-L., Chiaruttini, F., 2003, “Kapitza resistance at the liquid-solid interface,” *Molecular Physics*, **101**(11), pp. 1605–1610.

Batchelor, G. K., 1974, “Transport properties of two-phase materials with random structure,” *Annual Review of Fluid Mechanics*, **6**, pp. 227-255.

Bearman, R. J., Kirkwood, J. G., 1958, “Statistical mechanics of transport processes. XI. Equations of transport in multicomponent systems,” *The Journal of Chemical Physics*, **28**(1), 136-145.

Bruggeman, D. A. G., 1935, "Calculation of different physical constants of heterogeneous substances: I. Dielectric constant and conductivity of media of isotropic substances," *Ann. Phys. (Leipzig)*, **24**, pp. 636-664.

Bunn, C. W., 1939, "The crystal structure of long-chain normal paraffin hydrocarbons. The "shape" of the < CH_2 group," *Transactions of the Faraday Society*, **35**, pp. 482-491.

Buongiorno, J., Venerus, D. C., Prabhat, N., McKrell, T., Townsend, J., Christianson, R., Tolmachev, Y. V., Keblinski, P., Hu, L.-W., Alvarado, J. L., Bang, I. C., Bishnoi, S. W., Bonetti, M., Botz, F., Cecere, A., Chang, Y., Chen, G., Chen, H., Chung, S. J., Chyu, M. K., Das, S. K., Paola, R. D., Ding, Y., Dubois, F., Dzido, G., Eapen, J., Escher, W., Funfschilling, D., Galand, Q., Gao, J., Gharagozloo, P. E., Goodson, K. E., Gutierrez, J. G., Hong, H., Horton, M., Hwang, K. S., Iorio, C. S., Jang, S. P., Jarzebski, A. B., Jiang, Y., Jin, L., Kabelac, S., Kamath, A., Kedzierski, M. A., Kieng, L. G., Kim, C., Kim, J.-H., Kim, S., Lee, S. H., Leong, K. C., Manna, I., Michel, B., Ni, R., Patel, H. E., Philip, J., Poulikakos, D., Reynaud, C., Savino, R., Singh, P. K., Song, P., Sundararajan, T., Timofeeva, E., Tritcak, T., Turanov, A. N., Vaerenbergh, S. V., Wen, D., Witharana, S., Yang, C., Yeh, W.-H., Zhao, X.-Z., Zhou, S.-Q., 2009, "A benchmark study on the thermal conductivity of nanofluids," *Journal of Applied Physics*, 106(9), 094312-094312.

Cahill, D. G., Ford, W. K., Goodson, Mahan, G. D., Majumdar, A., Maris, H. J., Merlin, R., Phillpot, S. R., 2003, "Nanoscale Thermal Transport," *Journal of Applied Physics*, **93**(2), pp. 793-818.

Carson, J. K., Lovatt, S. J., Tanner, D. J., Cleland, A. C., 2005, "Thermal conductivity bounds for isotropic porous materials," *International Journal of Heat and Mass Transfer*, **48**(11), pp. 2150–2158.

Choi, S. U. S., 1995, “Enhancing thermal conductivity of fluids with nanoparticles, in: Developments and Application of Non-Newtonian Flows,” *ASME*, FED-Vol. **231**/MD-Vol. **66**, pp. 99–105.

Chon, C. H., Kihm, K. D., Lee, S. P., Choi, S. U. S., 2005, “Empirical correlation finding the role of temperature and particle size for nanofluid (Al_2O_3) thermal conductivity enhancement,” *Applied Physics Letters*, **87**(15), pp. 153107–1–3.

Cui, Y., Liu, C., Hu, S., Yu, X., 2011, “The experimental exploration of carbon nanofiber and carbon nanotube additives on thermal behavior of phase change materials,” *Solar Energy Materials and Solar Cells*, **95**(4), pp. 1208-1212.

Das, S., Putra, N., Thiesen, P., Roetzel, W., 2003, “Temperature dependence of thermal conductivity enhancement for nanofluids,” *Journal of Heat Transfer*, **125**, pp. 567-574.

Daw, M. S., Baskes, M. I., 1984, “Embedded-atom method: Derivation and application to impurities, surfaces, and other defects in metals,” *Physical Review B*, **29**(12), pp. 6443–6453.

Eapen, J., Li, J., Yip, S., 2007, “Beyond the Maxwell limit: thermal conduction in nanofluids with percolating fluid structures,” *Physical Review E*, **76**, 062501.

Eapen J., Li, J., Yip, S., 2007, “Mechanism of thermal transport in dilute nanocolloids,” *Physical Review Letters*, **98**(2), 028302.

Eapen, J., Rusconi, R., Piazza, R., Yip, S., 2010, “The classical nature of thermal conduction in nanofluids,” *Journal of Heat Transfer*, **132**(10), 102402.

Eastman, J. A., Choi, U. S., Li, S., Yu, W., Thompson, L. J., 2001, ‘‘Anomalously increased effective thermal conductivities of ethylene glycol-based nanofluids containing copper nanoparticles,’’ *Applied Physics Letters*, **78**(6), pp. 718-720.

Elgafy, A., Lafdi, K., 2005, “Effect of carbon nanofiber additives on thermal behavior of phase change materials,” *Carbon*, **43**(15), pp. 3067–3074.

Esselink, K., Hilbers, P. A. J., Van Beest, B. W. H., 1994, “Molecular dynamics study of nucleation and melting of n-alkanes,” *The Journal of Chemical Physics*, **101**, 9033.

Evans, W., Fish, J., Keblinski, P., 2006, “Role of Brownian motion hydrodynamics on nanofluid thermal conductivity,” *Applied Physics Letters*, **88**(9), 93116.

Gao, J. W., Zheng, R. T., Ohtani, H., Zhu, D. S., Chen, G., 2009, “Experimental investigation of heat conduction mechanisms in nanofluids. Clue on clustering,” *Nano Letters*, **9**(12), pp. 4128-4132.

Gharagozloo, P. E., Eaton, J. K., Goodson, K. E., 2008, “Diffusion, aggregation, and the thermal conductivity of nanofluids,” *Applied Physics Letters*, **93**(10), 103110.

Gharagozloo, P. E., Goodson, K. E., (2010), “Aggregate fractal dimensions and thermal conduction in nanofluids,” *Journal of Applied Physics*, **108**(7), pp. 074309-074309.

Gülseren, I., Coupland, J. N., 2007, “Excess ultrasonic attenuation due to solid-solid and solid-liquid transitions in emulsified octadecane,” *Crystal Growth and Design*, **7**(5), pp. 912-918.

Halicioglu, T., Pound, G. M., 1975, “Calculation of potential-energy parameters from crystalline state properties,” *Physica Status Solidi (a)*, **30**(2), pp. 619-623.

Hamilton, R. L., Crosser, O. K., 1962, “Thermal conductivity of heterogeneous two-component systems,” *Industrial and Engineering Chemistry Fundamentals*, **1**(3), pp. 187-191.

Hashin, Z., Shtrikman, S., 1962, “A variational approach to the theory of the effective magnetic permeability of multiphase materials,” *Journal of Applied Physics*, **33**(10), pp. 3125-3131.

Hasselman, D. P. H., and Johnson, L. F. J., 1987, “Effective Thermal Conductivity of Composites with Interfacial Thermal Barrier Resistance,” *Journal of Composite Materials*, **21**(6), pp. 508-515.

Himran, S., Suwono, A., Mansoori, G. A., 1994, “Characterization of alkanes and paraffin waxes for application as phase change energy storage medium,” *Energy Sources*, **16**(1), pp. 117-128.

Hu, L., Desai, T. G., Keblinski, P., 2011, “Determination of interfacial thermal resistance at the nanoscale,” *Physical Review B*, **83**(19), 195423.

Hu, L., Desai, T. G., Keblinski, P., 2011, “Thermal transport in graphene-based nanocomposite,” *Journal of Applied Physics*, **110**(3), 033517.

Hu, L., Zhang, L., Hu, M., Wang, J.-S., Li, B., Keblinski, P., 2010, “Phonon interference at self-assembled monolayer interfaces: Molecular dynamics simulations,” *Physical Review B*, **81**(23), pp. 1–5.

Huxtable, S., Cahill, D., Shenogin, S., Xu, L., Ozisik, R., Barone, P., Usrey, M., Strano, M., Siddons, G., Shim, M., Keblinski, P., 2003, “Interfacial heat flow in carbon nanotube suspensions,” *Nature Materials*, **2**, pp. 731–734.

Irving, J. H., Kirkwood, J. G., 1950, “The statistical mechanical theory of transport processes. IV. The equations of hydrodynamics,” *The Journal of Chemical Physics*, **18**, pp. 817-829.

Jang, S. P., Choi, S. U. S., 2004, “Role of Brownian motion in the enhanced thermal conductivity of nanofluids,” *Applied Physics Letters*, **84**(21), pp. 4316-4318.

Jorgensen, W. L., Madura, J. D., Swenson, C. J., Carol, J., 1984, “Optimized intermolecular potential functions for liquid hydrocarbons,” *Journal of American Chemical Society*, **106**(22), pp. 6638-6646.

Kang, H., Zhang, Y., Yang, M., 2011, “Molecular dynamics simulation of thermal conductivity of Cu–Ar nanofluid using EAM potential for Cu–Cu interactions,” *Applied Physics A*, **103**(4), pp. 1001–1008.

Kapitza, P. L. (1941), “The study of heat transfer in helium II,” *Zh. Eksp. Teor. Fiz.*, **11**, 1. [English translation: *Journal of Physics-USSR*, **4**, 181.]

Keblinski, P., Cahill, D. G., 2005, “Comment on “Model for Heat Conduction in Nanofluids”,” *Physical Review Letters*, **95**(20), 209401.

Keblinski, P., Phillpot, S. R. , Choi, S. U. S., Eastman, J. A., 2002, “Mechanisms of heat flow in suspensions of nano-sized particles (nanofluids),” *International Journal of Heat and Mass Transfer*, **45**(4), pp. 855-863.

Keblinski, P., Prasher, R., Eapen, J., 2008, “Thermal conductance of nanofluids: is the controversy over?,” *Journal of Nanoparticle Research*, **10**(7), pp. 1089-1097.

Khodadadi, J. M., Fan, L., Babaei, H., 2013, “Thermal conductivity enhancement of nanostructure-based colloidal suspensions utilized as phase change materials for thermal energy storage: A review,” *Renewable and Sustainable Energy Reviews*, **24**, pp. 418-444.

Khodadadi, J. M., Hosseinizadeh, S. F., 2007, “Nanoparticle-enhanced phase change materials (NEPCM) with great potential for improved thermal energy storage,” *International Communications in Heat and Mass Transfer*, **34**(5), pp. 534-543.

Kim, S., Drzal, L. T., 2009, “High latent heat storage and high thermal conductive phase change materials using exfoliated graphite nanoplatelets,” *Solar Energy Materials and Solar Cells*, **93**(1), pp. 136–142.

Kremer, K., Grest, G. S., 1990, “Dynamics of entangled linear polymer melts: A molecular dynamics simulation,” Journal of Chemical Physics, **92**(8), pp. 5057-5086.

Kubo, R., 1957, “Statistical-mechanical theory of irreversible processes. I. General theory and simple applications to magnetic and conduction problems,” *Journal of the Physical Society of Japan*, **12**(6), pp. 570-586.

Kumar, D. H., Patel, H. E., Kumar, V. R. R., Sundararajan, T., Pradeep, T., Das, S. K., 2004, “Model for heat conduction in nanofluids,” *Physical Review Letters*, **93**(14), 144301.

Landauer, R., 1952, “The electrical resistance of binary metallic mixtures,” *Journal of Applied Physics*, **23**(7), pp. 779-784.

Lee, S., Choi, U. S., Li, S., Eastman, J. A., 1999, “Measuring thermal conductivity of fluids containing oxide nanoparticles,” *Journal of Heat Transfer*, **121**(2), pp. 280–289.

Li, J., Porter, L.,Yip, S., 1998 “Atomistic modeling of finite-temperature properties of crystalline b-SiC II. Thermal conductivity and effects of point defects,” *Journal of Nuclear Materials*, **255**(2-3), pp. 139-152.

Lide, D. R., 2005, “*Handbook of chemistry and physics*,” 85th ed., CRC Press, Boca Raton, FL.

Lin, S., Buehler, M. J., 2013, “The effect of non-covalent functionalization on the thermal conductance of graphene/organic interfaces,” *Nanotechnology*, **24**(16), 165702.

Lindsay, L., Broido, D. A., 2010, “Optimized Tersoff and Brenner empirical potential parameters for lattice dynamics and phonon thermal transport in carbon nanotubes and graphene,” *Physical Review B*, **81**(20), 205441.

Liu, Y-D , Zhou, Y-G, Tong, M-W, Zhou, X-S, 2009, “Experimental study of thermal diffusivity and phase change performance of nanofluids PCMs,” *Microfluidics Nanofluidics,* **7**, pp. 579-584.

Losego, M. D., Cahill, D. G., 2013, “Breaking through barriers,” *Nature Materials*, *News & Views*.

Losego, M. D., Grady, M. E., Sottos, N. R., Cahill, D. G., Braun, P. V., 2012, “Effects of chemical bonding on heat transport across interfaces,” *Nature Materials*, **11**, pp. 502–506.

Lumpkin M. E., Saslow, W. M., Visscher, W. M., 1978, “One-dimensional Kapitza conductance: Comparison of the phonon mismatch theory with computer experiments,” *Physical Review B*, **17**(11), pp. 4295-4302.

Lüth, H., Nyburg, S. C., Robinson, P. M., Scott, H. G., 1974, “Crystallographic and calorimetric phase studies of the n-eicosane, $C_{20}H_{42}$: n-docosane, $C_{22}H_{46}$ system,” *Molecular Crystals and Liquid Crystals*, **27**(3-4), pp. 337-357.

MacGowan, D., Evans, D. J., 1986, “Heat and matter transfer in binary liquid mixtures,” *Physical Review A*, **34**(3), pp. 2133-2142.

Marbeuf, A., Brown, R., 2006, “Molecular dynamics in n-alkanes: Premelting phenomena and rotator phases,” *The Journal of Chemical Physics*, **124**, 054901.

Martin, M. G., Siepmann, J. I., 1998, “Transferable potentials for phase equilibria. 1. United-atom description of n-alkanes,” *The Journal of Physical Chemistry B*, **102**(14), pp. 2569-2577.

Martinez, L., Andrade, R., Birgin, E. G., Martínez, J. M., 2009, “Packmol: A package for building initial configurations for molecular dynamics simulations,” *Journal of Computational Chemistry*, **30**(13), pp. 2157-2164.

Masuda, H., Ebata, A., Teramae, K., Hishinuma, N., 1993, “Alteration of thermal conductivity and viscosity of liquid by dispersing ultra-fine particles,” *Netsu Bussei*, **7**(4), pp. 227–233.

Maxwell, J. C., 1881, “*A treatise on electricity and magnetism (Vol. 1)*,” 2nd ed., Clarendon Press, Oxford.

McLaughlin, E., 1964, “The thermal conductivity of liquids and dense gases,” *Chemical Reviews*, **64**(4), pp. 389–428.

McQuarrie, D. A., 2000, “Statistical mechanics,” University Science Books, California.

Müller, A., 1928, “A further X-ray investigation of long chain compounds (n-Hydrocarbon),” *Proceedings of the Royal Society of London. Series A*, Containing Papers of a Mathematical and Physical Character, **120**(785), pp. 437-459.

Müller-Plathe, F., 1997, “A simple nonequilibrium molecular dynamics method for calculating the thermal conductivity,” *The Journal of Chemical Physics*, **106**, pp. 6082-6086.

Murshed, S. M. S., 2009, “Correction and comment on “Thermal conductance of nanofluids: is the controversy over?,” *Journal of Nanoparticle Research*, **11**(2), pp. 511–512.

Nan, C.-W., Birringer, R., Clarke, D. R., Gleiter, H., 1997, “Effective thermal conductivity of particulate composites with interfacial thermal resistance,” *Journal of Applied Physics*, **81**(10), pp. 6692–6699.

Nath, S. K., Escobedo, F. A., de Pablo, J. J., 1998, “On the simulation of vapor–liquid equilibria for alkanes,” *The Journal of Chemical Physics*, **108**, 9905.

Nosé, S., 1984, “A unified formulation of the constant temperature molecular dynamics methods,” *The Journal of Chemical Physics*, **81**(1), pp. 511-519.

O’Brien, P. J., Shenogin, S., Liu, J., Chow, P. K., Laurencin, D., Mutin, P. H., Yamaguchi, M., Keblinski, P., Ramanath, G., 2012, “Bonding-induced thermal conductance enhancement at inorganic heterointerfaces using nanomolecular monolayers,” *Nature Materials*, **11**(10), pp. 1–5.

Ong, W. L., Rupich, S. M., Talapin, D. V., McGaughey, A. J., Malen, J. A., 2013, “Surface chemistry mediates thermal transport in three-dimensional nanocrystal arrays,” *Nature Materials*, **12**(5), pp. 410-415.

Paolini G. V., Ciccotti, G., 1987, “Cross thermotransport in liquid mixtures by nonequilibrium molecular dynamics,” *Physical Review A*, **35**(12), pp. 5156-5166.

Plimpton, S., 1995, “Fast parallel algorithms for short-range molecular dynamics,” *Journal of Computational Physics*, **117**(1), pp. 1-19.

Pomeau, Y., 1972, “Asymptotic Behavior of the Green-Kubo Integrands in Binary Mixtures,” *The Journal of Chemical Physics*, **57**(7), pp. 2800-2810.

Powell, R. W., Challoner, A. R., 1961, “Thermal conductivity of n-octadecane,” *Industrial and Engineering Chemistry*, **53**, pp. 581-582.

Prasher, R., Bhattacharya, P., Phelan, P. E., 2005, “Thermal conductivity of nanoscale colloidal solutions (nanofluids),” *Physical Review Letters*, **94**(2), pp. 025901–1–4.

Prasher, R., Bhattacharya, P., Phelan, P. E., 2006, “Brownian-motion-based convective-conductive model for the effective thermal conductivity of nanofluids,” *Journal of Heat Transfer*, **128**(6), pp. 588-595.

Prasher, R., Phelan, P. E., Bhattacharya, P., 2006, "Effect of aggregation kinetics on the thermal conductivity of nanoscale colloidal solutions (nanofluid)," *Nano Letters*, **6**(7), pp. 1529–1534.

Progelhof, R. C., Throne, J. L., and Ruetsch, R. R., 1976, "Methods for predicting the thermal conductivity of composite systems: A review," *Polymer Engineering and Science,* **16**(9), pp. 615-625.

Putnam, S. A., Cahill, D. G., Braun, P. V., Ge, Z., Shimmin, R. G., 2006, "Thermal conductivity of nanoparticle suspensions," *Journal of Applied Physics,* **99**(8), pp. 084308-084308.

Rapaport, D. C., 2004, "*The art of molecular dynamics simulation*," Cambridge University Press, New York.

Rastgarkafshgarkolaei, R., 2014, "Effect of the chain on thermal conductivity and thermal boundary conductance of long chain n-alkanes using molecular dynamics and transient plane source techniques," Auburn University, Master Thesis.

Rigby, D., Roe, R. J., 1988, "Molecular dynamics simulation of polymer liquid and glass. II. Short range order and orientation correlation," *The Journal of Chemical Physics*, **89**, 5280.

Ryckaert, J. P., 1995, "On the simulation of plastic crystals of< i> n</i>-alkanes with an atomistic model," *Physica A: Statistical Mechanics and its Applications*, **213**(1), pp. 50-60.

Ryckaert, J. P., Klein, M. L., 1986, "Translational and rotational disorder in solid n-alkanes: Constant temperature–constant pressure molecular dynamics calculations using infinitely long flexible chains," *The Journal of Chemical Physics,* **85**, 1613.

Ryckaert, J. P., Klein, M. L., McDonald, I. R., 1987, "Disorder at the bilayer interface in the pseudohexagonal rotator phase of solid n-alkanes," *Physical Review Letters*, **58**(7), pp. 698-701.

Sarkar, S., Selvam, R. P., 2007, “Molecular dynamics simulation of effective thermal conductivity and study of enhanced thermal transport mechanism in nanofluids,” *Journal of Applied Physics*, **102**(7), pp. 074302-074302.

Sasikumar, K., Keblinski, P., 2011, “Effect of chain conformation in the phonon transport across a Si-polyethylene single-molecule covalent junction,” *Journal of Applied Physics*, **109**, 114307.

Schelling, P. K., Phillpot, S. R., Keblinski, P., 2002, “Comparison of atomic-level simulation methods for computing thermal conductivity,” *Physical Review B*, **65**(14), pp. 1–12.

Schelling, P. K., Phillpot, S. R., Keblinski, P., 2002, “Phonon wave-packet dynamics at semiconductor interfaces by molecular-dynamics simulation,” *Applied Physics Letters*, **80**(14), pp. 2484-2486.

Sellan, D., Landry, E., Turney, J., McGaughey, A., Amon, C., 2010, “Size effects in molecular dynamics thermal conductivity predictions,” *Physical Review B*, **81**(21), pp. 1–10.

Shaikh, S., Lafdi, K., Hallinan, K., 2008, “Carbon nanoadditives to enhance latent energy storage of phase change materials,” *Journal of Applied Physics*, **103**(9), pp. 094302.

Shenogin, S., Ozisik, R., (2007), “Xenoview: visualization for atomistic simulations”.

Shenogin, S., Xue, L., Ozisik, R., Keblinski, P., Cahill, D.G., 2004, “Role of thermal boundary resistance on the heat flow in carbon-nanotube composites,” *Journal of Applied Physics*, **95**(12), pp. 8136–8144.

Shi, J.-N., Ger, M.-D., Liu, Y.-M., Fan, Y.-C., Wen, N.-T., Lin, C.-K., Pu, N.-W., 2013, “Improving the thermal conductivity and shape-stabilization of phase change materials using nanographite additives,” *Carbon*, **51**, pp. 365–372.

Shimizu, T., Yamamoto, T., 2000, “Melting and crystallization in thin film of n-alkanes: A molecular dynamics simulation,” *The Journal of Chemical Physics*, **113**(8), 3351.

Sindzingre, P., Ciccotti, G., Massobrio, C., Frenkel, D., 1987, “Partial enthalpies and related quantities in mixtures from computer simulation,” *Chemical Physics Letters*, **136**(1), pp. 35-41.

Sindzingre, P., Massobrio, C., Ciccotti, G., 1989, “Calculation of partial enthalpies of an argon-krypton mixture by NPT molecular dynamics,” *Chemical Physics*, **129**(2), pp. 213-224.

Smit, B., Karaborni, S., Siepmann, J. I., 1995, “Computer simulations of vapour-liquid phase equilibria of n-alkanes,” *Journal of Chemical Physics*, **102**, 2126.

Smith, A. E., 1953, “The crystal structure of the normal paraffin hydrocarbons,” *The Journal of Chemical Physics*, **21**(12), pp. 2229-2231.

Stuart, S. J., Tutein, A. B., Harrison, J. A., 2000, “A reactive potential for hydrocarbons with intermolecular interactions,” *The Journal of Chemical Physics*, **112**, 6472.

Sun, H., 1998, “COMPASS: An ab initio force-field optimized for condensed-phase applications overview with details on alkane and benzene compounds,” *The Journal of Physical Chemistry B*, **102**(38), pp. 7338-7364.

Swartz, E. T., Pohl, R. O., 1989, “Thermal boundary resistance,” *Reviews of Modern Physics*, **61**(3), pp. 605-668.

Swartz, E. T., Pohl, R. O., 1987, “Thermal resistance at interfaces,” *Applied Physics Letters*, **51**(26), pp. 2200-2202.

Tersoff, J., 1988, “Empirical interatomic potential for carbon, with application to amorphous carbon,” *Physical Review Letters*, **61**, pp. 2879-2882.

Tersoff, J., 1988, “New empirical approach for the structure and energy of covalent systems,” *Physical Review B*, **37**(12), 6991.

Tersoff, J., 1989, “Modeling solid-state chemistry: Interatomic potentials for multicomponent systems,” *Physical Review B,* **39**(8), pp. 5566-5568.

Tersoff, J., 1990, “Erratum: Modeling solid-state chemistry: Interatomic potentials for multicomponent systems,” *Physical Review B,* **41**(5), pp. 3248-3248.

Todd, B. D., Daivis, P. J., Evans, D. J., 1995, “Heat Aux vector in highly inhomogeneous nonequilibrium fluids,” *Physical Review E,* **51**(5), pp. 4362–4368.

Torquato, S., 1985, “Effective electrical conductivity of two-phase disordered composite media,” *Journal of Applied Physics*, **58**(10), pp. 3790-3797.

Verlet, L., 1967, “Computer experiments on classical fluids. I. Thermodynamical properties of Lennard-Jones molecules,” *Physical Review*, **159**, pp. 98-103.

Vogelsang, R., Hoheisel, C., 1987, “Thermal conductivity of a binary-liquid mixture studied by molecular dynamics with use of Lennard-Jones potentials,” *Physical Review A*, **35**(8), pp. 3487-3491.

Vogelsang, R., Hoheisel, C., Ciccotti, G., 1987, “Thermal conductivity of the Lennard-Jones liquid by molecular dynamics calculations,” *The Journal of Chemical Physics*, **86**(11), pp. 6371-6375.

Vogelsang, R., Hoheisel, C., Paolini, G. V., Ciccotti, G., 1987, “Soret coefficient of isotopic Lennard-Jones mixtures and the Ar-Kr system as determined by equilibrium molecular-dynamics calculations,” *Physical Review A*, **36**(8), pp. 3964-3974.

Waheed, N., Lavine, M. S., Rutledge, G. C., 2002, “Molecular simulation of crystal growth in n-eicosane,” *The Journal of Chemical Physics*, **116**, 2301.

Walther, J. H., Jaffe, R., Halicioglu, T., Koumoutsakos, P., 2001, “Carbon nanotubes in water: structural characteristics and energetic,” *The Journal of Physical Chemistry B*, **105**, 9980–9987.

Wang, J., Xie, H., Xin, Z., 2009, “Thermal properties of paraffin based composites containing multi-walled carbon nanotubes,” *Thermochimica Acta*, **488**(2), pp. 39–42.

Wang, X., Xu, X., Choi, S. U. S., 1999, ‘‘Thermal conductivity of nanoparticle-fluid mixture,’’ *Journal of Thermophysics and Heat Transfer*, **13**(4), pp. 474–480.

Wentzel, N., Milner, S. T., 2010, “Crystal and rotator phases of n-alkanes: A molecular dynamics study,” *The Journal of Chemical Physics*, **132**(4), 044901-044901.

Williams, D. E., 1967, “Nonbonded potential parameters derived from crystalline hydrocarbons,” *The Journal of Chemical Physics*, **47**, 4680.

Wu, S., Zhu, D., Zhang, X., Huang, J., 2010, “Preparation and melting/freezing characteristics of Cu/paraffin nanofluid as phase-change material (PCM),” *Energy and Fuels*, **24**(3), pp. 1894-1898.

Xiang, J., Drzal, L. T., 2011, “Investigation of exfoliated graphite nanoplatelets (xGnP) in improving thermal conductivity of paraffin wax-based phase change material,” *Solar Energy Materials and Solar Cells*, **95**(7), pp. 1811–1818.

Xie, H., Li, Y., Chen, L., 2009, “Adjustable thermal conductivity in carbon nanotube nanofluids, *Physics Letters A*, **373**(21), pp. 1861-1864.

Xuan, Y., Li, Q., Hu, W., 2003, “Aggregation structure and thermal conductivity of nanofluids,” AIChE Journal, **49**(4), pp. 1038–1043.

Xue, L., Keblinski, P., Phillpot, S. R., Choi, S. S., Eastman, J. A., 2004, “Effect of liquid layering at the liquid–solid interface on thermal transport,” *International Journal of Heat and Mass Transfer*, **47**(19), pp. 4277-4284.

Yarborough, D. W., Kuan, C-N, 1983, “The thermal conductivity of n-eicosane, n-octadecane, n-heptadecane, n-pentadecane, and n-tetradecane,” *17th I. Therm. Cond. Conf.*, June,

1981. Published in *Thermal Conductivity 17*, Plenum Press, New York, Ed. J.G. Hust, pp. 265-274.

Yavari, F., Raeisi Fard, H., Pashayi, K., Rafiee, M. A., Zamiri, A., Yu, Z., Ozisik, R., Borca-Tasciuc, T., Koratkar, N., 2011, "Enhanced thermal conductivity in a nanostructured phase change composite due to low concentration graphene additives," *Journal of Physical Chemistry C*, **115**(17), pp. 8753–8758.

Younglove, B., Ely, J. F., 1987, "*Thermophysical properties of fluids: II. Methane, Ethane, Propane, Isobutane, and normal Butane*," American Chemical Society and the American Institute of Physics for the National Bureau of Standards.

Yu, A. P., Ramesh, P., Itkis, M. E., Bekyarova, E., Haddon, R. C., 2007, "Graphite nanoplatelet-epoxy composite thermal interface materials," *Journal of Physical Chemistry C*, **111**(21), pp. 7565-7569.

Yu, A., Ramesh, P., Sun, X., Bekyarova, E., Itkis, M. E., Haddon, R. C., 2008, "Enhanced thermal conductivity in a hybrid graphite nanoplatelet – carbon nanotube filler for epoxy composites," *Advanced Materials*, **20**(24), pp. 4740–4744.

Yu, W., Xie, H., Chen, W., 2010, "Experimental investigation on thermal conductivity of nanofluids containing graphene oxide nanosheets," *Journal of Applied Physics*, **107**(9), 094317.

Yu, W., Xie, H., Wang, X., Wang, X., 2011, "Significant thermal conductivity enhancement for nanofluids containing graphene nanosheets," *Physics Letters A*, **375**(10), pp. 1323–1328.

Yu, Z.-T., Fang, X., Fan, L.-W., Wang, X., Xiao, Y.-Q., Zeng, Y., Xu, X., et al., 2013, "Increased thermal conductivity of liquid paraffin-based suspensions in the presence of carbon nano-additives of various sizes and shapes," *Carbon*, **53**, pp. 277–285.

Zeng, J. L., Liu, Y. Y., Cao, Z. X., Zhang, J., Zhang, Z. H., Sun, L. X., Xu, F., 2008, “Thermal conductivity enhancement of MWNTs on the PANI/tetradecanol form-stable PCM,” *Journal of Thermal Analysis and Calorimetry*, **91**(2), pp. 443-446.

Zeng, J. L., Cao, Z., Yang, D. W., Xu, F., Sun, L. X., Zhang, X. F., Zhang, L., 2009, Effects of MWNTs on phase change enthalpy and thermal conductivity of a solid-liquid organic PCM,” *Journal of Thermal Analysis and Calorimetry*, **95**(2), pp. 507-512.

Zhang, L., Wang, J.-S., Li, B., 2008, “Ballistic magnetothermal transport in a Heisenberg spin chain at low temperatures,” *Physical Review B*, **78**(14), 144416.